

**Антене и простирање**

**Antennas and Propagation**

# Second Integration within Potential Integrals in Case of Singular Basis Functions Using Singularity Cancellation

Aleksandra J. Krneta and Branko M. Kolundzija, *Fellow, IEEE*

**Abstract**—Efficient and accurate evaluation of potential integrals represents one of the main problems when using singular basis functions in the MoM/EFIE analysis of structures with the edge effect. In this work singularity cancellation technique is considered for precise evaluation of the second integration of potential integrals with singular basis functions in case of axially symmetric structures. The efficiency of this technique is analyzed on several examples for various angles between edges and for different positions of the field point.

**Index Terms**—Integral equation, Method of moments (MoM), potential integrals, singular basis functions, singularity cancellation.

## I. INTRODUCTION

THE moment method (MoM) is a well-established method which has been growing and improving for more than fifty years [1]. One of the current trends is the development of singular basis functions and their implementation in the method.

Namely, when using MoM/EFIE method for the EM analysis, at the edges of a structure surface charge may be singular as well as the parallel component of the surface current [1]-[6]. Polynomial basis functions, that are commonly used, can poorly take into account the edge effect. Therefore, singular basis functions are developed which can precisely follow the singular behavior of surface currents and charges. Various singular basis functions have been developed for 2D and 3D problems [2]-[4]. If properly chosen they can increase the accuracy of output results for several orders of magnitude [5].

However, singular integrals within the MoM system matrix, that arise in the case of singular basis functions, are very difficult to evaluate numerically [6]. Namely, the integrands have a singularity because of the singular basis functions and they can have another quasi-singularity due to the closeness of the field point. Accordingly, numerical integration of these integrals represents one of the main problems when implementing singular basis functions.

Singularity cancellation technique has been successfully

Aleksandra J. Krneta is with the School of Electrical Engineering, University of Belgrade, 73 Bulevar kralja Aleksandra, 11020 Belgrade, Serbia (e-mail: krneta@etf.rs).

Branko M. Kolundzija is with the School of Electrical Engineering, University of Belgrade, 73 Bulevar kralja Aleksandra, 11020 Belgrade, Serbia (e-mail: kol@etf.rs).

used for the integration of potential and impedance integrals in case of polynomial basis functions [7]-[9]. The focus of this work is efficient evaluation of the second integration of potential integrals with singular basis functions in case of axially symmetric structures using singularity cancellation.

Description of the considered problem and the choice of singular basis functions is discussed in section II. Potential integrals that are analyzed are also shown in section II. In section III several variable transformations are proposed for singularity cancellation for the evaluation of the second integration of potential integrals. Numerical results are shown in section IV where the efficiency of proposed variable changes are mutually compared. Conclusions are drawn in section V.

## II. POTENTIAL INTEGRALS IN CASE OF SINGULAR BASIS FUNCTIONS

Consider an axially symmetric structure modeled with building elements in the form of right-truncated cone surfaces (as shown in Fig. 1a), whose axis coincides with the  $z$ -axis. Every right-truncated cone can be defined using  $z$ -coordinates,  $z_1$  and  $z_2$ , and radii,  $a_1$  and  $a_2$ , at its endings. It can also be defined using  $z$ -coordinate,  $z_c$ , and radius,  $a_c$ , at the center of the cone, and half-differences of the  $z$ -coordinate,  $\Delta z$ , and radii,  $\Delta a$ , between its endings (see Fig. 1a). The relations between these parameters are

$$z_c = (z_1 + z_2)/2, \quad a_c = (a_1 + a_2)/2, \quad (1a,b)$$

$$\Delta z = (z_2 - z_1)/2, \quad \Delta a = (a_2 - a_1)/2. \quad (1c,d)$$

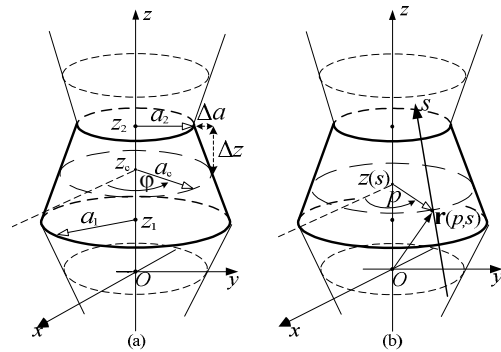


Fig. 1. (a) Example of an axially symmetric structure and (b) local  $ps$ -coordinate system.

Potential integrals that are considered, are given with

$$P = \int_{-1}^1 \int_{-1}^1 f_i(s) g(R) ds dp, \quad (2a)$$

$$P' = \int_{-1}^1 \int_{-1}^1 \frac{df_i(s)}{ds} g(R) ds dp, \quad (2b)$$

$$Q = \int_{-1}^1 \int_{-1}^1 f_i(s) g(R) \cos(\pi p) ds dp, \quad (2c)$$

where  $s$  is the local coordinate that goes along the generatrix of the element and takes values  $-1$  and  $1$ , at its ends (see Fig. 1b),  $p = \varphi/\pi$  is also a local coordinate that goes along the circumference of the considered element ( $\varphi$  is the azimuthal angle in cylindrical coordinate system),  $f_i(s)$  are basis functions that are used for the analysis,  $g(R) = e^{-j\beta R}/(4\pi R)$  is the Green's function,  $\beta = \omega(\mu_0 \epsilon_0)^{-1/2}$  is the phase coefficient, and  $R = |\mathbf{r}_l - \mathbf{r}_k|$  is the distance between the field point  $\mathbf{r}_l$  and the source point  $\mathbf{r}_k$  (which is on the considered generatrix of the element).

The basis functions are specifically chosen to take into account the edge effect. Namely, in the general case of an axially symmetric problem, surface current does not have a tangential component to any edge of the structure, and surface charge at the sharp edge has infinite value. For this reason singular functions, given with

$$f_i(s) = \begin{cases} (1+s)^b (1-s), & s_{ki} = -1 \\ (1+s)(1-s)^b, & s_{ki} = 1 \end{cases}, \quad (3a)$$

are chosen as basis functions [1], [5]. In (3a)  $s_{ki}$  represents the end where the edge effect is considered, and parameter  $b$  depends on the angle  $\theta$  between the generatrices of neighboring elements (as shown in Fig. 2a) and is given with  $b = \pi/(2\pi - \theta)$  [1], [5]. In case of an open end of the structure  $\theta$  has value  $\theta = 0$ , therefore  $b = 0.5$  (see Fig. 2b).

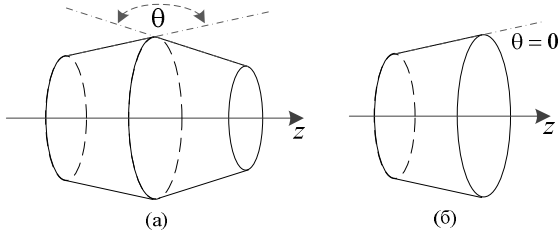


Fig. 2. (a) Angle  $\theta$  between the generatrices of neighboring elements. (b)  $\theta = 0$  in case of an open end of the structure (therefore  $b = 0.5$ ).

First derivative of the singular basis functions is given with

$$\frac{df_i(s)}{ds} = \begin{cases} (1+s)^{b-1} (b-1-s(b+1)), & s_{ki} = -1 \\ (1-s)^{b-1} (-b+1-s(b+1)), & s_{ki} = 1 \end{cases}, \quad (3b)$$

and it has infinite value at the point  $s = s_{ki}$ .

Since basis functions (3) are not polynomial functions and because they are singular at point  $s_{ki}$  numerical integration of (2) is very difficult using standard Gauss-Legendre integration formula. Therefore, singularity cancellation technique is applied as follows.

### III. SINGULARITY CANCELLATION FOR EVALUATION OF POTENTIAL INTEGRALS

The first integration of the potential integrals (2) goes along the  $s$ -axis and is given with

$$I_1 = \int_{-1}^1 f_i(s) g(R) ds, \quad (4a)$$

$$I_1' = \int_{-1}^1 \frac{df_i(s)}{ds} g(R) ds. \quad (4b)$$

Integrands from (4) are singular due to singular basis functions and they may have a quasi-singularity due to the closeness of the field point. In this work integrals from (4) are accurately evaluated using variable transformations from [6] for singularity cancellation technique.

The second integration of potential integrals (2) is given with

$$P = \int_{-1}^1 I_1(p, \mathbf{r}_l) dp, \quad (5a)$$

$$P' = \int_{-1}^1 I_1'(p, \mathbf{r}_l) dp, \quad (5b)$$

$$Q = \int_{-1}^1 I_1(p, \mathbf{r}_l) \cos(\pi p) dp. \quad (5c)$$

Without diminishing generality of the problem, let us suppose that the field point is in the  $xOz$ -plane. In that case integrands from (5) have singular behavior in the vicinity of  $p = 0$ . The singular behavior becomes more pronounced as the field point approaches the surface of the element.

In order to efficiently evaluate potential integrals (5) singularity cancellation technique is considered. Several variable transforms are analyzed.

First variable transform that is considered is

$$dt = \frac{dp}{\sqrt{p(2-p)}}, \quad t = \arcsin(p-1) \quad (6a,b)$$

$$p = \sin(t) + 1, \quad dp = \cos(t) dt, \quad (6c,d)$$

where  $p \in (0,2)$ . After applying (6), the integrals from (5) are evaluated using Gauss-Legendre (GL) integration formula. The transformation (6) as well the integrands from (5) are symmetrical with respect to  $p = 1$ . Therefore in order to increase the efficiency of numerical integration, GL formula of order  $2n$  is applied, and only first  $n$  samples are evaluated [10].

The second variable transform that is inspected is [9]

$$dt = \frac{dp}{\sqrt{p^2 + a'^2}}, \quad t = \ln \frac{p + \sqrt{p^2 + a'^2}}{a'} \quad (7a,b)$$

$$p = a' \sinh(t), \quad dp = a' \cosh(t) dt, \quad (7c,d)$$

where  $a'$  represents normalized distance between the field point  $\mathbf{r}_l$  and the considered element [9]. Having in mind (7b) it can be seen that the variable change (7) cannot be used if  $a' = 0$ . Therefore, variable change (7) can only be used if the field point is not directly on the surface of the element. The

transformation (7) as well the integrands from (5) are symmetrical with respect to  $p=0$ . Accordingly, the efficiency of integration can be increased by applying GL formula of order  $2n$ , and by evaluating only first  $n$  samples [10].

The last variable change that is considered is the Double-Exponential formula (DE) from [11]. Due to symmetry, only first  $n+1$  samples can be used (out of  $2n+1$ ).

#### IV. NUMERICAL RESULTS

The efficiency of proposed variable transformations for singularity cancellation is analyzed for several values of parameter  $b$ , for different positions of the field point and for various shapes of the element. The frequency is  $f=300$  MHz ( $\lambda \approx 1$  m). In every Fig. results are shown for proposed variable transformations and for direct integration (i.e. when directly applying GL integration formula) for comparison.

As the first example let us consider a cylindrical element of height  $h=2\lambda$  and radius  $a_1=a_2=\lambda$  (i.e.  $\Delta z=\lambda$ ,  $\Delta a=0$ ,  $z_c=\lambda$  and  $a_c=\lambda$ ) with parameter  $b=0.7$ . The field point is directly on the surface of the element with coordinates  $z_l=\lambda$ ,  $a_l=\lambda$ . Fig. 3 shows the efficiency of evaluation of the potential integral (5a) versus the number of integration points.

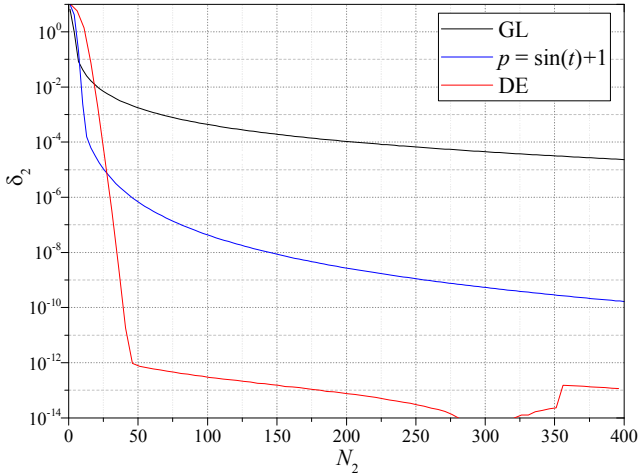


Fig. 3. Relative error  $\delta_2$  of integration of (5a) versus the number of integration points  $N_2$  for several integration techniques in the case of  $b=0.7$ . Cylinder dimensions:  $\Delta z=\lambda$ ,  $\Delta a=0$ ,  $z_c=a_c=\lambda$ , field point coordinates:  $z_l=\lambda$ ,  $a_l=\lambda$ .

As the next example the same cylindrical element is considered but with parameter  $b=7/9$ . Fig. 4 shows relative error of the integration of integral (5c) for the case when the field point is close to the surface of the element, with coordinates  $z_l=\lambda$ ,  $a_l=\lambda+10^{-4}\lambda$ . Fig. 5 shows the efficiency of integration of (5b) when the field point is directly on the surface of the element, with coordinates  $z_l=\lambda$ ,  $a_l=\lambda$ .

Results in Figs. 6 and 7 are for the case of a conical element with height  $h=2\lambda$  and the radius of the base  $a=2\lambda$  (i.e.  $\Delta z=\lambda$ ,  $\Delta a=\lambda$ ,  $z_c=\lambda$  and  $a_c=\lambda$ ). Parameter  $b$  has value  $b=7/8$ . In the case of Fig. 6 the field point is very close to the surface of the cone with coordinates  $z_l=1.5\lambda$ ,  $a_l=1.5\lambda+10^{-5}\lambda$ , and the efficiency of evaluation of (5a) is shown. Fig. 7 shows results for the efficiency of evaluation of (5b) for the case when the field point is directly on the surface of the cone, with

coordinates  $z_l=1.5\lambda$ ,  $a_l=1.5\lambda$ .

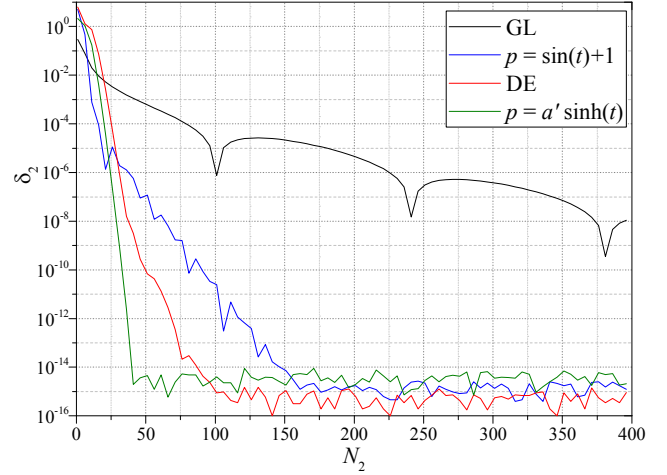


Fig. 4. Relative error  $\delta_2$  of evaluation of (5c) versus the number of integration points  $N_2$  for several integration techniques in the case of  $b=7/9$ . Cylinder dimensions:  $\Delta z=z_c=a_c=\lambda$ ,  $\Delta a=0$ , field point coordinates:  $z_l=\lambda$ ,  $a_l=\lambda+10^{-4}\lambda$ .

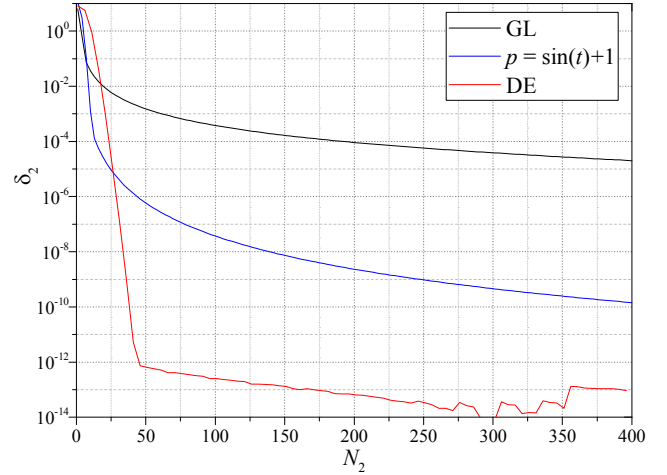


Fig. 5. Relative error  $\delta_2$  of evaluation of (5b) versus the number of integration points  $N_2$  for several integration techniques in the case of  $b=7/9$ . Cylinder dimensions:  $\Delta z=z_c=a_c=\lambda$ ,  $\Delta a=0$ , field point coordinates:  $z_l=\lambda$ ,  $a_l=\lambda$ .

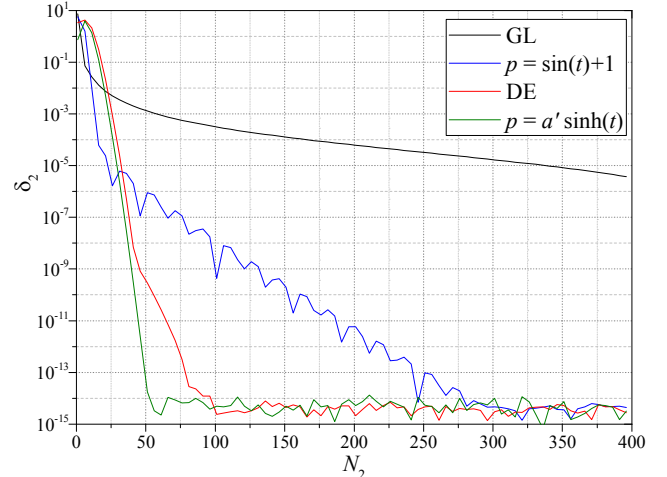


Fig. 6. Relative error  $\delta_2$  of evaluation of (5a) versus the number of integration points  $N_2$  for several integration techniques in the case of  $b=7/8$ . Cone dimensions:  $\Delta z=z_c=a_c=\Delta a=\lambda$ , field point coordinates:  $z_l=1.5\lambda$ ,  $a_l=1.5\lambda+10^{-5}\lambda$ .

As the next example right truncated cone is considered with height  $h=2\lambda$ , radius of the first basis  $a_1=2\lambda$  and of the second basis  $a_2=\lambda$  (i.e.  $\Delta z=\lambda$ ,  $\Delta a=-0.5\lambda$ ,  $z_c=\lambda$  and  $a_c=1.5\lambda$ ). Parameter  $b$  has value  $b=2/3$ . Fig. 8 shows the relative error of integration of (5b) in the case when the field point is close to the surface of the element with coordinates  $z_l=10^{-5}\lambda$ ,  $a_l=2\lambda+0.5\lambda\cdot 10^{-5}$ . Fig. 9 shows the relative error of evaluation of (5c) in the case when the field point is directly on the surface of the element with coordinates  $z_l=10^{-5}\lambda$ ,  $a_l=2\lambda-0.5\lambda\cdot 10^{-5}$ .

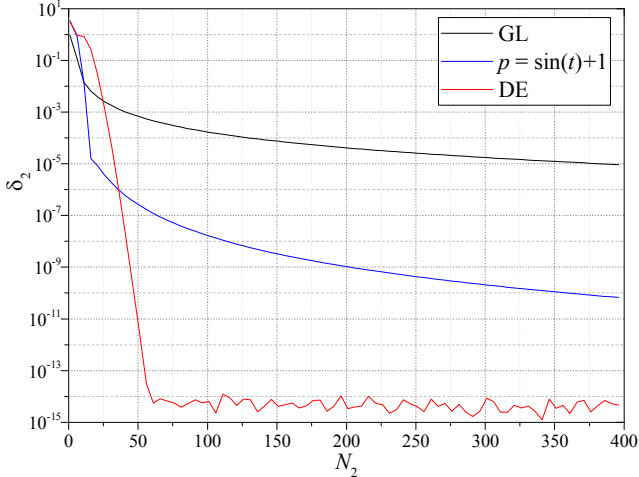


Fig. 7. Relative error  $\delta_2$  of evaluation of (5b) versus the number of integration points  $N_2$  for several integration techniques in the case of  $b=7/8$ . Cone dimensions:  $\Delta z=z_c=a_c=\Delta a=\lambda$ , field point coordinates:  $z_l=1.5\lambda$ ,  $a_l=1.5\lambda$ .

From Figs. 3-9 it can be seen that all variable transformations are much more efficient than direct integration (GL). For example, in the case of a conical element (with dimensions  $h=a=2\lambda$ ) and the field point which is near the surface of the cone (Fig. 6) variable transformation (7) provides maximal precision (relative error is  $\delta_2 \approx 10^{-15}$ ) with only 60 points. In contrast to that, direct integration requires 350 in order to provide the relative error of  $\delta_2 \approx 10^{-5}$ .

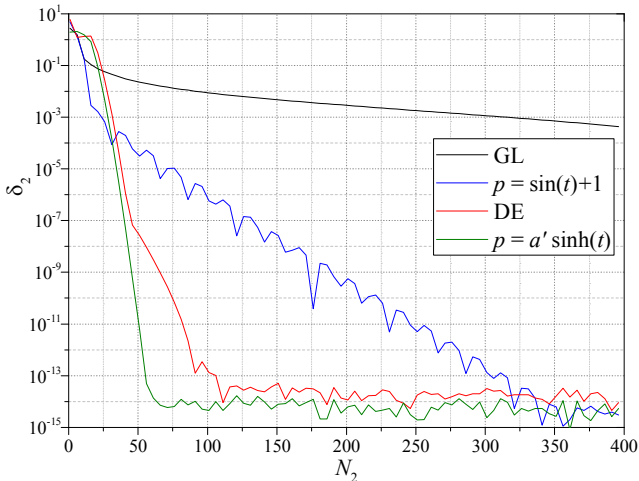


Fig. 8. Relative error  $\delta_2$  of evaluation of (5b) versus the number of integration points  $N_2$  for several integration techniques in the case of  $b=2/3$ . Right-truncated cone dimensions:  $\Delta z=z_c=\lambda$ ,  $a_c=1.5\lambda$ ,  $\Delta a=-0.5\lambda$ , field point coordinates:  $z_l=10^{-5}\lambda$ ,  $a_l=2\lambda+0.5\lambda\cdot 10^{-5}$ .

From Figs. 3-9 it can also be seen that if the field point is near the surface of the element, variable change (7) is the most efficient transformation. However, it cannot be used if the field point is directly on the surface of the element. DE formula can be used in all cases. In the case when the field point is directly on the surface of the element DE formula provides maximal precision with the least number of integration points.

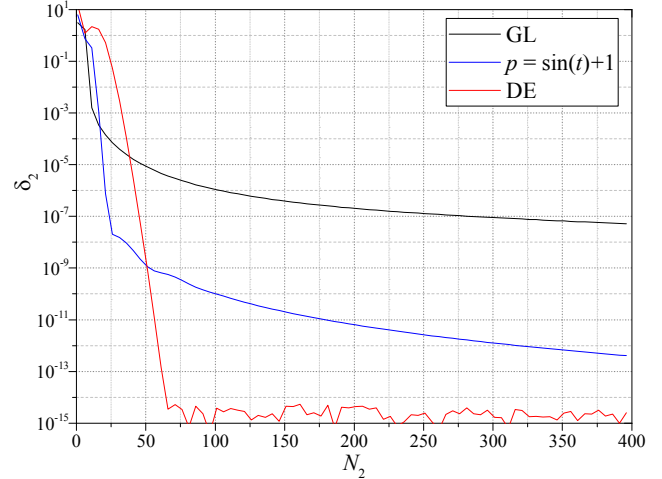


Fig. 9. Relative error  $\delta_2$  of evaluation of (5c) versus the number of integration points  $N_2$  for several integration techniques in the case of  $b=2/3$ . Right-truncated cone dimensions:  $\Delta z=z_c=\lambda$ ,  $a_c=1.5\lambda$ ,  $\Delta a=-0.5\lambda$ , field point coordinates:  $z_l=10^{-5}\lambda$ ,  $a_l=2\lambda-0.5\lambda\cdot 10^{-5}$ .

## V. CONCLUSION

In this work efficient and accurate evaluation of the second integration of potential integrals with singular basis functions is considered for MoM/EFIE analysis of axially symmetric structures. Singular basis functions are used in order to take into account the edge effect. The second integration of potential integrals has singular behavior in the vicinity of the projection of the field point to the considered element. Therefore, evaluation of potential integrals using standard Gauss-Legendre integration formula is inefficient.

For this reason several variable transformations are considered for accurate numerical integration of these integrals using singularity cancellation technique. The efficiency of these transformations is analyzed on several examples for different values of the angle at the edge, and for various shapes and dimensions of the element, as well as for different positions of the field point. From the results it can be concluded that all variable transformations are much more efficient than direct integration (GL). Variable change (7) provides maximal precision with the least number of integration points in the case when the field point is close to the surface of the element, and DE formula is the most efficient in the case when the field point is directly on the surface of the element.

The integration of potential integrals as a result of Galerkin test procedure using singular basis function (as test functions) is singular as well. Therefore, singularity cancellation technique could possibly improve the efficiency of evaluation

of these integrals (i.e. the impedance integrals) as well, which will be the subject of future work.

#### ACKNOWLEDGMENT

This work was supported by the Serbian Ministry of Education, Science and Technological Development under grant TR-32005.

#### REFERENCES

- [1] B. M. Kolundzija and A. R. Djordjevic, *Electromagnetic Modeling of Composite Metallic and Dielectric Structures*, Boston, MA, USA: Artech House, 2002.
- [2] W. J. Brown and D. R. Wilton, "Singular Basis Functions and Curvilinear Triangles in the Solution of the Electric Field Integral Equation," *IEEE Trans. Antennas Propag.*, vol. 47, no. 2, pp. 347-378, Feb. 1999.
- [3] M. M. Bibby, A. F. Peterson and C. M. Caldwell, "High Order Representations for Singular Currents at Corners," *IEEE Trans. Antennas Propag.*, vol. 56, no. 8, pp. 2277 - 2287, Aug. 2008.
- [4] G. Lombardi and R. D. Graglia, "Singular Higher Order Divergence-Conforming Bases of Additive Kind and Moments Method Applications to 3D Sharp-Wedge Structures," *IEEE Trans. Antennas Propag.*, vol. 56, no. 12, pp. 3768-3788, Dec. 2008.
- [5] A. J. Krmeta and B. M. Kolundzija, "The Use of Singular Basis Functions for Precise EM Analysis of Axially Symmetric Metallic Antennas," *IEEE 2019 AP-S & USNC/URCI*, Atlanta, USA, July, 2019.
- [6] A. J. Krmeta and B. M. Kolundzija, "The Use of Singular Basis Functions for Precise EM Analysis of Axially Symmetric Metallic Antennas," *2019 Int. Conf. Electromagnetics Adv. Applicat. (ICEAA)*, Granada, Spain, Sept 9-13, 2019.
- [7] A. G. Polimeridis, F. Vipiana, J. R. Mosig, and D. R. Wilton, "DIRECTFN: Fully Numerical Algorithms for High Precision Computation of Singular Integrals in Galerkin SIE Methods", *IEEE Trans. Antennas and Propag.*, vol. 61, no. 6, Jun 2013.
- [8] D. R. Wilton and N. J. Champagne, "Evaluation and integration of the thin wire kernel", *IEEE Trans. Antennas Propag.*, vol. 54, no. 4, pp. 1200-1206, Apr. 2006.
- [9] A. J. Krmeta and B. M. Kolundzija, "Evaluation of Potential and Impedance Integrals in Analysis of Axially Symmetric Metallic Structures to Prescribed Accuracy Up To Machine Precision," *IEEE Trans. Antennas Propag.*, vol. 65, no. 5, pp. 2526-2539, Feb. 2017.
- [10] A. J. Krmeta and B. M. Kolundzija, "Optimal Use of Gauss-Legendre Integration Formula for Evaluation of Potential Integrals in Analysis of Axially Symmetrical Wire Antennas," *3rd Int. Conf. Electr., Electron. Comp. Eng. (IcETAN 2016)*, Zlatibor, Serbia, June 13-16, 2016, pp. APII.4.1-6.
- [11] A. G. Polimeridis and J. R. Mosig, "Evaluation of Weakly Singular Integrals Via Generalized Cartesian Product Rules Based on the Double Exponential Formula", *IEEE Trans. Antennas and Propag.*, vol. 58, no. 6, Jun 2010.

# Performance of Max-Ortho Basis Functions in FEM Scattering Analysis

Slobodan V. Savić, *Member, IEEE*, Milan M. Ilić, *Senior Member, IEEE*,  
and Branko M. Kolundzija, *Fellow, IEEE*

**Abstract**—Performance of previously developed maximally orthogonalized higher order basis functions implemented in the large-domain finite element method are additionally evaluated in two numerical examples. In our previous work these basis functions were used only for non-radiating problems. In order to expand their scope, and make them suitable for radiating problems also, in this work these basis functions are combined with the first order absorbing boundary condition. It is shown that this does not degrade their superiority regarding the condition number.

**Index Terms**—Condition number; finite element method; higher-order basis functions; higher-order modeling; numerical analysis; orthogonal functions.

## I. INTRODUCTION

TWO most popular numerical techniques for solving general linear electromagnetic (EM) problems in the frequency domain are the finite element method (FEM) [1, 2] and the method of moments (MoM) [3, 4]. After expanding EM quantities in terms of basis functions and unknown coefficients, the final system of linear equations must be solved, which can represent a significant percentage of the total simulation execution time. There are several algorithms for solving systems of linear equations (iterative methods being some of them). In any case, larger systems of equations require more computational recourses and more time to be solved.

It is generally accepted that div- and curl-conforming higher-order basis functions are more efficient than low-order functions [5, 6], i.e., that they yield a smaller system of linear equations for the same accuracy, compared to low-order basis functions. Unfortunately, in their original form, hierarchical higher-order basis functions possess significant linear dependence, which leads to ill-conditioned system-matrices. This, in turn, limits the maximal order of basis functions in the mesh [7], and disables the efficient usage of iterative solvers [8, 9].

Great amount of work has been done within the community in attempts to construct more orthogonal and linearly independent basis functions [10-14]. In [15] a general theory

S. V. Savić is with the School of Electrical Engineering, University of Belgrade, Serbia (phone: +381 11 3218 351; e-mail: [ssavic@etf.bg.ac.rs](mailto:ssavic@etf.bg.ac.rs)).

M. M. Ilić is with the School of Electrical Engineering, University of Belgrade, Serbia (e-mail: [milanilic@etf.bg.ac.rs](mailto:milanilic@etf.bg.ac.rs)).

B. M. Kolundzija is with the School of Electrical Engineering, University of Belgrade, Serbia (e-mail: [kol@etf.bg.ac.rs](mailto:kol@etf.bg.ac.rs)).

of maximally orthogonal div- and curl-conforming higher-order basis functions is presented for generalized wires, quadrilaterals and hexahedra. Explicit expressions for these basis functions are presented up to the eight order and numerical results are presented for the MoM-SIE. In [16] maximally orthogonal basis functions were implemented in the higher-order large-domain FEM, and the novel two-term recurrent formulas for their calculation were developed.

As a continuation of our work in [9], [15] and [16], here we evaluate the accuracy and orthogonality of the maximally orthogonal basis functions in the higher-order large-domain FEM in two numerical experiments. As an addition to the numerical experiments from [16], these examples cover problems frequently encountered in engineering practice.

The rest of this paper is organized as follows. To keep the paper self-contained, the relevant theory of the higher order large-domain FEs is given in Section II. Three types of basis functions (classical, near-ortho and max-ortho), used in the higher-order FEM, are presented in Section III. Results of numerical experiments are presented in Section IV, and the concluding remarks are given in Section V.

## II. HIGHER ORDER LARGE-DOMAIN FINITE-ELEMENT TECHNIQUE

As a basic element for the geometrical modeling of arbitrary shaped 3-D electromagnetic (EM) structures in the FEM, we use a generalized curved parametric hexahedron [6] whose geometry is defined as

$$\mathbf{r}(u, v, w) = \sum_{m=0}^{K_u} \sum_{n=0}^{K_v} \sum_{l=0}^{K_w} \mathbf{r}_{mnl} L_m^{K_u}(u) L_n^{K_v}(v) L_l^{K_w}(w), \quad (1)$$

$$-1 \leq u, v, w \leq 1,$$

where  $\mathbf{r}_{mnl}$  are the position vectors of the interpolation nodes,  $K_u$ ,  $K_v$ , and  $K_w$  are the geometrical orders of the element along  $u$ -,  $v$ - and  $w$ -parametric coordinates, and  $L_m^{K_u}$ ,  $L_n^{K_v}$ , and  $L_l^{K_w}$  are the Lagrange interpolating polynomials [6].

Equation (1) defines a mapping from a cubical parent domain ( $-1 \leq u, v, w \leq 1$ ) to the generalized hexahedron, as illustrated in Fig. 1. All parameters of a FE, such as its basis functions, are defined in the parent domain and mapped through (1) to the global domain, i.e., to the  $xyz$ -coordinate system in Fig. 1.

In the FEM formulation, we start from the curl-curl electric field vector-wave equation [6]

$$\nabla \times \mu_r^{-1} \nabla \times \mathbf{E} - k_0^2 \epsilon_r \mathbf{E} = 0, \quad (2)$$

where  $\varepsilon_r$  and  $\mu_r$  are complex relative permittivity and permeability of the medium,  $\mathbf{E}$  is the electric-field complex intensity vector,  $k_0 = \omega\sqrt{\varepsilon_0\mu_0}$  is the free-space wave number,  $\varepsilon_0$  and  $\mu_0$  are permittivity and permeability of free space, and  $\omega$  is the angular frequency of the implied time-harmonic excitation. Inside each element we approximate the electric-field intensity vector as

$$\mathbf{E} = \sum_{i=0}^{N_u-1} \sum_{j=0}^{N_v-1} \sum_{k=0}^{N_w-1} \alpha_{uijk} \mathbf{f}_{uijk} + \sum_{i=0}^{N_u-1} \sum_{j=0}^{N_v-1} \sum_{k=0}^{N_w-1} \alpha_{vijk} \mathbf{f}_{vijk} + \sum_{i=0}^{N_u-1} \sum_{j=0}^{N_v-1} \sum_{k=0}^{N_w-1} \alpha_{wijk} \mathbf{f}_{wijk}, \quad (3)$$

where  $\mathbf{f}_{uijk}$ ,  $\mathbf{f}_{vijk}$ , and  $\mathbf{f}_{wijk}$  are the curl-conforming vector basis functions,  $N_u$ ,  $N_v$ , and  $N_w$  are adopted orders of the electric field expansion, and  $\alpha_{uijk}$ ,  $\alpha_{vijk}$ , and  $\alpha_{wijk}$  are unknown field-distribution coefficients to be determined by the FEM [6].

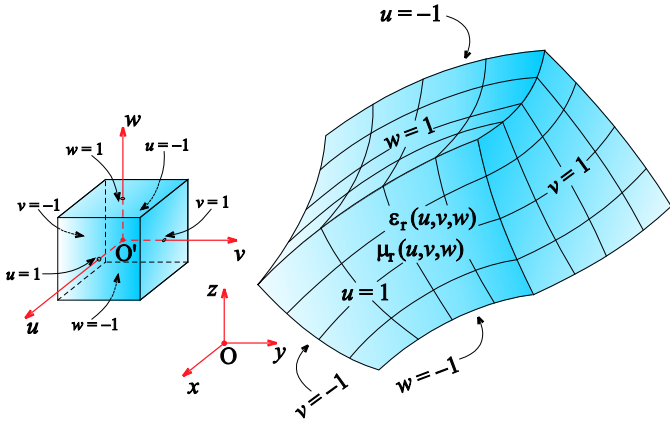


Fig. 1. Cube to hexahedron mapping defined by (1).

A standard Galerkin-type weak-form discretization of (2) yields [9]

$$\begin{aligned} & \int_V \mu_r^{-1} (\nabla \times \mathbf{f}_{ijk}) \cdot (\nabla \times \mathbf{E}) dV - k_0^2 \int_V \varepsilon_r \mathbf{f}_{ijk} \cdot \mathbf{E} dV = \\ & = - \oint_S \mu_r^{-1} \mathbf{f}_{ijk} \cdot \mathbf{n} \times (\nabla \times \mathbf{E}) dS, \end{aligned} \quad (4)$$

where  $V$  is the volume of the element,  $\mathbf{f}_{ijk}$  stands for any of the testing functions,  $S$  is the surface of the element, and  $\mathbf{n}$  is the outward unit normal to the surface of the element. (In the Galerkin method, testing functions are the same as the basis functions.) Electric field expansion from (3) is substituted in (4), leading to the final system of linear equations with unknown coefficients  $\alpha_{uijk}$ ,  $\alpha_{vijk}$  and  $\alpha_{wijk}$ . In the final discretized form of (4) the first integral on the left-hand side produces the entries of the FEM stiffness matrix, whereas the second integral produces the entries of the FEM mass matrix [1].

In the higher-order finite-element technique we use, basis functions are constructed from polynomials [6]. For the same field-expansion orders [ $N_u$ ,  $N_v$ , and  $N_w$  in (3)], namely for

the same degree of polynomial approximation of the EM field distribution, these polynomials can be arranged in different ways and different polynomials can be assigned to different basis functions [16]. Regardless of the way in which the polynomials are arranged, they span the same space and they equivalently approximate the EM field. On the other hand, they result in different stiffness and mass matrices and they produce different systems of linear equations. Because of this, by starting from one arrangement of polynomials in original basis functions, we can rearrange them in order to get the system of linear equations best suited for solving by standard numerical procedures. The condition number of the matrix is one of the parameters describing the corresponding system of equations in this sense, and, generally, matrices with smaller condition number are preferable, i.e., yield numerically more stable solutions.

### III. BASIS FUNCTIONS AND THEIR ORTHOGONALITY IN THE HIGHER ORDER FEM

The curl-conforming basis functions can be represented as [6]

$$\begin{aligned} \mathbf{f}_{uijk} &= P_i(u) S_j(v) S_k(w) \mathbf{a}^u, \\ \mathbf{f}_{vijk} &= S_i(u) P_j(v) S_k(w) \mathbf{a}^v, \\ \mathbf{f}_{wijk} &= S_i(u) S_j(v) P_k(w) \mathbf{a}^w, \end{aligned} \quad (5)$$

where  $\mathbf{a}^u$ ,  $\mathbf{a}^v$  and  $\mathbf{a}^w$  are reciprocal unitary vectors defined as

$$\mathbf{a}^u = \mathbf{a}_v \times \mathbf{a}_w / J, \quad \mathbf{a}^v = \mathbf{a}_w \times \mathbf{a}_u / J, \quad \mathbf{a}^w = \mathbf{a}_u \times \mathbf{a}_v / J, \quad (6)$$

$J$  is the Jacobian of the covariant transformation

$$J = (\mathbf{a}_u \times \mathbf{a}_v) \cdot \mathbf{a}_w, \quad (7)$$

and  $\mathbf{a}_u$ ,  $\mathbf{a}_v$  and  $\mathbf{a}_w$  are unitary vectors defined as

$$\mathbf{a}_u = d\mathbf{r}/du, \quad \mathbf{a}_v = d\mathbf{r}/dv \quad \text{and} \quad \mathbf{a}_w = d\mathbf{r}/dw, \quad (8)$$

with  $\mathbf{r}$  given in (1).

Two basis functions  $\mathbf{f}_i$  and  $\mathbf{f}_j$  are said to be orthogonal if their inner product is equal to zero [15, 16], i.e., if

$$\langle \mathbf{f}_i, \mathbf{f}_j \rangle = \int_V \mathbf{f}_i \cdot \mathbf{f}_j dV = 0, \quad i \neq j, \quad (9)$$

where  $V$  is the volume of the particular FE. Based on (9), basis functions belonging to different elements are inherently mutually orthogonal.

The orthogonality condition (9) takes into account the polynomial form of the basis functions, but also the geometry of the particular element [through the unitary and reciprocal unitary vectors, as well as the Jacobian appearing in (5) and (6)]. The orthogonality condition defined this way is very restrictive, so it is very challenging to develop basis functions orthogonal in this sense for a general (curved) FE. Because of this, we will consider less general and less restrictive orthogonality condition in which it is assumed that a FE has mutually orthogonal coordinate lines with constant unitary and reciprocal unitary vectors. In this particular case, the basis functions orthogonality defined in (9) can be reduced to the orthogonality of  $P$ - and  $S$ -functions from (5) [15, 16]. We will thus consider the two basis functions to be mutually

orthogonal if their  $P$ - and  $S$ -functions satisfy

$$\langle P_i, P_j \rangle = \int_{u=-1}^1 P_i(u) P_j(u) du = 0, \quad i \neq j, \quad \text{and} \quad (10)$$

$$\langle S_i, S_j \rangle = \int_{u=-1}^1 S_i(u) S_j(u) du = 0, \quad i \neq j. \quad (11)$$

Based on this we can define the orthogonality factors for  $P$ - and  $S$ -functions as [15, 16]

$$o_{ij}^P = \frac{\langle P_i, P_j \rangle}{\sqrt{\langle P_i, P_i \rangle} \sqrt{\langle P_j, P_j \rangle}} \quad \text{and} \quad o_{ij}^S = \frac{\langle S_i, S_j \rangle}{\sqrt{\langle S_i, S_i \rangle} \sqrt{\langle S_j, S_j \rangle}}. \quad (12)$$

Next, we consider three types of basis functions and their orthogonality: classical basis functions (CLBFs), near-ortho basis functions (NOBFs), and max-ortho basis functions (MOBFs), and we examine their performance and behavior in the context of the higher order large-domain FEM.

For CLBFs,  $P$ - and  $S$ -functions [in (5)] are defined as [5, 6, 15, 16]

$$P_i(u) = u^i, \\ S_j(v) = \begin{cases} 1 - (-1)^j v, & j = 0, 1 \\ v^j - 1, & j = 2, 4, 6, \dots, \quad -1 \leq u, v \leq 1. \\ v^j - v, & j = 3, 5, 7, \dots \end{cases} \quad (13)$$

$S$ -functions ( $S_j$ ,  $j \geq 0$ ) can be divided into two groups:  $S_0$  and  $S_1$  will be called *node  $S$ -functions*, and  $S_j$ ,  $j \geq 2$ , will be called *segment  $S$ -functions*, as in [15, 16]. Only basis functions with appropriate node  $S$ -functions establish the continuity of the tangential component of the electric field at a face shared by adjacent elements, making them curl-conforming.

For near-ortho basis functions,  $P$ - and  $S$ -functions are defined as [9, 11, 15]

$$P_i(u) = L_i(u), \\ S_j(v) = \begin{cases} L_0(v) - (-1)^j L_1(v), & j = 0, 1, \quad -1 \leq u, v \leq 1, \\ L_j(v) - L_{j-2}(v), & j \geq 2 \end{cases} \quad (14)$$

where  $L_i$  are Legendre polynomials of order  $i$ .

Max-ortho segment  $S$ -functions,  $S_j$ ,  $j \geq 2$ , can be constructed in the form [15, 16]

$$S_j(v) = L_j(v) - L_{j-2}(v) + D_j S_{j-2}(v), \quad j \geq 2, \quad (15)$$

and recurrent formula for the unknown coefficients  $D_j$  is derived in [16]

$$D_2 = 0, \quad D_3 = 0, \quad D_j = \frac{2j-7}{4j-10-(2j-3)D_{j-2}}, \quad j \geq 4. \quad (16)$$

Max-ortho node  $S$ -functions,  $S_0$  and  $S_1$ , can be constructed in the form [15, 16]

$$S_j^N(v) = L_0(v) - (-1)^j L_1(v) + \sum_{k=2}^N D_j^k S_k(v), \quad j = 0, 1, \quad (17)$$

where  $N$  is an appropriate field-expansion order and  $S_k$ ,  $2 \leq k \leq N$  are max-ortho segment  $S$ -functions from (15). The

recurrent formula for the unknown coefficients  $D_0^k$  and  $D_1^k$ ,  $2 \leq k \leq N$ , is determined in [16]

$$D_j^0 = 1, \quad D_j^1 = (-1)^{j+1}, \quad D_j^k = \frac{2k+1}{2k-3} D_j^{k-2} D_{k+2}, \quad j = 0, 1, \quad 2 \leq k \leq N. \quad (18)$$

Notice that the max-ortho node  $S$ -functions are not mutually orthogonal, and that they are not hierarchical. The fact that these functions are not hierarchical has different practical implications in the FEM and the MoM-SIE, and this will be the subject of our future research. Additionally, in [17] it is shown that high-order Legendre polynomials and their derivatives cannot be calculated precisely simply by linearly combining power functions, and that they should be calculated recurrently. Thus, the max-ortho basis functions should also be calculated recurrently (as they contain Legendre polynomials in our implementation). Based on this, the recurrent formulas (16) and (18) are perfectly suited for efficient and precise calculation of the max-ortho basis functions.

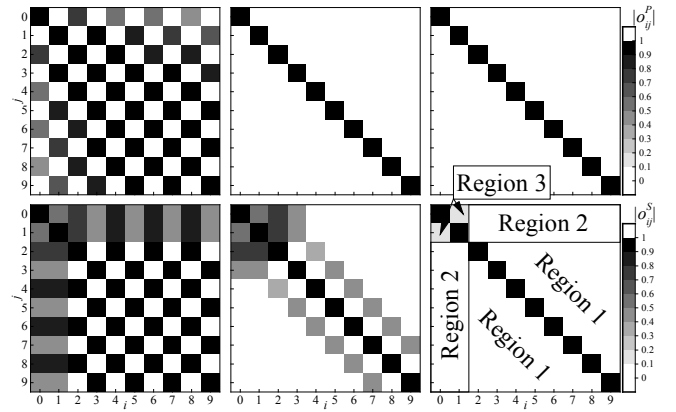


Fig. 2. Matrix form of orthogonality factors  $|o_{ij}^P|$  (top row) and  $|o_{ij}^S|$  (bottom row) for (a) classical, (b) near-ortho and (c) max-ortho basis functions.

Absolute values of orthogonality factors  $o_{ij}^P$  and  $o_{ij}^S$  are plotted in Fig. 2 in the form of a matrix for CLBFs, NOBFs and MOBFs up to the ninth order ( $0 \leq i, j \leq 9$ ), similarly as in [15, 16]. For CLBFs, the matrices of the orthogonality factors  $o_{ij}^P$  and  $o_{ij}^S$  [Fig. 2 (a)] have many non-zero elements, thus the majority of basis functions are not mutually orthogonal. For NOBFs,  $P$ -functions are completely mutually orthogonal and the matrix of the orthogonality factors  $o_{ij}^P$  is an identity matrix [Fig. 2(b)].  $S$ -functions are not completely mutually orthogonal, but, when compared with CLBFs, the matrix of the orthogonality factors  $o_{ij}^S$  is sparser. Finally, as it can be seen from Fig. 2(c), max-ortho  $P$ -functions are completely mutually orthogonal, segment  $S$ -functions are completely mutually orthogonal (Region 1), node  $S$ -functions are completely orthogonal to the segment  $S$ -functions, (Region 2), node  $S$ -functions are not mutually orthogonal (Region 3), and the matrix of the orthogonality factors  $o_{ij}^S$  is the sparsest for the MOBFs. Based on these results, it seems reasonable to

assume that the MOBFs will lead to the smallest condition number of the FEM mass matrix, especially when the mesh consists of electrically large elements with high field-expansion orders.

#### IV. NUMERICAL EXAMPLES

In this section we examine the performance of MOBFs implemented in higher order large-domain FEM technique [6]. We also compare their performance with CLBFs and NOBFs, similarly as in [16]. In all numerical examples, the entries of the mass and stiffness matrices are diagonally normalized [15] by the entries on the main diagonal of the mass matrix and all real and complex numbers are represented in double-precision floating-point format.

As the first example, consider a spherical perfect electric conductor (PEC) scatterer of radius  $a = 1$  m, situated in free space. The scatterer is modeled with six second-order ( $K = 2$ ) truncated square pyramid like elements, as shown in the inset of Fig. 3. These elements have inner radius  $a = 1$  m and outer radius  $b = 1.5$  m with the PEC boundary condition and first-order absorbing boundary condition (ABC) [18] applied to their faces that sit on the scatterer and outer surface, respectively. The scatterer is illuminated by a uniform plane wave. A bistatic radar cross-section (RCS) is calculated at frequency  $f \approx 300$  MHz ( $\lambda_0 = 1$  m being the corresponding wavelength in a free space). For all elements in the mesh, the field-expansion orders in all directions are set to be equal ( $N_u = N_v = N_w = N$ ).

When solving an EM eigenvalue problem (e.g., as in first two examples from [16]), FEM mass and stiffness matrices are kept separately, and a separate condition number can be calculated for each of them. In contrast with this, when solving radiation or scattering problems, FEM mass and stiffness matrices are combined, resulting in a final FEM matrix. As can be seen from Section II, computation of entries in the stiffness matrix includes the curl operator. The curl operator affects the basis functions, and mutually orthogonal basis functions generally are not mutually orthogonal after the curl operator has been applied. This will definitely degrade the orthogonality of the final FEM matrix compared to the orthogonality of the mass matrix. Nevertheless, it is reasonable to expect that max-ortho basis functions will lead to reduction of the condition number of the final FEM matrix compared to all the other types of basis functions.

Fig. 3 shows the condition number of the normalized final FEM matrix for the spherical scatterer. The results for all three types of basis functions are compared. We can see from Fig. 3 that the MOBFs indeed produce the lowest condition number. When the CLBFs are used, the condition number increases rapidly, and it is expected that after reaching a peak, it will remain practically constant, similarly as in [16].

Fig. 4 shows the normalized  $L^2$  error norm of the computed bistatic RCS [19] for the PEC spherical scatterer. In this example, all three types of basis functions yield similar accuracy in computation of the RCS. One of the main

advantages of the max-ortho basis functions in this example would be the smallest condition number, which is a feature highly sought by the iterative solvers [16].

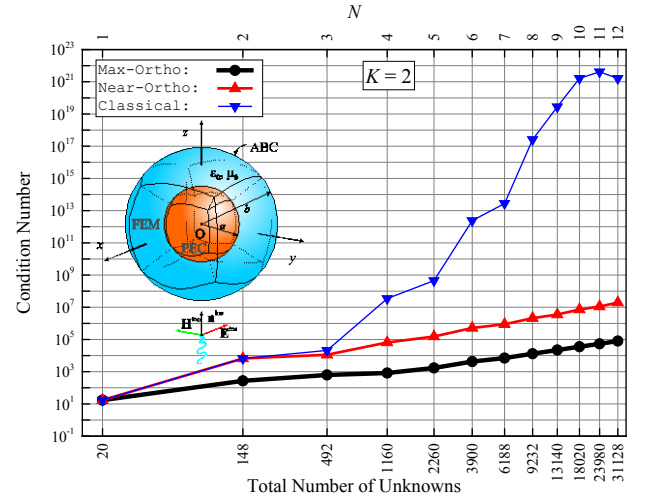


Fig. 3. Condition number of the final FEM matrix for the PEC spherical scatterer; comparison of MOBFs, NOBFs, and CLBFs.

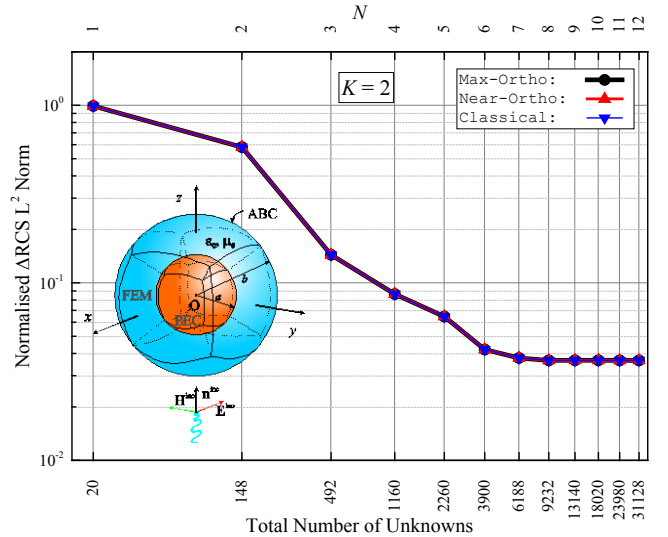


Fig. 4. Normalized  $L^2$  error norm for the computed bistatic RCS of the PEC spherical scatterer; comparison of MOBFs, NOBFs, and CLBFs.

As the second example, consider a waveguide band-pass filter, frequently encountered in engineering practice. The filter consists of an air-filled rectangular PEC waveguide with two PEC stubs in the form of rectangular cuboids. The waveguide is  $c = 50$  mm long with dimensions  $a = 20$  mm and  $b = 10$  mm in the cross-section, as shown in the inset of Fig. 5. The two stubs have a square cross-section,  $a_0 = 2$  mm on a side, and they are set symmetrically in the waveguide. Their axes are separated by  $c_0 = 17.5$  mm.

The filter is meshed with eight trilinear ( $K = 1$ ) elements. For all elements in the mesh, the field-expansion orders in all directions are equal and set to  $N$  ( $N_u = N_v = N_w = N$ ).

Fig. 5 shows the condition number of the final FEM matrix

for all three types of basis functions. We can conclude based on this figure that with  $p$ -refinement [6], the CLBFs lead to a drastic increase of the condition number. On the other hand, the MOBFs have the lowest condition number, whereas the difference in the condition number between the MOBFs and NOBFs is not very large.

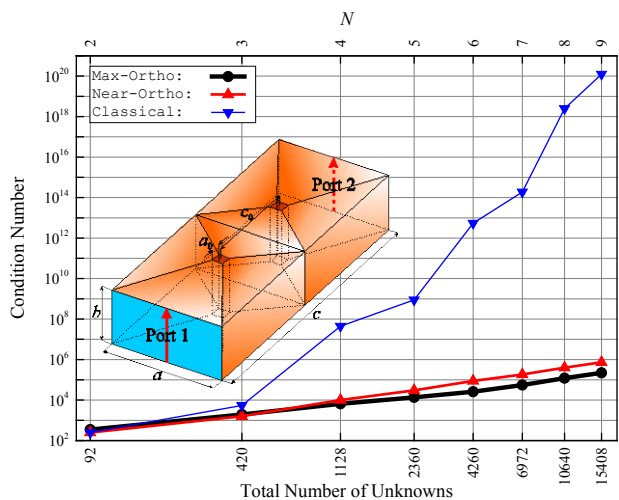


Fig. 5. Condition number of the final FEM matrix for the waveguide band-pass filter; comparison of MOBFs, NOBFs, and CLBFs.

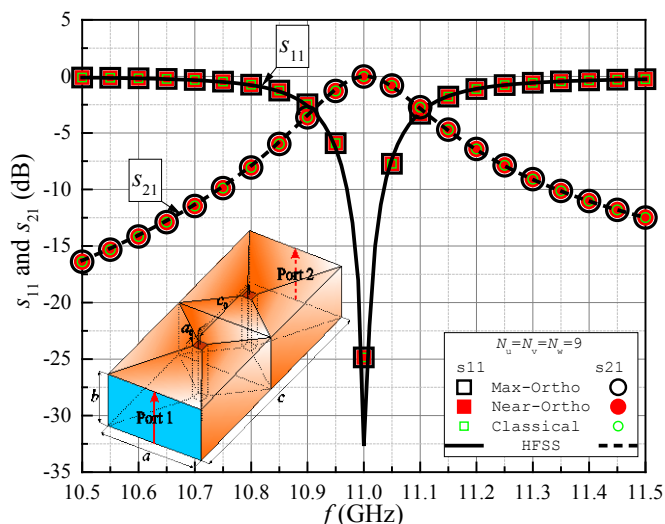


Fig. 6. Scattering parameters of the waveguide band-pass filter; comparison of results obtained by HFSS and by the higher order FEM using MOBFs, NOBFs, and CLBFs.

In order to evaluate the accuracy of the higher-order FEM analysis of the filter and validate the obtained results, we employ a HFSS [20] model for comparison. Fig. 6 shows the comparison of the scattering parameters ( $s$ -parameters) of the filter computed by our higher order FEM (for the dominant mode excitation) and by HFSS (a fully converged solution). For the higher order FEM, all three set of results (for CLBFs, NOBFs and MOBFs) are shown and we can see from the figure that the agreement of the results is excellent.

## V. CONCLUSION

We evaluated the performance of the max-ortho basis

functions in comparison with the classical and near-ortho basis functions using two numerical examples. For the scatterer analysis in open space we combined the max-ortho basis functions with the first order absorbing boundary condition. The results show that the max-ortho basis functions retain their superiority regarding the condition number. We also showed that the max-ortho basis functions lead to the smallest FEM matrix condition number in a waveguide filter analysis problem, which contains geometrically deformed and electrically small finite elements.

## ACKNOWLEDGMENT

The authors acknowledge funding provided by the School of Electrical Engineering Belgrade, through the grants of the Ministry of Education, Science, and Technological Development of the Republic of Serbia.

## REFERENCES

- [1] P. P. Silvester and R. L. Ferrari, *Finite Elements for Electrical Engineers*, 3 ed. New York: Cambridge University Press, 1996.
- [2] J.-M. Jin, *The Finite Element Method in Electromagnetics*. Hoboken, New Jersey: John Wiley & Sons, 2014.
- [3] R. F. Harrington, *Field Computation by Moment Methods* (IEEE Series on Electromagnetic Wave Theory). New Jersey Wiley-IEEE Press, 1993.
- [4] B. D. Popović and B. M. Kolundžija, *Analysis of metallic antennas and scatterers* (IEE Electromagnetic Wave Series 38). London, United Kingdom: The Institution of Electrical Engineers, 1994.
- [5] B. M. Kolundžija, "Electromagnetic Modeling of Composite Metallic and Dielectric Structures," *IEEE Trans. Microw. Theory Techn.*, vol. 47, no. 7, pp. 1021-1032, July 1999.
- [6] M. M. Ilić and B. M. Notaroš, "Higher order hierarchical curved hexahedral vector finite elements for electromagnetic modeling," *IEEE Trans. Microw. Theory Techn.*, vol. 51, no. 3, pp. 1026-1033, March 2003.
- [7] E. M. Klopf, N. J. Šekeljčić, M. M. Ilić, and B. M. Notaroš, "Optimal Modeling Parameters for Higher Order MoM-SIE and FEM-MoM Electromagnetic Simulations," *IEEE Trans. Antennas Propag.*, vol. 60, no. 6, pp. 2790-2801, June 2012.
- [8] B. M. Kolundžija and T. K. Sarkar, "Iterative Solvers in Frequency Analysis of Complex Structures Based on MoM Solution of Surface Integral Equations," in *Proceedings of IEEE Antennas and Propagation Society International Symposium (APS)*, Boston, MA, USA, 2001, pp. 588-591.
- [9] M. M. Ilić and B. M. Notaroš, "Higher Order Large-Domain Hierarchical FEM Technique for Electromagnetic Modeling Using Legendre Basis Functions on Generalized Hexahedra," *Electromagnetics*, vol. 26, no. 7, pp. 517-529, November 2006.
- [10] J. P. Webb, "Hierarchical Vector Basis Functions of Arbitrary Order for Triangular and Tetrahedral Finite Elements," *IEEE Trans. Antennas Propag.*, vol. 47, no. 8, pp. 1244-1253, August 1999.
- [11] E. Jørgensen, J. L. Volakis, P. Meincke, and O. Breinbjerg, "Higher Order Hierarchical Legendre Basis Functions for Electromagnetic Modeling," *IEEE Trans. Antennas Propag.*, vol. 52, no. 11, pp. 2985-2995, November 2004.
- [12] D. S. Sumic and B. M. Kolundžija, "Efficient Iterative Solution of Surface Integral Equations Based on Maximally Orthogonalized Higher Order Basis Functions," in *Proc. in IEEE Antennas and Propagation Society International Symposium (APS)*, Washington, DC, USA, 2005, pp. 288-291.
- [13] B. M. Kolundžija and D. S. Sumic, "Optimal Weights of Basis Functions for Efficient Iterative Solution of Surface Integral Equations," in *Proc. in IEEE Antennas and Propagation Society International Symposium (APS)*, Washington, DC, USA, 2005, pp. 284-287.
- [14] A. F. Peterson and R. D. Graglia, "Scale Factors and Matrix Conditioning Associated With Triangular-Cell Hierarchical Vector Basis Functions," *IEEE Antennas Wireless Propag. Lett.*, vol. 9, pp. 40-43, February 2010.

- [15] M. M. Kostić and B. M. Kolundžija, "Maximally Orthogonalized Higher Order Bases Over Generalized Wires, Quadrilaterals, and Hexahedra," *IEEE Trans. Antennas Propag.*, vol. 61, no. 6, pp. 3153-3148, June 2013.
- [16] S. V. Savić, M. M. Ilić, and B. M. Kolundžija, "Maximally Orthogonalized Higher Order Basis Functions in Large-Domain Finite Element Modeling in Electromagnetics," *IEEE Trans. Antennas Propag.*, vol. 68, no. 8, pp. 6455-6460, August 2020.
- [17] A. J. Krneta and B. M. Kolundžija, "Using Ultra-High Expansion Orders of Max-Ortho Basis Functions for Analysis of Axially Symmetric Metallic Antennas," *IEEE Trans. Antennas Propag.*, vol. 66, no. 7, pp. 3696-3699, July 2018.
- [18] M. M. Ilić, S. V. Savić, and B. M. Notaroš, "First Order Absorbing Boundary Condition in Large-Domain Finite Element Analysis of Electromagnetic Scatterers," in *Proceedings of 10th International Conference on Telecommunications in Modern Satellite, Cable and Broadcasting Services, TELSIKS 2011*, Niš, Serbia, 2011, vol. 2, pp. 424-427.
- [19] S. V. Savić, B. M. Notaroš, and M. M. Ilić, "Accuracy Analysis of the Nonrigorous Second-Order Absorbing Boundary Condition Applied to Large Curved Finite Elements," in *2015 International Conference on Electromagnetics in Advanced Applications (ICEAA)*, Turin, Italy, 2015, pp. 58-61.
- [20] ANSYS. ANSYS HFSS 15.0.0. ANSYS, 2014, <http://www.ansys.com>.

# Method for Estimation of Electrical Distance Between Antennas Based on MUSIC-Type Algorithm

Nikola Basta and Miljko Erić

**Abstract**—A method for estimation of electrical distance between two realistic antennas, based on a MUSIC-type algorithm, is proposed. A simple physical model of the antennas is assembled in a full-wave electromagnetic simulation tool. The synthesized signal accounts for the transfer function between antenna ports, which is extracted from the electromagnetic simulation. The method is verified through comparison with the actual distance within the electromagnetic model and with the computed normalized group-delay.

**Index Terms**—distance measurement; radio positioning; ToA estimation; MUSIC algorithm;

## I. INTRODUCTION

DEVELOPMENT of the global navigation satellite systems (GNSS) and the increase of processing power of the handheld devices was immediately followed by development of indoor positioning systems. Indoor positioning, as well as GNSS, found their way to many commercial, military and safety-of-life applications. In the heart of all positioning algorithms lies the measurement of distance between the transmitter and the receiver, using the information on the signal power, phase or time of arrival (ToA) [1], [2]. The radio ranging algorithms that are based on observation of the time of arrival (ToA) of the signal, actually estimate *electrical* [3] rather than physical distance between the transmitter and receiver antennas. The antennas are often roughly approximated by point radiators, which do not account for propagation of the signal within the antennas themselves. The consequence of this mismodeling is performance degradation of ranging, localization and direction-of-arrival (DoA) estimators. The information on the propagation of the electrical signal in the antennas is carried within the frequency- and angle-dependent phase and group-delay characteristics of the transfer function between the antenna ports [2], [4], [5]. In many cases, this transfer function cannot be measured *in situ*. Since there is a constant demand for high-level positioning accuracy, it is important to revisit the problem of estimation of electrical distance with a careful modeling of the received signal.

In this work we elaborate the signal model and propose a MUSIC-type algorithm [6]–[8] for estimation of electrical distance between two antennas in a typical narrowband ranging

Nikola Basta is with the School of Electrical Engineering, University of Belgrade, 73 Bulevar kralja Aleksandra, 11120 Belgrade, Serbia (e-mail: nbasta@etf.rs).

Miljko Erić is with the School of Electrical Engineering, University of Belgrade, 73 Bulevar kralja Aleksandra, 11120 Belgrade, Serbia (e-mail: meric@etf.rs)

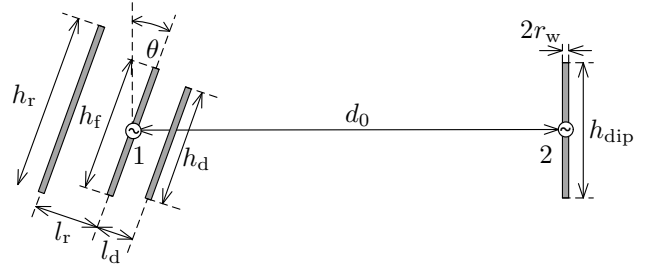


Fig. 1. Half-wave dipole and Yagi-Uda antenna, placed at distance  $d_0$  in the simulated two-antenna scenario.

procedure. In order to assess the error contribution of the ranging algorithm, we compare the estimates to the normalized group delay, derived from the transfer function between the antenna ports that is obtained from an electromagnetic simulation of the scenario.

## II. PROBLEM FORMULATION

We consider a system consisting of a transmitter and a receiver antenna, set apart by physical distance  $d_0$  (Fig. 1). The position of each of the antennas is determined by a fixed point at or close to the geometrical center of the antenna in question. The signal that is being transmitted is a periodic sequence of  $N$  symbols and of bandwidth  $BW$ , modulated at central frequency  $f_c$ . It is assumed that the transmitter and the receiver have perfectly synchronized reference clocks. The problem in focus is estimation of the electrical distance between the antenna ports for different orientations of the transmitting antenna and different sequence lengths  $N$ . The estimation is based on  $M$  transmitted frames of the *a priori* known signal sequence.

## III. ELECTROMAGNETIC SIMULATION SETUP

The setup for the electromagnetic simulation consists of a transmitting three-element Yagi-Uda antenna (port 1) and a receiving half-wave dipole antenna (port 2), placed in vacuum at distance  $d_0 = 5$  m, as shown in Fig. 1. The antennas are realized as wire models in a full-wave solver WIPL-D Pro [9]. They are optimized for operation at central frequency  $f_c = 1$  GHz, from which the central free-space wavelength follows,  $\lambda_c = c/f_c \approx 0.3$  m. The radius of the model wires is  $r_w = \lambda_c/100$ . The Yagi-Uda antenna is inclined by angle  $\theta$  and is defined by the lengths of the reflector, feeder and

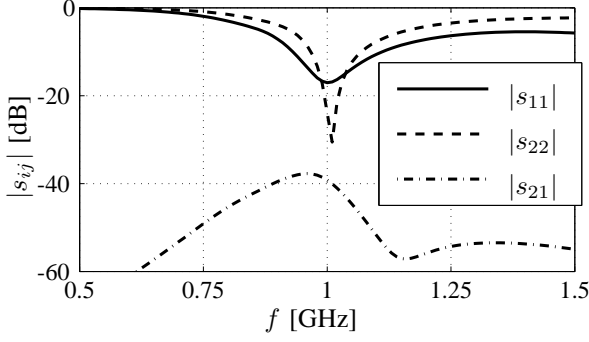


Fig. 2. Scattering parameters of the two antennas for  $\theta = 0^\circ$ .

director elements, respectively:  $h_r = 0.5\lambda_c$ ,  $h_f = 0.44\lambda_c$  and  $h_d = 0.43\lambda_c$ . The reflector and director are placed at distances  $l_r = 0.5\lambda_c$  and  $l_d = 0.2\lambda_c$  from the feeder element, respectively. The length of the receiving dipole is  $h_{\text{dip}} = 0.51\lambda_c$ .

The simulated scattering parameters (reflection and transmission) of the antennas are shown in Fig. 2 for a wide range of frequencies, where we can see that both antennas are well matched at the central frequency. In our study we will particularly observe the band of  $BW = 10$  MHz around  $f_c$ . In order to generate the receiving signal, the forward transmission parameter  $s_{21}(f)$ , i.e. transfer function between ports 1 and 2, has been recorded for different inclination angles  $\theta \in [0^\circ, 75^\circ]$  with a  $5^\circ$  step, and at  $N$  uniformly spaced frequency points within the band of interest, i.e. the set of sample frequencies is defined by  $f_n = f_c - BW/2 + (n-1)BW/(N-1)$ , where  $n \in \{1, 2, \dots, N\}$ . This data will allow us to observe how the signal-processing algorithm handles the angle-dependent phase characteristic of the transfer function. In Fig. 3 example phase and group delay characteristics of  $s_{21}$  are plotted with respect to frequency. The group delay is derived from the transmission parameter

$$\tau_{\text{gd}}(f) = -\frac{1}{2\pi} \frac{d}{df} \arg\{s_{21}(f)\}. \quad (1)$$

#### IV. SIGNAL MODEL AND ESTIMATION ALGORITHM

The proposed bandpass signal consists of a periodic and orthogonal polyphase sequence of complex numbers,  $\mathbf{b} \in \mathbb{C}^{N \times 1}$ ,  $|b_n| = 1$ . Such sequences are usually used in spread-spectrum systems [10]. In our examples, the sequence is transmitted in  $M$  consecutive frames. At the receiver side, the transmitted frame is altered by the transfer function, which includes impact of antennas and of the propagation path, with addition of white noise. Therefore, the  $m$ -th frame received by the half-wave dipole,  $\mathbf{x}_m \in \mathbb{C}^{N \times 1}$ , can be expressed as time-domain (TD) baseband model

$$\mathbf{x}_m = \mathbf{a}e^{j\gamma_m} + \mathbf{n}_m, \quad m = 1, 2, \dots, M, \quad (2)$$

where  $\gamma_m$  is the constant corresponding to the initial phase of the  $m$ -th frame and  $\mathbf{n}_m \in \mathbb{C}^{N \times 1}$  is the noise vector. The vector  $\mathbf{a}$  is given by

$$\mathbf{a} = (\mathbf{TW})^H(\hat{\mathbf{s}}_{21} \odot \hat{\mathbf{b}}), \quad (3)$$

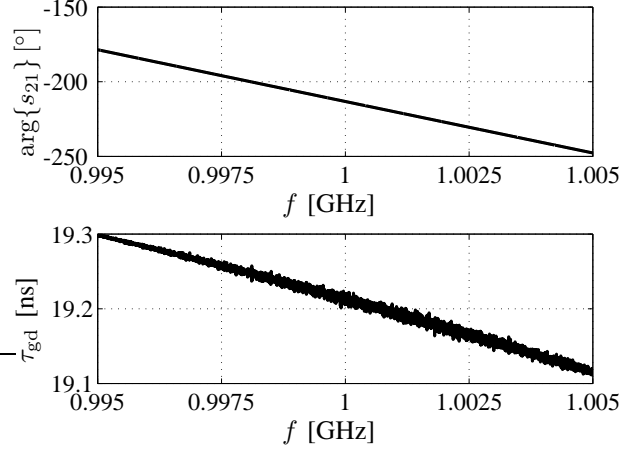


Fig. 3. Phase and group delay of the transmission parameter  $s_{21}$  vs. frequency for  $\theta = 0^\circ$ .

where  $\mathbf{W} \in \mathbb{C}^{N \times N}$  is the discrete Fourier transform (DFT) matrix,  $\mathbf{T} \in \mathbb{R}^{N \times N}$  is the permutation matrix (shifts DC component to the center of the spectrum)

$$\mathbf{T} = \begin{bmatrix} \mathbf{0} & \mathbf{I}_{N/2} \\ \mathbf{I}_{N/2} & \mathbf{0} \end{bmatrix}, \quad (4)$$

$\mathbf{I}_{N/2}$  is the identity matrix of size  $N/2$ ,  $\hat{\mathbf{b}} = \mathbf{TW}\mathbf{b} \in \mathbb{C}^{N \times 1}$  is the frequency-domain (FD) spectrum of the sequence,  $\hat{\mathbf{s}}_{21} \in \mathbb{C}^{N \times 1}$  is the column vector containing samples of the parameter  $s_{21}(f_n)$  for a particular inclination angle  $\theta$  and  $d_0$ . The hat sign denotes FD magnitudes and  $\odot$  represents the Hadamard product.

The comprehensive model of the received signal for an unknown distance  $d$  and angle  $\theta$  would be

$$\mathbf{y}_m = \mathbf{u}_a e^{j\gamma_m} + \mathbf{n}_m, \quad (5)$$

where  $\mathbf{u}_a = (\mathbf{TW})^H(\hat{\boldsymbol{\alpha}} \odot \hat{\boldsymbol{\beta}} \odot \hat{\mathbf{b}})$ ,  $\hat{\boldsymbol{\alpha}} \in \mathbb{R}^{N \times 1}$  is the magnitude spectrum of the transfer function and the elements of  $\hat{\boldsymbol{\beta}} \in \mathbb{C}^{N \times 1}$  are given by  $\hat{\beta}_n = e^{j\phi_n}$ , where  $\phi_n = \phi(f_n)$  is the discrete phase spectrum of the transfer function. Thus, in such a model we have  $2N$  unknown parameters. This large estimation problem can be simplified using following approximations: (i) Since the transmitted sequence is known and its magnitude spectrum is flat [10], we can perform magnitude equalization at the receiver and obtain the equalized signal and its respective model for a single frame as

$$\mathbf{x}_m^{\text{eq}} = (\mathbf{TW})^H(\hat{\mathbf{x}}_m \odot \overline{|\hat{\mathbf{x}}|}) \Rightarrow \mathbf{y}_m^{\text{eq}} = \mathbf{u}_a^{\text{eq}} e^{j\gamma_m} + \mathbf{n}_m, \quad (6)$$

where  $\overline{|\hat{\mathbf{x}}|} = \frac{1}{M} \sum_{m=1}^M |\hat{\mathbf{x}}_m|$  is the mean magnitude spectrum of  $\mathbf{x}$ , the operator  $|\cdot|$  returns the vector of element-wise absolute values,  $\odot$  is the element-wise division and  $\mathbf{u}_a^{\text{eq}} = (\mathbf{TW})^H(\hat{\boldsymbol{\beta}} \odot \hat{\mathbf{b}})$ . (ii) Secondly, since the signal model is narrowband, the phase characteristic is approximated by a linear function, and therefore, according to (1), the group delay is approximated by a constant  $\tau_{\text{gd}}(f) \approx \tau_{\text{gd}}(f_c)$  in proximity of  $f_c$ . It follows that  $\hat{\beta}_n \approx \hat{v}_n(d) = e^{-j\frac{2\pi f_n d}{c}}$ , where it is assumed that  $d \approx c\tau_{\text{gd}}(f_c)$ . Let us define a grid of distances

$d_k, k = 1, 2, \dots, K$ , that correspond to different traveling times of the signal. We can now write the signal model for each point on the grid

$$\mathbf{y}_m^{\text{eq}}(d_k) \approx \mathbf{u}(d_k)e^{j\gamma_m} + \mathbf{n}_m, \quad (7)$$

where  $\mathbf{u}(d_k) = (\mathbf{T}\mathbf{W})^H(\hat{\mathbf{v}}(d_k) \odot \hat{\mathbf{b}})$  and

$$\hat{\mathbf{v}}(d_k) = [e^{-j\frac{2\pi}{c}d_k f_1}, e^{-j\frac{2\pi}{c}d_k f_2}, \dots, e^{-j\frac{2\pi}{c}d_k f_N}]^T \quad (8)$$

is the *delay manifold* vector. This model is justified by the level of collinearity of vectors  $\mathbf{u}$  and *equalized*  $\mathbf{a}$  from (3), given as

$$\mathbf{a}^{\text{eq}} = (\mathbf{T}\mathbf{W})^H(\hat{\mathbf{v}}_c \odot \hat{\mathbf{b}}), \quad (9)$$

where  $\hat{\mathbf{v}}_c(d_k, f_c) = [e^{-j\frac{2\pi}{c}d_k f_c}, \dots, e^{-j\frac{2\pi}{c}d_k f_c}]^T$ . The measure of this collinearity is their scalar product  $\chi(d, \theta, f_c) = \|\mathbf{u}^H \mathbf{a}^{\text{eq}}\| / (\|\mathbf{u}\| \|\mathbf{a}^{\text{eq}}\|)$ . Our simulations show that for the adopted set of parameters  $f_c, BW, \theta$  and  $d_0$ , the collinearity is as high as  $\chi > 0.941$ .

The simplified model in (7) is analogous to the signal model used in spatial (angular) domain for sensor arrays, where  $\mathbf{u}$  corresponds to the steering vector and  $\gamma_m$  to the phase at the reference point of the sensor array. Due to this analogy, the algorithms used for parameter estimation in angular domain, e.g. MUSIC, can be applied in time-frequency domain. In order to apply MUSIC, we define matrix  $\mathbf{X} \in \mathbb{C}^{N \times M}$ , which is obtained by joining together  $M$  signal frames  $\mathbf{x}_m^{\text{eq}}$ , and the estimation of its covariance matrix,  $\mathbf{R}_{\mathbf{X}\mathbf{X}} = \frac{1}{M} \mathbf{X}\mathbf{X}^H$ . Finally, for given  $\theta$ , we can write the MUSIC spectrum as

$$P_{\text{MUSIC}}(d_k) = \frac{\mathbf{u}(d_k)^H \mathbf{u}(d_k)}{\mathbf{u}(d_k)^H \mathbf{Q}_n \mathbf{Q}_n^H \mathbf{u}(d_k)}, \quad (10)$$

where  $\mathbf{Q}_n \in \mathbb{C}^{N \times (N-1)}$  is the noise subspace matrix of  $\mathbf{R}_{\mathbf{X}\mathbf{X}}$  [7] and the denominator  $\mathbf{u}(d_k)^H \mathbf{u}(d_k)$  represents a scaling factor. The estimation of electrical distance between antennas is obtained by

$$\hat{d}(\theta, f_c) = \max_{d_k} \{|P_{\text{MUSIC}}(d_k)|\}. \quad (11)$$

## V. NUMERICAL EXAMPLES

Besides the data acquired from the simulated scenario in Fig. 1, in order to test the algorithm, we define here further parameters of our experiment. We use sequences of different lengths,  $N \in \{16, 64, 256\}$ . Such sequence is repeated  $M = 100$  times. For each inclination angle  $\theta$  we perform 100 estimations of distance  $d$ , while the signal-to-noise ratio is set to  $SNR = 30$  dB. In this study, such relatively high  $SNR$  level is chosen in order to distinguish the imperfections of the transmission channel and of the algorithm from the noise effects. The search space (range) for the estimated distance  $\hat{d}$  directly affects the size of the problem, i.e. the computation time. However, since the physical distance between antennas is known *a priori*, in this work, a range of only 1 m is considered in order to assess the accuracy of the proposed algorithm. Therefore, the chosen grid resolution is  $\Delta d = 0.1$  mm. The results of the MUSIC estimations for  $N = 16$ , as well as the normalized group delay at the central frequency  $c\tau_{\text{gd}}(f_c)$ , are shown in Fig. 4 with respect to  $\theta$ . For each inclination angle, a

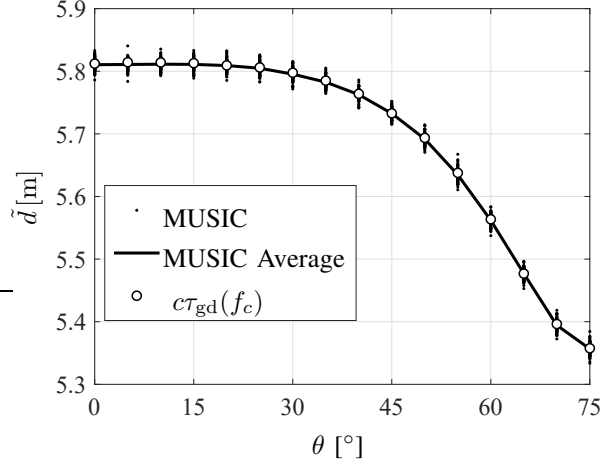


Fig. 4. Estimation of electrical distance between antennas at different inclination angles for  $N = 16$ . The dots represent single estimations, whereas the solid line is estimated average for each inclination angle. Circles are estimation based on the simulated group delay of the transmission channel.

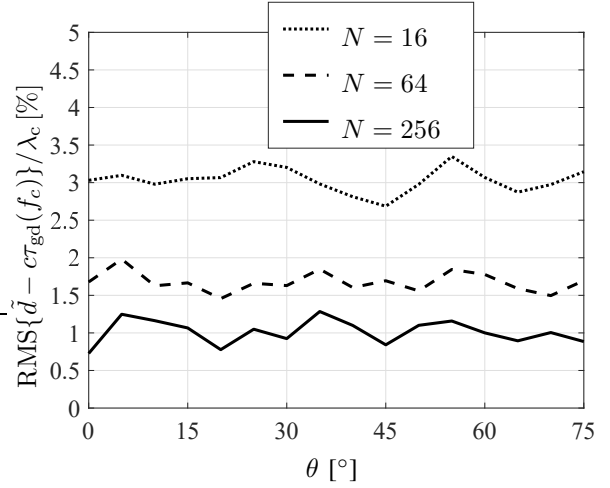


Fig. 5. Normalized root mean square of the estimation error vs. inclination angle for different sequence lengths.

set of estimations is performed, the plot of which are given in dots, whereas their average for the given angle is given in solid line. The root mean square (RMS) of the estimation error with respect to  $c\tau_{\text{gd}}(f_c)$  vs. inclination angle for different sequence lengths is given in Fig. 5.

In the first place, we see in Fig. 4 that the estimation obtained through MUSIC algorithm fits very well to the prediction given by the computed group delay, even for a relatively short sequence, when  $N = 16$ . This verifies the methodology for assessing the algorithm performance, using electromagnetic simulation and proper reference magnitudes. Furthermore, we notice that the relative discrepancy between the simulated physical distance and the normalized group delay is  $|d_0 - c\tau_{\text{gd}}(f_c, \theta)| / \lambda_c \in [1.19, 2.71]$ . This result might seem surprising, knowing that the maximal diameter of the simulated Yagi-Uda antenna is  $0.84\lambda_c$  and that of the dipole is  $0.51\lambda_c$ . In general, the discrepancy stems largely from

the geometrical and electrical properties of the antennas and the environment, which condition the phase characteristic of the total propagation path. The example illustrates effectively the realistic error levels in narrowband ranging applications, in case no calibration of the group-delay bias is available. Finally, in Fig. 5 we observe that the contribution of the algorithm itself to the estimation error is relatively small. Already for  $N = 256$ , the RMS of the error with respect to  $c\tau_{\text{gd}}(f_c)$  approaches 0.75% in terms of  $\lambda_c$ , which corresponds approximately to 2.25 mm. The results in Fig. 5 show that the accuracy doubles if the length of the sequence is increased four times.

## VI. CONCLUSION

A method based on a MUSIC-type algorithm for estimation of the electrical distance between two antennas is proposed. The estimation results are compared to the normalized group delay, obtained from the electromagnetic simulation of the scenario. The obtained ranging accuracy increases linearly with the length of the signal sequence and can reach only a fraction of the free-space wavelength. Due to the group-delay variations and simplifications of the signal model, the estimated electrical distance contains a bias error with respect to the physical distance, which can exceed the size of the antennas. This fact is important in distinguishing properties of the estimation algorithm from the inherent physical properties of the transmission channel.

## REFERENCES

- [1] Y. Gu, A. Lo and I. Niemegeers, A survey of indoor positioning systems for wireless personal networks, in *IEEE Communications Surveys & Tutorials*, vol. 11, 2009, pp. 13-32, 2009.
- [2] G. A. Bartels, GPS-Antenna phase center measurements performed in an anechoic chamber, in *Astrodynamics and Satellite Systems*, vol. 8, Delft University Press, 1997.
- [3] S. R. Best, Distance-measurement error associated with antenna phase-center displacement in time-reference radio positioning systems, in *IEEE Antennas and Propagation Magazine*, vol. 46, pp. 13-22, 2004.
- [4] W. Kunysz, Antenna phase center effects and measurements in GNSS ranging applications, *2010 14th International Symposium on Antenna Technology and Applied Electromagnetics & the American Electromagnetics Conference*, 2010, pp. 1-4, 2010
- [5] V. A. Tischenko, V. I. Tokatly and S. A. Kolotygin, The normalized electrical parameters of the antennas of the navigation apparatus of the users of the global satellite navigation systems, in *Measurement Techniques*, vol. 58, pp. 70-74, 2015.
- [6] C. Morhart and E. M. Biebl, High resolution time of arrival estimation for a cooperative sensor system, *Adv. Radio Sci.*, vol. 8, pp. 61-66, 2010.
- [7] R. Schmidt, Multiple emitter location and signal parameter estimation, in *IEEE Trans. Ant. Prop.*, vol. 34, no. 3, pp. 276-280, 1986.
- [8] H. L. Van Trees, *Detection, Estimation, and Modulation Theory Part IV*, John Wiley and Sons, 2002.
- [9] <http://www.wipl-d.com/products.php?cont=wipl-d-pro>.
- [10] N. Suehiro and M. Hatori, Modulatable orthogonal sequences and their application to SSMA systems, in *IEEE Transactions on Information Theory*, vol. 34, no. 1, pp. 93-100, 1988.

# Trade-offs Between Maximal Forward Gain and Minimal Backward Gain of a Yagi Antenna

Ana Djurdjevic, Dragan Olcan, *Member, IEEE*, and Branko M. Kolundzija, *Fellow IEEE*

**Abstract**—Optimization of Yagi antenna for maximum forward gain and minimal backward gain is conducted. Possible trade-offs between objectives are presented in the form of a Pareto front. It is determined by weighting the cost functions with many different combinations of weighting factors. Antenna solutions are generated by genetic algorithm and evaluated in method of moments based numerical solver, in a frequency range of interest. Our main objective is finding the best compromises between forward and backward gain of Yagi antenna, using the outlined optimization process.

**Index Terms**—backward gain, forward gain, genetic algorithm, Pareto front, Yagi antenna

## I. INTRODUCTION

An optimal design of Yagi antenna that meets required criteria (eg. maximum forward gain, minimum backward gain, maximum front-to-back ratio of gain etc.) is practically impossible to find with analytical methods. Studies of impact of lengths and spacing of elements on the radiation performance leads to a complex nonlinear optimization problem, due to fact that parasitic elements are strongly coupled through electromagnetic (EM) field. With the advancement of the computers and numerical EM algorithms, the optimization has become common approach for design of Yagi antenna.

In earlier research, different optimization techniques based on adjusting elements' lengths and distances are developed in order to exploit maximum forward gain for Yagi antenna [1-3]. As concluded in [2], there exist many local minima in the optimization space, which is defined by the total number of optimization variables and their predefined (given) ranges. Since the introduction of Genetic Algorithm (GA) [4], many researchers utilized its standard form to solve the problem of optimization of Yagi antenna [5-8]. Stochastic GA operators allow the algorithm to find the global minimum in the given optimization space, thus making it a good candidate for this optimization problem.

Having more than one objective leads to a multiobjective optimization, which is intrinsically more complex than the single criterion optimization. In that case, theoretically there is no single best solution, but rather there is a set of Pareto optimal solutions (i.e., a set of the best possible trade-offs among specified criteria). Pareto front for the forward gain maximization and backward gain minimization is estimated using GA and presented in this paper. Note that the side

lobes in the radiation pattern are not considered. Although it might seem that maximization of the forward gain and minimization of the backward gain are the same optimization goal, the numerical results show that these objectives are conflicting. This statement is in agreement with results presented in [9], where a different method is used to estimate Pareto front.

## II. YAGI ANTENNA AND ITS NUMERICAL EM MODEL

The analyzed twelve-element Yagi antenna consists of a driven element, a single reflector and ten directors [10]. The antenna is designed to operate at the central frequency of 300 MHz, and the frequency range of interest is 295 MHz to 305 MHz. EM analysis is performed in WIPL-D software package [11] that is method of moments (MoM) based numerical solver, with higher order basis functions. The optimization is done in an external application, created for the purpose of the presented work. Every element of the antenna is modeled as a wire, forcing kernel to use a thin-wire approximation, which is very fast and sufficiently accurate for the thin wires [8]. The main reason for using thin-wire approximation is to speed up the numerical EM analysis. In every iteration of the optimization, a different set of antenna parameters is provided to WIPL-D kernel for the numerical EM analysis. After the simulation, the obtained output results for antenna gain in forward and backward directions are used to evaluate the cost function used in the optimization. The total number of unknowns in MoM matrix goes up to 36, where the limit is established from the case when the lengths of elements take the highest values from the ranges of optimization variables. With nowadays computers, this is a relatively small-size numerical problem that results in acceptably fast numerical analysis (typically 0.2 s per simulation). The used desktop computer configuration consists of Intel® Core™ i7 CPU 950@3.07 GHz and 24 GB of RAM.

The optimization variables are lengths and spacings between the elements of the Yagi antenna [10]. All the dimensions are chosen from the interval from  $0.2 \lambda$  to  $0.8 \lambda$ , where  $\lambda$  is a free-space wavelength at 300 MHz. Lengths of each director, as well as spacings between the adjacent directors, are kept the same, resulting in the total of six optimization variables. The two considered optimization criteria are: the highest possible gain in the forward direction, and the minimal possible gain in the backward direction.

## III. ALGORITHM USED FOR MULTI-OBJECTIVE OPTIMIZATION

From a general perspective, every optimization algorithm consists of the following steps: creating a starting solution or groups of solutions, evaluating the cost functions of the

Dragan Olcan and Branko Kolundzija are with the School of Electrical Engineering, University of Belgrade, Bulevar kralja Aleksandra 73, 11020 Belgrade, Serbia (e-mail: olcan@etf.rs, kol@etf.rs).

Ana Djurdjevic is with WIPL-D d.o.o., Gandijeveva 7, apt. 32, 11073 Belgrade, Serbia, and she is also a master student at the School of Electrical Engineering, University of Belgrade, Bulevar kralja Aleksandra 73, 11020 Belgrade, Serbia (e-mail: da193305m@student.etf.bg.ac.rs).

current solution(s), checking whether some of the solutions satisfies given criteria, creating a new set of solutions and repeating the process. The optimization stops either if the goal has been achieved or the maximum allowed number of iterations has been attained. In the first case, the solution of the problem is provided to the user. In the second case, the best found solution is provided to the user.

In the problem of finding trade-offs between forward and backward gain of Yagi antenna we are looking for the best possible solution that can be found for the given number of iterations.

The fitness functions for these two objectives are defined as follows:

$$f_1 = A - G_{\text{front}}, \quad (1)$$

$$f_2 = B + G_{\text{back}}. \quad (2)$$

Here  $G_{\text{front}}$  denotes gain in dBi in the forward direction, and  $G_{\text{back}}$  denotes gain in dBi in the backward direction.  $G_{\text{front}}$  is expected to be positive [10], while  $G_{\text{back}}$  should be negative for a good solution from an engineering point of view. The variables  $A$  and  $B$  are positive numbers chosen to be large enough to ensure strictly positive values for both cost functions in all possible cases in the optimization problem. Moreover, a proper choice of the constants makes different criteria comparable in terms of their (numerical) significance, relative one to the other. Combining these two criteria into a single cost function, for the given multicriteria optimization problem, is obtained by summation of (1) and (2) as

$$f = f_1 + f_2. \quad (3)$$

Considering the forms of  $f_1$  and  $f_2$  together with the optimization goals, it is obvious that a lower cost function always points out to a better solution. Formula (3) is calculated in  $N$  equidistant frequency points, so the final cost function is expressed as a root mean square deviation:

$$F = \sqrt{\frac{\sum_{i=1}^N f_i^2}{N}}, \quad (4)$$

where  $f_i$  stands for value of  $f$  at  $i$ -th simulation frequency. Note that in the case of Yagi antenna optimization we use  $N = 5$ .

#### A. Genetic Algorithm

The standard form of GA has been adapted to this problem according to [10]. An individual here refers to a different antenna design solution, described with its variables that are called genes in the GA terminology. The initial population was generated randomly, using uniform random generator.

In the process of the selection, the quality of each solution is examined by evaluating the fitness function (4). Selection operator is realized using tournament selection. In every round, pairs of individuals are randomly chosen to compete in "duels", and the ones that fit better (i.e., the ones that have

lower cost functions) qualify for the next round of the tournament. The tournament ends when the number of not eliminated individuals drops to initially defined number of survivors  $k$ . Survivors are used to create solutions ("offspring") for the next generation. Although the best solutions are being forced in average through the tournament selections, there is a good chance that a solution that might not be in the fittest  $k$  (if we would sort the whole population at once), becomes chosen for crossover just because of having randomly chosen less-fit opponents. This effect is intentional and its purpose is the preserving of certain amount of diversity among the solutions. This is what makes tournament selection significantly different and more applicable in comparison to the pure elitism, which allows only the best individuals to take a part in crossovers.

Once the selection is finished, a crossover is performed. The crossover is a process of recombination parents' genes (optimizing variables), in order to produce solutions for the next generation. Two parents are randomly chosen to create three descendants according to formulas (5), (6) and (7), with predefined probability of the crossover  $P_c = 0.8$ , as in [10]. In other words, this probability represents chances that the two individuals will be used for crossover after being chosen, and will not be discarded.

$$\mathbf{d}_1 = \mathbf{p}_2 + \alpha(\mathbf{p}_1 - \mathbf{p}_2) \quad (5)$$

$$\mathbf{d}_2 = \mathbf{p}_2 - \alpha(\mathbf{p}_1 - \mathbf{p}_2) \quad (6)$$

$$\mathbf{d}_3 = \mathbf{p}_1 + \alpha(\mathbf{p}_1 - \mathbf{p}_2) \quad (7)$$

Here  $\mathbf{d}$  and  $\mathbf{p}$  represent descendant's and parent's chromosomes respectively, both defined as a vector of optimization variable (genes), while  $\alpha$  is a real number, randomly generated from the interval  $[0,1]$  for every crossover. Crossover stops when the number of new solutions are created so that the whole next generation is populated. In attempt to avoid possible multiple convergences to the same local minima in the optimization space, not a single solution from the previous generation is allowed to be used in the next generation.

The mutation operator is realized as a replacement of genes with the randomly chosen values with uniform distribution in the range between the lower and the upper bound for the selected variable. For each gene of each generated solution, mutation is to be executed with the probability  $P_m = 0.15$ . The controlled mutation causes the other parts of optimization space to be explored, which may eventually lead to a better solution. Increasing the probability of mutation degenerates even good solutions, making it more difficult or impossible for GA to converge.

#### B. Pareto Front

In cases of multiobjective problems, there is rarely a solution that dominates all the other solutions with regard to all the criteria. Most often the criteria are conflicting, so it is not possible to make an improvement in one objective without deterioration the others. Pareto front is the set of the best possible trade-offs that can be theoretically achieved, and it is defined by an infinite number of Pareto-optimal solutions, if the optimization space is continuous and if the criteria are defined as real-number functions. A solution is

pareto optimal if there is no other solution in the search space that has better performances for all the given objectives [10], [12]. Pareto front provides deep insight into compromises that should be made for the sake of overall performance, hence one can choose the most suitable solution for a problem under consideration.

The aim of this work is to present the best found compromises between the maximum gain in the forward direction and the minimum gain in the backward direction for Yagi antenna described in Section II. The method starts with weighting the penalties for cost functions (1) and (2), thus increasing the importance of one or the other criterion in the cost function. Now the total cost function becomes:

$$f_{\text{tot}} = w_1 f_1 + w_2 f_2 \quad (8)$$

By replacing  $f_{\text{tot}}$  in (4) with expression from (8), the final cost function used in the optimization yields to:

$$F_{\text{tot}} = \sqrt{\frac{\sum_{i=1}^N (w_1 f_{1,i} + w_2 f_{2,i})^2}{N}}, \quad (9)$$

where  $f_{1,i}$  and  $f_{2,i}$  denote values of (1) and (2) on  $i$ -th frequency.

In order to decrease the cost function defined above, the optimization will tend to produce solutions which minimize the cost function that is associated with higher weighting coefficient, relative to the ratio of (1) and (2). Roughly speaking, the ratio of the separate cost functions in the final solution is expected to be proportional to the ratio of their weighting coefficients. From that perspective, it is clear that  $A$  and  $B$  in the definitions for  $f_1$  and  $f_2$  should be chosen carefully, since they directly influence the final cost function. It should also be noted that values of the forward and the backward gain that are summed here, significantly differ for various antennas.

In order to determine the Pareto front accurately, the optimization needs to be performed for all possible combination of  $w_1$  and  $w_2$  [12]. The theoretical number of those combinations is infinite. For that reason, only few extreme scenarios are enough to get an engineering insight into the distribution of the optimal solutions, i.e., to estimate the Pareto front.

#### IV. ANTENNA OPTIMIZATION AND RESULTS

The parameters used in GA are as follows: the population has 16 solutions, 4 selected solutions from the population creates the next generation, the total number of generations is 100. One iteration is an evaluation of the cost function, so there are 1600 iterations in a single optimization run, i.e., to find the cost functions for all solutions in one generation of GA. The variable  $A$  in  $f_1$  is chosen to be 20 dBi, and  $B$  in  $f_2$  is chosen to be 50 dBi. These values are determined to be related to the gain of the best-found solutions when the algorithm was run solely for the front and the back gain, as shown in Fig. 1. and Fig. 2. The total number of frequency points in EM analysis and the optimization is 5. The sets of weighting coefficients used for finding the Pareto front are  $(w_1=0, w_2=1)$ ,  $(w_1=1, w_2=0)$ ,  $(w_1=1, w_2=1)$ ,  $(w_1=1, w_2=2)$ ,

$(w_1=2, w_2=1)$ ,  $(w_1=1, w_2=3)$ ,  $(w_1=3, w_2=1)$ ,  $(w_1=1, w_2=5)$ ,  $(w_1=5, w_2=1)$ ,  $(w_1=1, w_2=10)$ ,  $(w_1=10, w_2=1)$ ,  $(w_1=1, w_2=100)$ ,  $(w_1=100, w_2=1)$ . For each pair of weighting factors, GA is restarted 10 times, and the best-found solutions from every run are presented as the results.

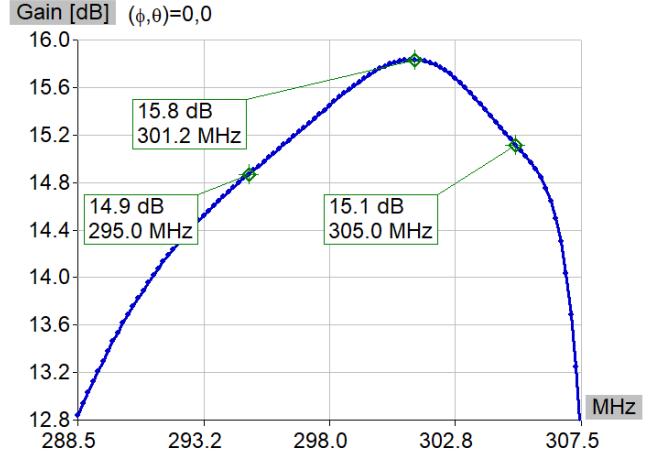


Fig. 1. Gain in forward direction in terms of frequency, obtained for  $(w_1=1, w_2=0)$

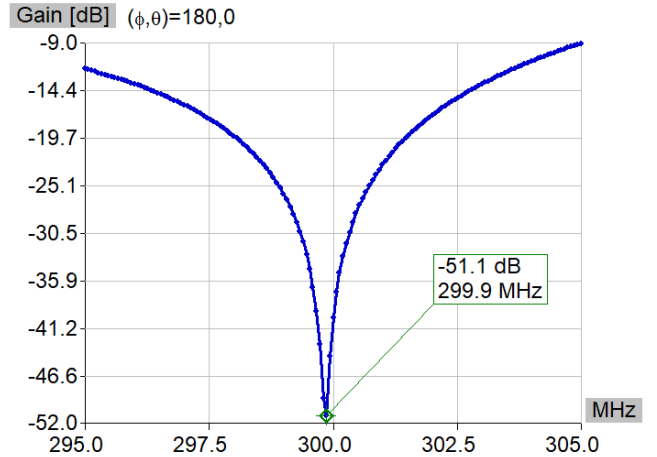


Fig. 2. Gain in backward direction in terms of frequency, obtained for  $(w_1=0, w_2=1)$

Two new variables,  $x$  and  $y$ , are presented in Fig. 3 and they are defined as root-mean-square of the forward and backward gains as:

$$x = \sqrt{\frac{\sum_{i=1}^N (A - G_{\text{front},i})^2}{N}} \quad (9)$$

$$y = \sqrt{\frac{\sum_{i=1}^N (B + G_{\text{back},i})^2}{N}}, \quad (10)$$

where  $G_{\text{front},i}$  and  $G_{\text{back},i}$  stand for values of gain on  $i$ -th frequency, and  $N = 5$ .

It can be seen from Fig. 3 that those solutions found for same weighting factors in different optimization runs are pretty much grouped on the graph and they converge to one part of the Pareto front. It is observed that some solutions on the Pareto front which would make the curve smoother were not found in the given number of iterations. A better Pareto front approximation could certainly be achieved by

additional adjusting of weighting factors and more optimization runs.

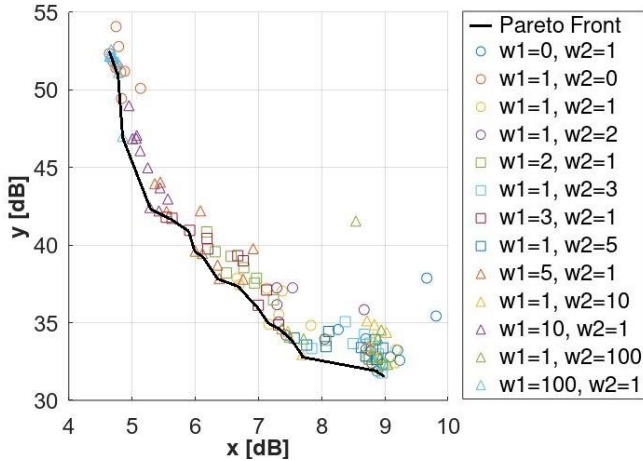


Fig. 3. Pareto Front in terms of root mean square deviations for best-found solutions in frequency range 295 to 305 MHz.

As it is shown in Fig. 2, bandwidth where the front gain is less than 3 dB reduced from the maximum value is about 19 MHz wide. However, in Fig. 3 it is shown that the suppression of the backward lobe has extremely narrow bandwidth, with more than 40 dB differences with frequency shift of 5 MHz, in this case. Therefore, the best-found solutions in terms of average values of gain in the given range are presented in Fig. 4.

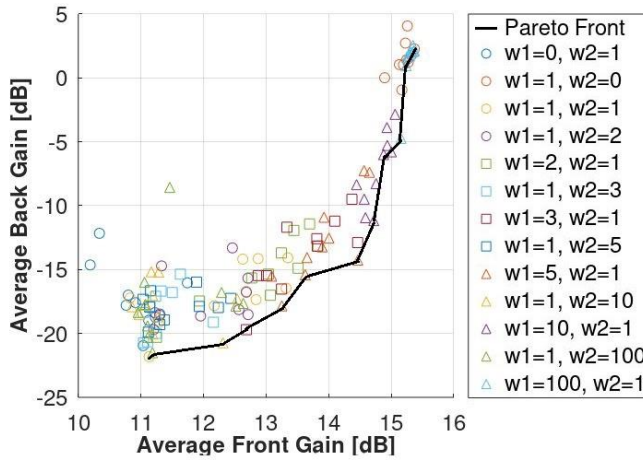


Fig. 4. Pareto Front in terms of average values of gain for best-found solutions in frequency range 295 MHz to 305 MHz.

It can be seen from Fig. 4. that it is possible to keep the average back gain of about -20dBi, up to average front gain of about 12.5 dBi. With further increment of front gain, back gain increases rapidly, entering zone where the objectives start to be more mutually conflicting. Due to the physical nature of the problem, the performances are better in a very narrow bandwidth, as can be seen in Fig. 1 and Fig. 2. Radiation pattern at 300 MHz in H and E plane for one of optimal solutions are given in Fig. 5. and Fig. 6.

## V. CONCLUSION

The best compromises between maximization of gain in the forward direction and minimization of the gain in the backward direction, for twelve-element Yagi antenna in frequency range 295 MHz to 305 MHz are presented and

analyzed in this work. It is shown that in order to achieve value of front gain close to maximum possible, one should sacrifice suppression of back lobe level. However, there are numerous optimal solutions for relatively low level of backward radiation, with not so high deviation of front gain from its maximum value. It is also observed that much greater front-to-back ratio could be found in one frequency point, but it is question of significance of these solution when it comes to practical realization and operation of the antenna. Genetic Algorithm used for optimization is confirmed to be suitable for this multi minima optimization problem.

## ACKNOWLEDGMENT

The authors acknowledge funding partially provided by the School of Electrical Engineering Belgrade, through the grants of the Ministry of Education, Science, and Technological Development of the Republic of Serbia.

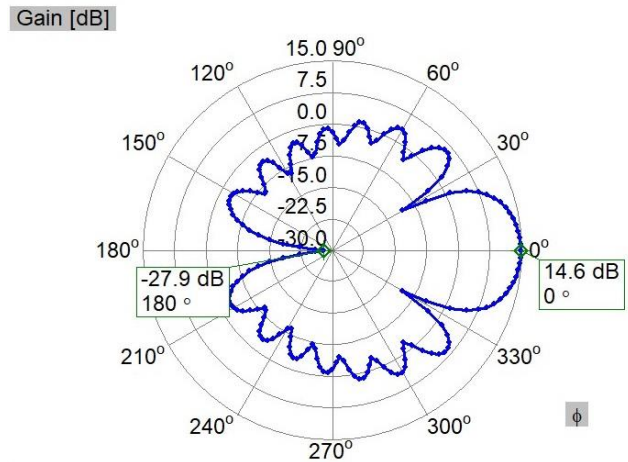


Fig. 5. Gain on 300 MHz in H-plane for one of optimal solutions

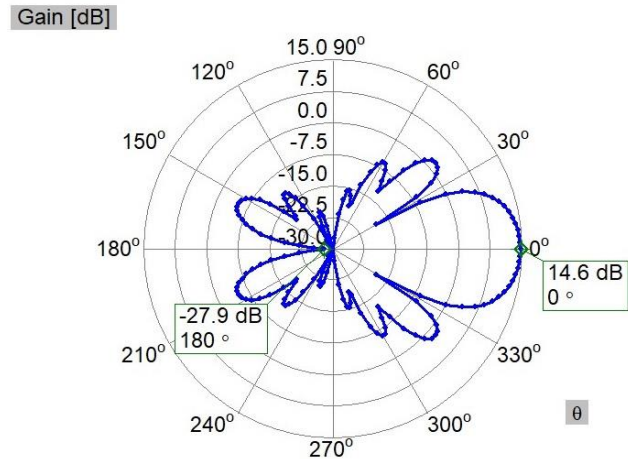


Fig. 6. Gain on 300 MHz in E-plane for one of optimal solution

## REFERENCES

- [1] H. W. Ehrenspeck and H. Poehler, "A new method for obtaining maximum gain from Yagi antennas," *IRE Trans. Antennas Propagat.*, vol. AP-7, pp. 379–386, Oct. 1959.
- [2] D. K. Cheng, "Gain optimization for Yagi-Uda arrays," *IEEE Antennas Propagat. Mag.*, vol. 33, pp. 42–45, June 1991.
- [3] J. H. Bojsten, H. Schaer-Jacobsen, E. Nilsson, and J. B. Anderson, "Maximum gain of Yagi-Uda arrays," *Electron. Lett.*, 7, no. 18, pp. 531–532, September 9, 1971
- [4] J. H. Holland, *Adaptation in natural and artificial systems, an introductory with applications to biology, control, and artificial intelligence*, The MIT Press, 5th Edition, 1992.
- [5] E. A. Jones and W. T. Joines, "Design of Yagi-Uda Antennas using

- Genetic Algorithms," *IEEE Transactions on Antennas and Propagation*, vol. 45, no. 9, pp. 1386–1392, 1997.
- [6] H. J. Wang, K. F. Man, C. H. Chan, and K. M. Luk, "Optimization of Yagi array by Hierarchical Genetic Algorithms," *Proc. of IEEE Radio and Wireless Conference, 2003. RAWCON '03*, pp. 91–94, 2003.
- [7] Y. Kuwahara, "Multiobjective Optimization Design of Yagi-Uda Antenna," *IEEE Transactions on Antennas and Propagation*, vol. 53, no. 6, pp. 1984–1992, 2005.
- [8] B. M. Kolundzija, and A. R. Djordjevic, *Electromagnetic Modeling of Composite Metallic and Dielectric Structures*, Artech House, Norwood, 2002.
- [9] M. Modaresi, L. Shafai and B. Lindmark, "Efficient optimization of a Yagi-Uda antenna using genetic algorithm," *11th International Symposium on Antenna Technology and Applied Electromagnetics [ANTEM 2005]*, pp. 1-4, 2005.
- [10] B.M. Kolundzija, D.I. Olćan, "Multiminima heuristic methods for antenna optimization," *IEEE Transactions on Antennas and Propagation*, Vol. 54, No. 5, pp. 1405-1415, May 2006.
- [11] WIPL-D Pro CAD 2019, WIPL-D d.o.o, Belgrade, 2019.
- [12] D. S. Weile, E. Michelssen, and D. E. Goldberg "Genetic Algorithm Design of Pareto Optimal Broadband Microwave Absorbers," *IEEE Trans. on Electromagnetic Compatibility*, Vol. 38, NO. 3. August 1996.

# The Influence of Different Realization of Ground Plane on a Characteristic of HFSWR Transmitter Monopole Array

Nemanja Grbić, *Member, IEEE*, Pavle Petrović, *Member, IEEE*, Ana Čupurdija, Nikola Lekić  
*Member, IEEE* and Slobodan V. Savić, *Member, IEEE*

**Abstract**—Mutual coupling of antennas in systems that use multiple antennas is a phenomenon that can be detrimental to a system's functionality. Mutual coupling of antennas in an existing High Frequency Surface Wave Radar (HFSWR) transmitter is analyzed in this paper. Earlier measurements of VSWR had indicated that significant coupling may be present. After various simulations, its presence was confirmed, and it was shown that the simulated radiation pattern has differences compared to the theoretical. In this paper, simulations were performed to analyze the effects of different realization of ground planes on antenna coupling and its effect on radiation pattern while keeping the deployment area and antenna foundations intact. The nature of the coupling was analyzed along with different realizations of ground planes. Simulation results are presented and discussed in details, showing that coupling through the free space is dominant in nature of this effect.

**Index Terms**—Ground Realization, HFSWR, Monopole, Mutual Coupling.

## I. INTRODUCTION

Economies are becoming heavily reliant on overseas shipping making maritime traffic denser than ever. Without going further into the significance of maritime areas, the Exclusive Economic Zone (EEZ) is where it practically all takes place. The EEZ is a strip of sovereign water going 200 nautical miles (around 370 km) from the coastline to the open sea [1]. To control such a large area, an efficient surveillance system is needed, which is no easy feat. Microwave radars and electro-optical systems can only bypass the curvature of the earth using mobile platforms, this solution does not have a satisfactory uptime, nor operational cost.

In contrast to that, high frequency surface wave radar (HFSWR) is a system that satisfies mentioned needs. HFSWR is a radar that works in the High Frequency (HF) band ranging from 3 MHz to 30 MHz [2-3]. These frequencies allow propagation of electromagnetic (EM)

surface waves closely coupled to some surface, in this case seawater. Initially, they were used for oceanographic observations such as the height and direction of waves, speed and direction of currents, as well as tsunami detection [2-4]. Such waves follow the curvature of the earth, allowing for detection well beyond the horizon, going as far as 370 km, which is a requirement for complete EEZ observation [5-6].

The analysis presented in this paper is inspired by experience gained from currently operating system in the Gulf of Guinea [6-9], which represents the backbone of a complex multi-layer system for maritime surveillance [10]. It is a frequency-modulated continuous-wave (FMCW) radar occupying a 100 kHz bandwidth with central frequency at 6.9 MHz. The system is comprised of 2 separate sites, transmitter (Tx) and the Receiver (Rx). The receiver is an antenna array consisting of 16 monopole antennas. The transmitter is made of 4 quarter-wave monopole antennas, as illustrated in Fig 1. Further details regarding this radar can be found in [6-8].

Certain measurements of this radar have raised suspicion of significant mutual coupling between transmitter antennas. Different realizations of ground plane and its influence on the coupling of antennas will be discussed.



Fig. 1. Transmitter site located in the Gulf of Guinea.

Section II contains a brief introduction to the problem of mutual coupling of antennas, and all relevant data for used numerical models will be presented. Section III will present several numerical models of the ground plane and its effects on antenna array performance. Conclusions are presented in Section IV.

Nemanja Grbić, Pavle Petrović and Ana Čupurdija are with the School of Electrical Engineering, University of Belgrade, 73 Bulevar kralja Aleksandra, 11020 Belgrade, Serbia and with the Vlatacom Institute, Belgrade, Bulevar Milutina Milankovića 5, 11070 Novi Beograd, Serbia (e-mails: nemanja.grbic@vlatacom.com, pavle.petrovic@vlatacom.com and ana.cupurdija@vlatacom.com).

Nikola Lekić – is with the Vlatacom Institute, Belgrade, Bulevar Milutina Milankovića 5, 11070 Novi Beograd, Serbia (e-mail: nikola.lekic@vlatacom.com).

Slobodan V. Savić is with the School of Electrical Engineering, University of Belgrade, 73 Bulevar kralja Aleksandra, 11020 Belgrade (e-mail: ssavic@etf.bg.ac.rs).

## II. MUTUAL COUPLING

Mutual coupling between array elements can be separated as a free-space coupling (radiation coupling) and/or coupling through currents flowing on the ground plane shared by these elements (conductive coupling) [11-13]. Regardless of its nature, the mutual coupling of array elements generally affects radiation pattern and the input impedance of array.

As can be seen from Fig. 1, the transmitting array consists of 4 antennas arranged to be corners of a rectangle. The side facing the shoreline is  $0.5\lambda$ , while the side perpendicular to it is  $0.15\lambda$ , where  $\lambda$  is the free space wavelength at 6.9 MHz. The  $0.15\lambda$  separation is of particular importance since it is believed that it is the main reason for mutual coupling.

VSWR measurement was performed for individual antennas and the splitter that feeds them. VSWR measured for each antenna was below 1.5 at 6.9 MHz, as shown in Fig. 2 for one of the antennas. For this measurement, one antenna is excited while all others are closed with loads. In the second measurement, all transmitting antennas are fed by a 1:4 splitter, and then VSWR at the input of splitter is measured. As can be seen from Fig. 2, in this case, the VSWR was 3 and practically flat in a 200 kHz span around 6.9 MHz. The splitter is declared to have VSWR less than 1.1. Because of this, it was suspected that antennas are (significantly) mutually coupled.

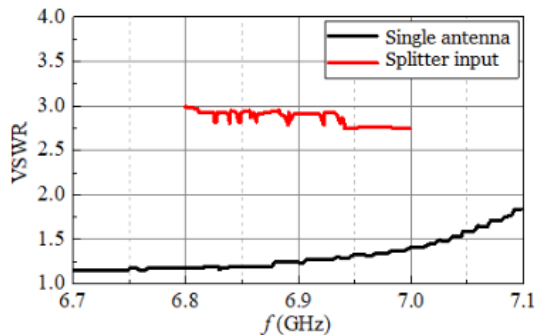


Fig. 2. VSWR measured for one antenna (black) and the input of a 1:4 splitters connected to 4 antennas.

This prompted further analysis, and simulations were performed using the software package WIPL-D Pro [14]. All WIPL-D Pro simulations were performed at 6.9 MHz. To demonstrate the mutual coupling, the initial model was made with vertical monopoles arranged exactly the same as those for the transmitter of HFSWR in the Gulf of Guinea. However, to simplify the model, the ground for the monopoles is made as an infinitely large perfect electric conductor (PEC) plane. The excitation of the front row of antennas (3 and 4), closer to the sea, is delayed for  $126^\circ$  to simulate longer feed cables compared to those that excite the back row of antennas at the site in the Gulf of Guinea. This was done in order to get a null in radiation pattern away from the sea (direction of  $270^\circ$ ), while having a sufficiently wide main lobe. Common antenna array theory was used for this calculation [15-16]. The theoretical model was also derived from these calculations. It implies monopoles with infinite PEC ground plane without mutual coupling. Fig. 3. shows the overlay of the theoretical radiation pattern versus the WIPL-D Pro results. Both of the given radiation patterns are obtained when all 4 antennas are active while being

normalized to 0 dB, meaning that they are not absolute values.

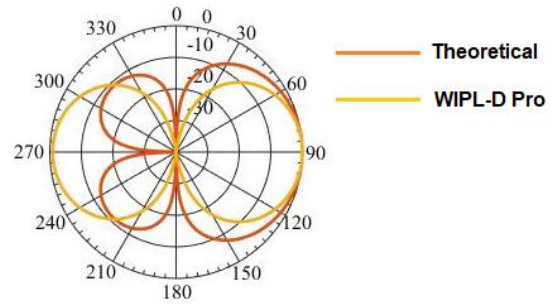


Fig. 3. Overlay of theoretical radiation pattern (red) versus WIPL-D Pro results (yellow) when all 4 antennas are active.

The sideways null in results has a purpose of preventing the signal leakage from transmitter directly to the receiver, and it is fairly equal in both models. However, the null away from the sea has drastic differences. Using the WIPL-D Pro software, it is shown that there is a significant lobe in the direction of  $270^\circ$ . It seems reasonable to assume that  $0.15\lambda$  spaced monopoles are strongly coupled, which changes radiation pattern relative to theoretical.

In models with multiple excitations, WIPL-D Pro allows analysis when only one excitation is active at a time while the others are terminated with a short circuit. This short circuit is not consistent with the measurement set up and the real system. To remedy this, all non-excited antennas are terminated with a concentrated load of  $50\ \Omega$ . This is shown in Fig. 4, where only one antenna has an active excitation. The displayed radiation pattern is shown for the horizontal cut. From this result, we see that other (non-excited) antennas affect radiation pattern, since the monopole antenna has an omnidirectional radiation pattern. It is important to note that WIPL-D presents the radiation pattern from the center of the coordinate system, regardless where the excitation is.

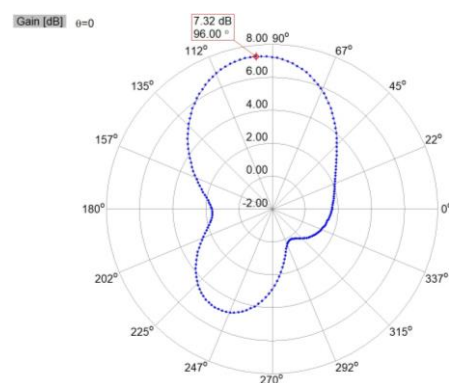


Fig. 4. Radiation pattern in the horizontal cut of a singly excited antenna in the transmitting array in the vicinity of all others antennas.

Looking at the  $s$ -parameters, in this case, off-diagonal elements of  $s$ -matrix, it can be seen that monopoles have significant coupling (especially  $s_{41}$ ), as shown in Table I. Antenna numeration (A1-A4) is counter-clockwise starting from the left antenna farther from the sea, meaning 1-2-3-4 counter-clockwise from that antenna, as shown in Fig. 1. Keep in mind that this analysis is reciprocal and that the array has a plane of symmetry.

TABLE I  
S-PARAMETER MAGNITUDES BETWEEN EACH ANTENNA FOR INFINITE PEC GROUND

$ \underline{s}_{41} $	-6.9350 [dB]
$ \underline{s}_{42} $	-20.7820 [dB]
$ \underline{s}_{43} $	-17.5511 [dB]

In these kinds of implementations, ideally, parameters from Table I should be zero to ensure the desired performance. Also note that  $s$ -parameters of  $0.5\lambda$  spaced antennas ( $s_{42}$  and  $s_{43}$ ) are more than 10 dB lower in amplitude, meaning that the coupling effect is of lesser intensity. This clearly signifies that mutual coupling in this model is a consequence of antennas being too close to each other. At first glance, a simple solution would be to simply separate antennas further and calculate the necessary phase shift. However, a larger site is not an option. For HFSWR in the Gulf of Guinea, it is very difficult to find and then obtain, suitable land, especially due to the rising costs of coastal land. It is also worth mentioning that sometimes increasing antenna separation can increase coupling [13].

In this paper, analysis will be made on effects of different ground planes on the mutual coupling of antennas without changing the size of the transmitter allocated area, or drastically changing the array configuration. The area allocated for a transmitter in the Gulf of Guinea is approximately 92 m x 76.5 m, with the wider side being parallel to the sea. In Fig 5. the WIPL-D Pro model with a finite PEC ground can be seen. It should be noted that the allocated area is in fact the area for the ground plane for the transmitter array.

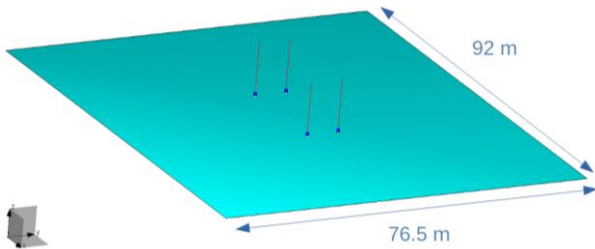


Fig. 5. Finite PEC ground model cut into 4 plates.

### III. SIMULATION WITH DIFFERENT GROUND PLANES

Since the initial request is to keep the same antenna separation, there is very little that can be done against free-space coupling. This leaves the possibility to reduce mutual coupling via manipulations of currents flowing through the ground plane. Previous WIPL-D Pro model has an infinite PEC plane as ground, which obviously cannot be constructed in practice, but represents a good starting point. The first modification will consist of a finite PEC plane with dimensions equal to space allocated for the transmitter site, as mentioned in the previous chapter. The magnitudes of  $s$ -parameters in dB of such a configuration are presented in Table II.

TABLE II  
S-PARAMETER MAGNITUDES BETWEEN EACH ANTENNA FOR FINITE PEC GROUND

$ \underline{s}_{41} $	-7.3780 [dB]
$ \underline{s}_{42} $	-22.1203 [dB]
$ \underline{s}_{43} $	-17.3683 [dB]

Compared to the results from Table I, it can be seen that coupling is now slightly reduced, but practically it remains the same. The next step is to look at current distributions for finite PEC ground model. Please note that all further figures regarding current distribution display current density amplitude.

The current distribution of a finite PEC ground model when only excitation 4 is active is shown in Fig. 6. It can be seen that there is a considerable current at antenna 1 feed point, while much less at feed points 2 and 3. The unit of current density displayed is mA/m.

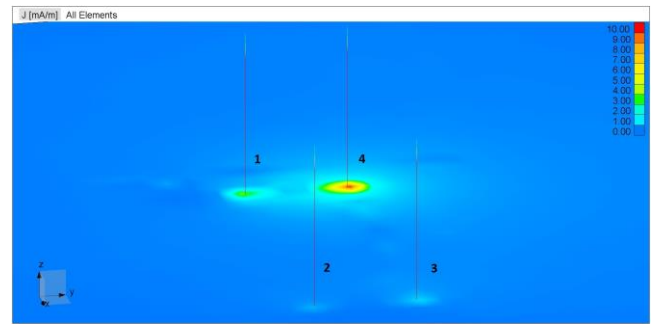


Fig. 6. Current distribution for finite PEC ground model when only generator 4 is active.

From this analysis, it is difficult to discern the exact ratio of contribution of current and free-space coupling. Antennas 4 and 1 have significant currents in the sector of a ground plane between them. The next step in order to try to reduce coupling is to galvanically separate all the antennas. The idea is to separate the current finite PEC into 4 equal plates, as shown in Fig. 7. The width of all slits is 2 m, which was chosen as to have an adequate graphical presentation.

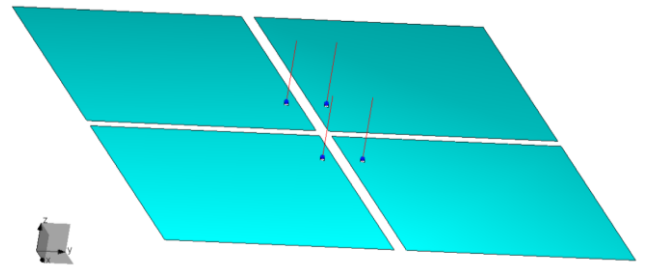


Fig. 7. Finite PEC ground model cut into 4 plates.

Next, we will determine how  $s$ -parameters depend on the width of the slit. A sweep was done with slit width ranging from 0.5 m to 3 m in increments of 0.5 m. The results are shown in Fig 8. The abscissa of Fig. 8 is a separation width value, and the ordinate is the linear magnitude of  $s$ -parameters. Four curves displayed represent magnitudes of  $|\underline{s}_{41}|$ ,  $|\underline{s}_{42}|$ ,  $|\underline{s}_{43}|$  and  $|\underline{s}_{44}|$  shown in blue, red, purple and green respectively in [dB].

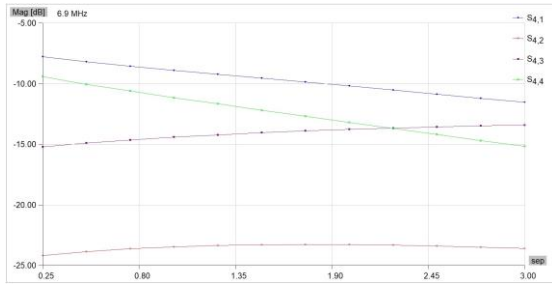


Fig. 8.  $S$ -parameter magnitude in respect to the slit width.

From Fig. 8 it can be seen that the coupling of the nearest antennas ( $s_{41}$ ) is reduced as slit width increases. The coupling of the diagonal antenna ( $s_{42}$ ) remains practically unchanged. Interestingly enough, coupling for  $0.5\lambda$  separated antennas ( $s_{43}$ ) slightly increases with slit width increase. The next step is to see the current distribution. Results for slit width equal to 2 m are presented in Fig. 9. Again, only generator 4 is active.

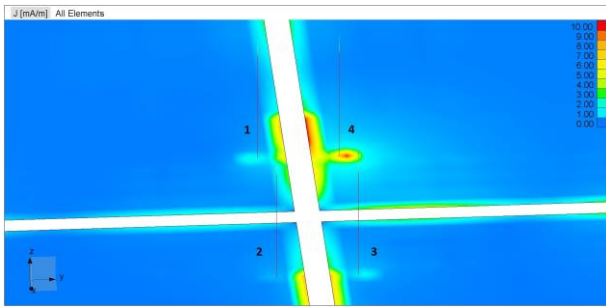


Fig. 9. Current distribution for finite PEC ground model with slit when only generator 4 is active.

Fig. 9 shows interesting results. There are significant currents on all four plates' edges, implying a strong radiation coupling since there is no galvanic contact between these plates. The horizontal cut of the radiation pattern when all four generators are turned on is shown in Fig. 10.

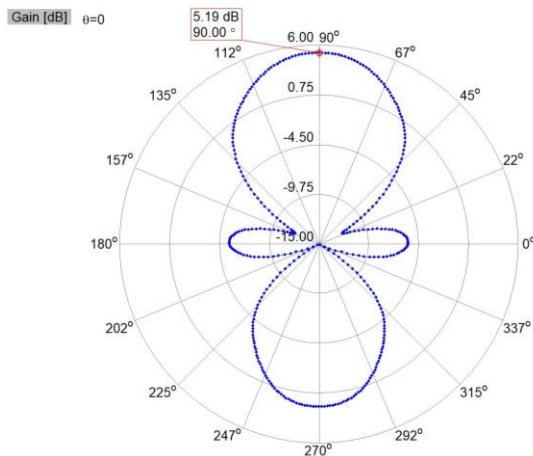


Fig. 10. Radiation pattern in the horizontal cut of finite PEC ground model with slit with all 4 active generators.

From the Fig. 10, we can see that there is significant radiation directly above the antennas, going up to 3 dBi. The back-lobe intensity is about 3 dB lower than the frontal main

lobe which is 5.19 dBi. This solution proves to be energy-inefficient because a significant portion of the energy is radiated upwards, providing no benefit for HFSWR analyzed in this paper. In fact, this occurrence can degrade radar operation as it allows for significant ionospheric reflections which for this type of system are interference. Based on this, one should be very careful when attempting this kind of antenna decoupling.

Final analyzed realization of ground for the monopoles will be in the form of radials. Radials are wires going from the feed point of the antenna and act as a ground plane for it. They are galvanically connected to the “cold” conductor of the transmission line, in this case, coaxial cable. Their purpose is to increase the radiation efficiency of an antenna by preventing losses in the earth, which is far from a perfect conductor. Increasing the number of radials and their length acts as a better ground. The transmitter of HFSWR in the Gulf of Guinea has 36 radials per monopole, with 35 m of length. This length is greater than the distance between each transmitting antenna, especially for distances of antenna pairs 1-4 and 2-3. Because wires in the WIPL-D Pro model must not have unspecified intersections to ensure an appropriate model, radials should be carefully modeled. The radials placed on the real site are not symmetrically placed around the monopole itself. A reason for this is to fit all wires and to enable movement of personnel on-site. It should be noted that all of them are galvanically isolated with rubber. Therefore, the transmitter is modeled as close as possible to the deployed antenna array. Antennas 1 and 3 are rotated  $5^\circ$  around their monopoles, while antennas 2 and 4 have no rotation. Furthermore, all antenna feed points are slightly elevated, all to prevent wire intersection, and this model is presented in Fig. 11.

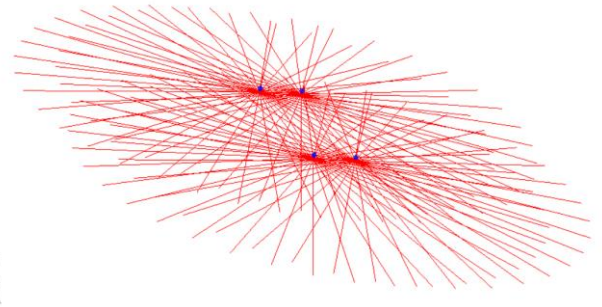


Fig. 11. Model of transmitting antennas with radials.

Similar to previous cases,  $s$ -parameter magnitudes in dB are shown in Table III.

TABLE III  
S-PARAMETER MAGNITUDES BETWEEN ANTENNAS IN RADIAL GROUND MODEL

$ S_{41} $	-6.7407 [dB]
$ S_{42} $	-24.2707 [dB]
$ S_{43} $	-19.2778 [dB]

From these results, it can be seen that antenna coupling is on a similar order with previous cases. The radiation pattern of the array with radials is shown in Fig. 12.

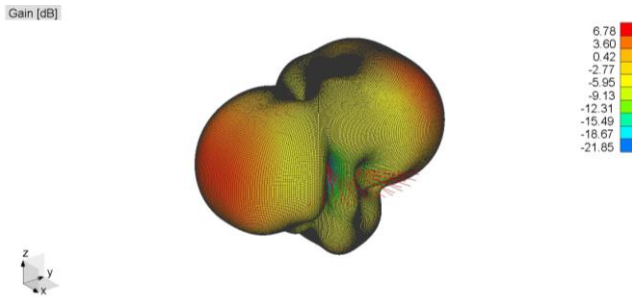


Fig. 12. Radiation pattern for array with radials when all generators are active.

It can be seen that the main lobe is tilted upward. This is typical for a monopole with radials and has nothing to do with coupling [17]. More importantly, the back-lobe is still very pronounced as it was expected (similar to results in Fig. 3), indicating significant antenna mutual coupling, more clearly seen in Fig. 13.

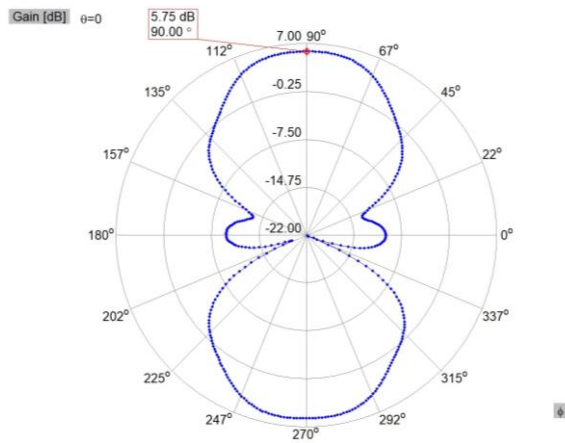


Fig. 13. Radiation pattern in the horizontal cut for array with radials in the horizontal cut when all generators are active.

#### IV. CONCLUSION

In this paper, the effects of different realizations of the ground plane on mutual coupling of antennas on the transmitting array of a deployed HFWR were analyzed. The simulated radiation pattern has differences compared to the theoretical, mainly in the 270° direction. Different realizations of ground planes provided similar *s*-parameters. Considering the restrictions of keeping the antenna array configuration and the maximum allocated area the same, this analysis indicates that a different approach should be taken to affect mutual coupling. This opens the course of future work in the form of obtaining more information about free space coupling of the transmitter array antennas and methods that can affect it.

#### REFERENCES

- [1] United Nations Convention on Law of the Sea.
- [2] D. E. Barrick, M. W. Evans, B. L. Weber, "Ocean Surface Currents Mapped by Radar", *Science*, 1977: Vol. 198, Issue 4313, pp. 138-144 DOI: 10.1126/science.198.4313.138
- [3] J.D. Paduan, L. Washburn, "High-Frequency Radar Observations of Ocean Surface Currents", *Annual Review of Marine Science*, 2013. 5:115-36
- [4] A. Dzvonkovskaya, D. Nikolić, V. Orlić, M. Perić, and N. Tošić. (2019), "Remote Observation of a Small Matesunami in the Bight of Benin

- Using HF Radar Operating in Lower HF Band", *IEEE Access*, 7, 88601-88608.
- [5] L. D. Sevgi and A. M. Ponsford, "An HF Radar Base Integrated Maritime Surveillance System," *Proc. 3rd International Multiconference IMACS / IEEE CSCC'99*, Athens (Greece), July 4-8, 1999, pp.5801-5806.
- [6] D. Nikolić, N. Stojković, P. Petrović, N. Tošić, N. Lekić, Z. Stanković, N. Dončov, "The high frequency surface wave radar solution for vessel tracking beyond the horizon", *Facta universitatis-series: Electronics and Energetics* 33(1),37-59, 4, 2020
- [7] N. Stojkovic, D. Nikolic, P. Petrovic, N. Tosic, I. Gluvacevic, N. Stojiljkovic and N. Lekic: "An Implementation of DBF and CFAR Models in OTHR Signal Processing," *Proc. CSPA 2019*, Penang, Malaysia, pp. 7-11, 8.-9. March 2019.
- [8] D. Nikolić, B. Džolić, N. Tošić, N. Lekić, V. D. Orlić and B. M. Todorović, "HFSW Radar Design: Tactical, Technological and Environmental Challenges", *Proc. of 7th International Scientific Conference on Defensive Technologies (OTEH 2016)*, Belgrade, October 6-7, 350-355.
- [9] R. Petrovic, D. Simic, D. Drajić, Z. Cica, D. Nikolic, and M. Peric, "Designing Laboratory for IoT Communication Infrastructure Environment for Remote Maritime Surveillance in Equatorial Areas Based on the Gulf of Guinea Field Experiences", *Sensors*, vol. 20, no. 5, p. 1349, Feb. 2020.
- [10] N. Stojkovic, D. Nikolic, S. Puzović, "Density Based Clustering Data Association Procedure for Real-Time HFSWRs Tracking at OTH Distances", *IEEE Access* 8,39907-39919, 2020
- [11] S. Zhang, X. Chen and G. F. Pedersen, "Mutual Coupling Suppression with Decoupling Ground for Massive MIMO Antenna Arrays," *IEEE Transactions on Vehicular Technology*, vol. 68, no. 8, pp. 7273-7282.
- [12] S. Marko and E. T. Salonen, "Low Mutual Coupling Between Monopole Antennas by Using Two  $\lambda/2$  Slots," *IEEE Antennas and Wireless Propagation Letters*, vol. 9, pp. 138-141, 2010.
- [13] C. Z. Ning, S. Terence and X. Qing "Cross-Band Mutual Coupling of Monopole Antennas on a Finite-Sized Ground Plane," *IEEE Transaction on Antennas and Propagation*, vol 61. pp. 4372-4375, 2013.
- [14] <https://wipl-d.com/>
- [15] C. A. Balanis, *Antenna Theory: Analysis and Design*, 3<sup>rd</sup> ed. Hoboken, New Jersey, USA: Wiley-Interscience, 2005.
- [16] M. Eric and N. Vukmirovicm, *Uvod u obradu signala sa antenskih nizova - Introduction to antenna array signal processing*, 1<sup>st</sup> ed, Belgrade, RS: Akademska misao, 2019.
- [17] M. Fartookzadeh, S. Armaki, J. Razavi and J. Rashed-Mohassel, (2016), "Optimum Functions for Radial Wires of Monopole Antennas with Arbitrary Elevation Angles", *Radioengineering*, vol. 25., no. 1, pp 53-60.

# Modeling of Matching Load for Slotted Waveguide Antenna

Bojan Milanović, Stefan Filipović, Vladimir Đorđević and Vladimir Petošević

**Abstract**—In order to reduce simulation time, waveguide matching load with rectangular shape is proposed. Matching load is modeled as dielectric layer with losses introduced via imaginary part of the layer's relative permittivity and permeability. In order to estimate quality of the proposed shape, WIPL-s technical support modeled for us pyramidal shape waveguide matching load, which we used as the reference. All models are made in the WIPL-D PRO-16 software. Rectangular shape is proposed in order to reduce boundary area which has led to reduction of number of unknowns. Comparing the execution time it was shown that by modeling the load as rectangular shape dielectric layer, pattern deviation less than 0.5dB is obtained, while simulation time is noticeable reduced.

**Index Terms**—Waveguide matching load; slotted waveguide antenna; travelling wave; WIPL-D.

## I. INTRODUCTION

Slotted waveguide array antenna, firstly was made in Canada, during the Second World War. At the beginning, it was used in military ground and airborne radar systems for target detection and tracking. Afterwards, application of slotted waveguide array antennas spread to many applications such as: remote sensing from aircraft and space vehicles, microwave communication links, weather forecasting, environmental monitoring, climate change studies, etc. Application of the slotted array antenna for automobile collision avoidance systems is also considered [1]. Broad spectrum of application of slotted waveguide antennas is due the simple structure, suitable for mass production with low cost, simple feeding, precise control of aperture distribution and low loss [2, 3, 4]. Slotted waveguide antennas are often used in radar systems because of high gain requirements and mechanical robustness [5].

There are two types of slotted waveguide array antennas: arrays with standing wave, and arrays with traveling wave [5]. Standing wave array antennas are closed with conducting wall, producing reflected wave due which standing wave is formed. Travelling wave antennas are closed with waveguide matching load. No reflections are

produced so no standing wave is formed. Advantage of the travelling wave solution is broader bandwidth.

In order to familiarize with behavior of a radar antenna, model of a slotted waveguide antenna array was built. Idea was to generate and investigate behavior of the antenna pattern for different frequencies, slot angles and to investigate origin of the squint angle. According to the proposal from the WIPL-D technical support, for this research, a matched load with pyramidal absorber is formed. Simulations are started and noticeable length of the simulation time for larger antenna array is noticed. In order to reduce simulation time, alternative solution was needed. According to [6], from the boundary conditions for tangential field components, equivalent electric and magnetic currents placed over the dielectric boundary surface should be uniquely determined. Since the pyramidal absorber has relatively large boundary surface, instead of pyramidal absorber, idea was to reduce surface size by introducing square shaped dielectric layer with corresponding tangent losses. In such manner, shorter simulation time was expected.

## II. SLOTTED WAVEGUIDE ANTENNA

Slotted waveguide antenna is waveguide with a slot on the wider or the narrower wall of the waveguide (Fig. 1). Antenna slot radiates if the slot introduce discontinuity which interrupt the flow of the current along the waveguide. If the current flows around the edges of the slot, the slot will act as dipole antenna [5]. Radiated power from the slot is regulated by tilt angle of the slot. For this simulation and frequency span from 2.9GHz to 3.1GHz, waveguide WR248 (72.136mm x 34.036mm) is used.

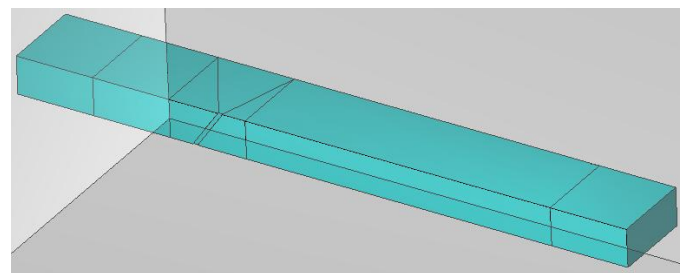


Fig. 1. Slotted antenna with the tilted slot on the narrower side.

Length of the slot should be equal to the half of the free space wavelength. Since this length is larger than the length of the narrower wall, part of the slot is edged (Fig. 2) in to the top and bottom walls [1].

Bojan Milanović is with the Military Academy, University of Defence, Veljka Lukića Kurjaka 33, 11000 Belgrade, Serbia (e-mail: [bojan.milanovic@va.mod.gov.rs](mailto:bojan.milanovic@va.mod.gov.rs)).

Stefan Filipović is with the Military Academy, University of Defence, Veljka Lukića Kurjaka 33, 11000 Belgrade, Serbia (e-mail: [stefi.drenovac1@gmail.com](mailto:stefi.drenovac1@gmail.com)).

Vladimir Đorđević is with the Military Academy, University of Defence, Veljka Lukića Kurjaka 33, 11000 Belgrade, Serbia (e-mail: [vladimir.djordjevic@va.mod.gov.rs](mailto:vladimir.djordjevic@va.mod.gov.rs)).

Vladimir Petošević is with the Military Academy, University of Defence, Veljka Lukića Kurjaka 33, 11000 Belgrade, Serbia (e-mail: [vladimirpetosevic@hotmail.com](mailto:vladimirpetosevic@hotmail.com)).

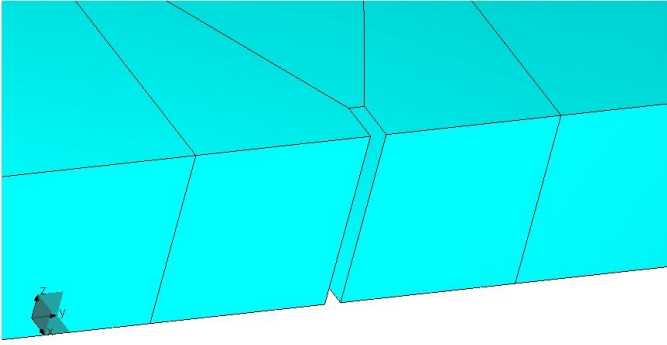


Fig. 2. Waveguide slot edged in to the wither wall.

In order to obtain travelling wave, antenna is closed with matching load (Fig. 3.), proposed from WIPL-D technical support [7].

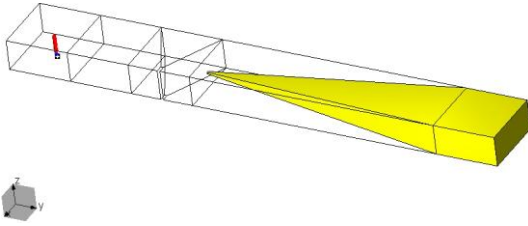


Fig. 3. Position of the pyramidal absorber inside the waveguide.

Pyramidal absorber is two waveguide wavelengths long, with half waveguide wavelength long cubic shape absorber added at the end. Conductivity of the absorber is set to 3 S/m while the real part of the relative permittivity of the absorber is set to 1.1 and imaginary to zero. Simulation of the model with one slot elapsed for 15.62s<sup>1)</sup>. Pattern of the single slot is show in (Fig. 4).

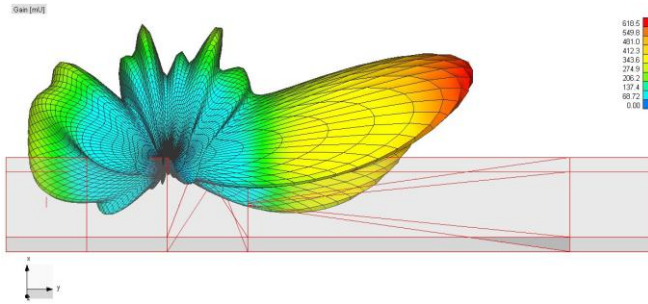


Fig. 4. Pattern of the single slot antenna.

Due to travelling wave condition, pattern is slightly tilted toward waveguide, so in practice, in order to obtained pattern perpendicular to the waveguide, two of this slots are set half wavelength apart, with opposite directions of the tilt.

Model of antenna with two tilted slots is shown in Fig. 5. Simulation time for this array was 34.91s.

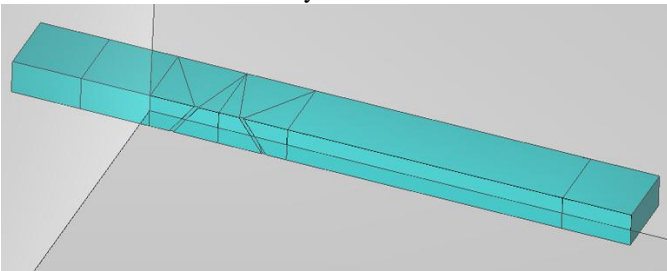


Fig. 5. Two slots antenna array.

<sup>1)</sup> Processor Intel(R) Core(TM) i5-6200U CPU @ 2.30GHz, 2400 Mhz, 2 Core(s), 4 Logical Processor(s)

Antenna pattern of the two slot array is shown in Fig. 6.

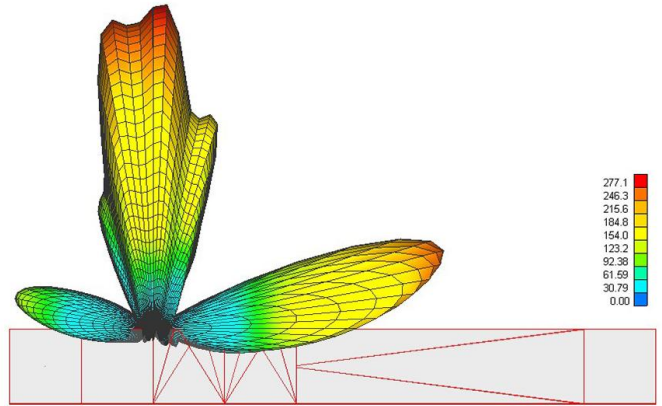


Fig. 6. Antenna pattern of the two slots antenna array.

Simulation for 20 elements antenna array, shown in Fig. 7, elapsed for 117.42s. 2D antenna pattern is calculated for 1441 points in azimuth plane and 1 point in elevation plane.

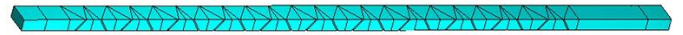


Fig. 7. Twenty elements antenna array.

Antenna pattern of the twenty slots antenna array is shown in Fig. 8.

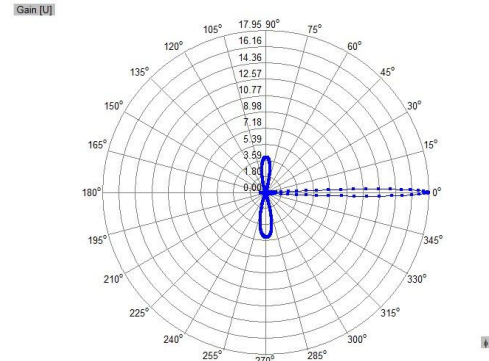


Fig. 8. Twenty elements antenna array pattern.

### III. MATCHED LAYER

In order to match short end to the waveguide, absorber with complex relative permittivity and permeability is used. This layer introduces attenuation of the wave passing through, while keeping matched surface with the air. Wave impedance in the waveguide can be calculated by the equation:

$$Z_{TE10} = \sqrt{\frac{\mu_0 \cdot \mu_r}{\epsilon_0 \cdot \epsilon_r}} \cdot \frac{1}{\sqrt{1 - \left(\frac{\lambda}{\lambda_c \cdot \mu_r \cdot \epsilon_r}\right)^2}} \quad (1)$$

In order to keep no reflection from the air to dielectric boundary, wave impedance of the dielectric should be equal to the wave impedance of the air. In case of the plane wave, that can be easily achieved by setting relative permittivity and permeability to be equal and by introducing imaginary part with negative sign. But, for waveguide, that is not so easy task, since relative permittivity and permeability appears both in front and under the fraction of equation (1). Since in our version of the WIPL, we don't have

optimization tool, relative permittivity and permeability values are obtained by try and error. Idea was to obtain smallest reflection coefficient. In such manner, relative permittivity of  $\epsilon_r = 1 - j \cdot 0.15$  and permeability  $\mu_r = 1 - j \cdot 0.15$  are used.

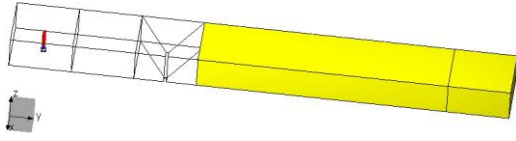


Fig. 9. Rectangular dielectric absorbing layer.

#### IV. RESULTS

Simulations for single slot, two slots and 20 slots antenna arrays with rectangular dielectric absorbing layer are made. For single slot antenna simulation elapsed for 4.78s compared to 15.62s for model with pyramidal absorber.

In the Fig. 10. antenna patterns for model with matching load modeled with pyramidal shape absorber and matching load modeled as rectangular shape absorber are shown overlaid. From Fig. 10. one can see good matching of these two patterns. Gain difference is of the order part of the dB.

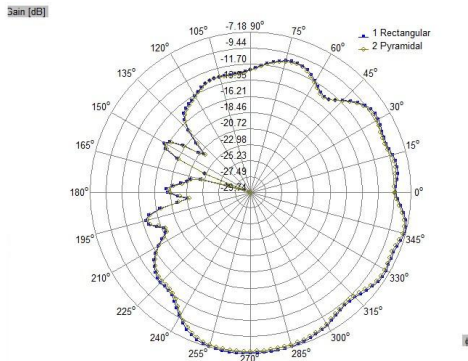


Fig. 10. Single slot antenna pattern comparison.

For two slots antenna array, elapsed time was 6s compared to 34.91s for model with pyramidal shape absorber. In the Fig. 11. antenna patterns for two array antenna model with pyramidal and model with rectangular absorbers are shown overlaid. From Fig. 11. one can see good matching of these two patterns.

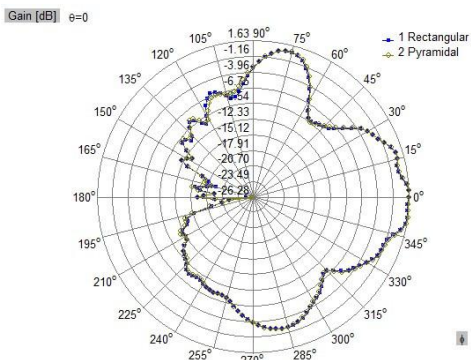


Fig. 11. Two slots antenna pattern comparison.

For 20 slots antenna array, elapsed time was 82.81s compared to 117.42s for model with pyramidal absorber. Same as for previous models, patterns for two different

shapes of the matching loads are shown overlaid in Fig. 12.

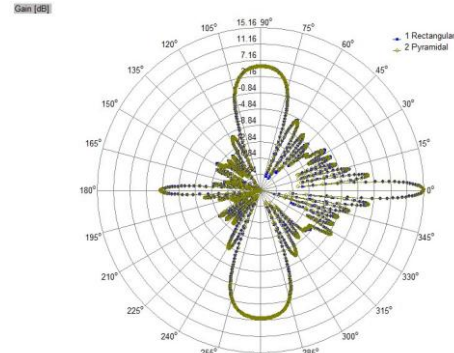


Fig. 12. Twenty slots antenna pattern comparison.

#### V. CONCLUSION

By using different shape of the matching load model, simulation time is significantly reduced. For single slot antenna, simulation time is reduced from 15.62s to 4.78s with no noticeable differences in antenna pattern. For two slots antenna, simulation time is reduced from 34.91s to 6s while, for twenty slots antenna array simulation time is reduced from 117.42s to 82.84s. This analysis shows that by reducing total surface area of the boundary between domains, simulation time can be reduced with no significant loss in pattern calculation. Simulations are made for one frequency and single tilt angle of the slot. By taking simulations for many frequencies and many slot tilt angles, this elapsed time reduction become more significant.

#### ACKNOWLEDGMENT

This paper is part of University of Defence research project VA/TT/1/19-21.

#### REFERENCES

- [1] Josefsson L, Rengarajan S. Slotted waveguide array antennas: theory, analysis and design. SciTech Publishing Inc.,; 2018.
- [2] Park S, Tsunemitsu Y, Hirokawa J, Ando M. Center feed single layer slotted waveguide array. IEEE transactions on antennas and propagation. 2006 May 8;54(5):1474-80.
- [3] Wang W, Zhong SS, Zhang YM, Liang XL. A broadband slotted ridge waveguide antenna array. IEEE transactions on antennas and propagation. 2006 Aug 7;54(8):2416-20.
- [4] R. C. Hansen, *Phased Array Antennas*. New York: Wiley, 1998.
- [5] Enju RK, Perotoni MB. Slotted waveguide antenna design using 3D EM simulation. Microwave Journal. 2013 Jul 12;56(7):72.
- [6] Kolundžija BM. WIPL-D Microwave: Circuit and 3D EM Simulation for RF & Microwave Applications: Software and User's Manual. WIPL-D. Artech House. Inc: Norwood, MA. 2005.
- [7] <https://wipl-d.com/support/>, last accessed 30.08.2020.

# Phased Arrays of Cavity-backed Antennas for 5G Smartphones with Metallic Casing

Miodrag Tasić, *Member IEEE* and Dragan Nikolić

**Abstract**—Cellular handset antennas for future 5G applications need to provide beam steering, so the antenna focus is on the phased arrays. For the metallic casing handsets, a cavity-backed antenna is a natural candidate for an element of the phased array. Cavity can be cut in the handset wall and filled with the dielectric, thus potential waterproofing can be maintained. Radiation is through the cavity, hence the metallic casing is not an obstacle. In this paper we use electromagnetic models to investigate the problems and limitations of a phased array with cavity-backed antennas.

**Index term**—5G; phased arrays; cavity-backed antenna; electromagnetic modeling.

## I. INTRODUCTION

IN order to provide higher bandwidths for cellular services, 5G technology will (also) use frequency bands near (28 GHz) or in (38 GHz, 60 GHz) millimeter-wave (mmWave) spectrum [1]. Since propagation losses in mmWave spectrum are higher than in the spectrum under 3 GHz (used so far, for 4G and older technologies), utilization of highly directive antennas with beam steering is implied. Frequency range around 28 GHz seems to be especially interesting, since minimum of propagation loss occurs in that range [2].

Design principles for 5G antennas are yet to be established [3]. However, for cellular handsets with metallic casing, antennas in the form of slots in the casing are one obvious solution [4], [5]. Namely, the metal casing would block the signal if the antenna was inside, hence typical phased array of patches cannot be used. In that sense, a cavity-backed antenna [6] is a good choice for the element of the phased array. At the time being, smartphones with 5G label have glass back panels and, furthermore, can be delivered without mmWave 5G antenna modules (though they have slots for this purpose). Anyway, phased arrays with cavity-backed elements can be naturally employed if a handset has a metal frame (if not full metallic casing).

In this work, we implement a phased array of cavity-backed antennas as in [4]. We adopt the same cavity size, aimed to work in the frequency range around 28 GHz, whereas we optimized dimensions of feeding microstrip lines. Two models of a cellular handset with phased arrays are discussed—one with a metallic frame, but without a cover,

and the other with a metallic cover, i.e., with full metal casing. Interiors of models are empty. In reality, the casings are completely filled: the largest part is occupied by the battery (and, maybe, the coil for wireless charging), then by the camera and motherboards. More comprehensive study is necessary to consider effects of these components, which is beyond the scope of this work.

The geometrical and electromagnetic models of the phased array antenna are presented in Section II, numerical results are presented in Section III, whereas conclusions are given in Section IV.

## II. ANTENNA MODEL

Outlines of the model are shown in Fig. 1. A cavity-backed antenna comprises a cavity excited by a stepped pin fed by a microstrip line. There are two eight-element phased arrays along two edges. Each cavity-backed antenna is enumerated. A 3D view, with the dimensions, is shown in the figure inset. The model is situated in the Cartesian coordinate system, also shown in the figure.

Cavity is shown in Fig. 2. It is excited by a metal stepped pin. The wider part of the pin is connected to the wall of the cavity, whereas the narrower part is soldered to the microstrip line. In the original design, the metal pin is nailed from outside of the metallic frame. In electromagnetic sense, these two models are equivalent. The pin is attached to the feeding microstrip line, as shown in Fig. 3. The point voltage generator is connected to the other side of the microstrip line, between the line and the ground plane.

Dimensions, in mm, are shown in Fig. 4 ( $xy$ -plane) and in Fig. 5 ( $xz$ -plane). Dimensions of the cavity and the stepped pin and the parameters of the dielectrics are the same as in [4]. The relative permittivity of the dielectric in the cavities is 3, whereas the relative permittivity and the thickness of the microstrip line substrate are 2.2, and 0.254 mm. The boards of the microstrip lines for different antennas are separated to achieve better isolation between the ports. The dimensions of the microstrip line and of all gaps around it are optimized to achieve good balance between port's reflection coefficients and the coupling between the ports. Note that the structure is sensitive in this regard, so one can expect a notable discrepancy between simulated and measured  $S$ -parameters.

Solid 3D model of the handset frame with the cavity-backed antennas is shown in Fig. 6. Since handset covers commonly are not metallic (or, at least, one of them is not), such model can be considered as an approximate model for the handset with low permittivity dielectric covers.

Miodrag Tasić – Elektrotehnički fakultet, Univerzitet u Beogradu, Bulevar Kralja Aleksandra 73, 11020 Beograd, Srbija (e-mail: tasic@etf.rs).

Dragan Nikolić – Elektrotehnički fakultet, Univerzitet u Beogradu, Bulevar Kralja Aleksandra 73, 11020 Beograd, Srbija (e-mail: nikolicdragansiki@gmail.com).

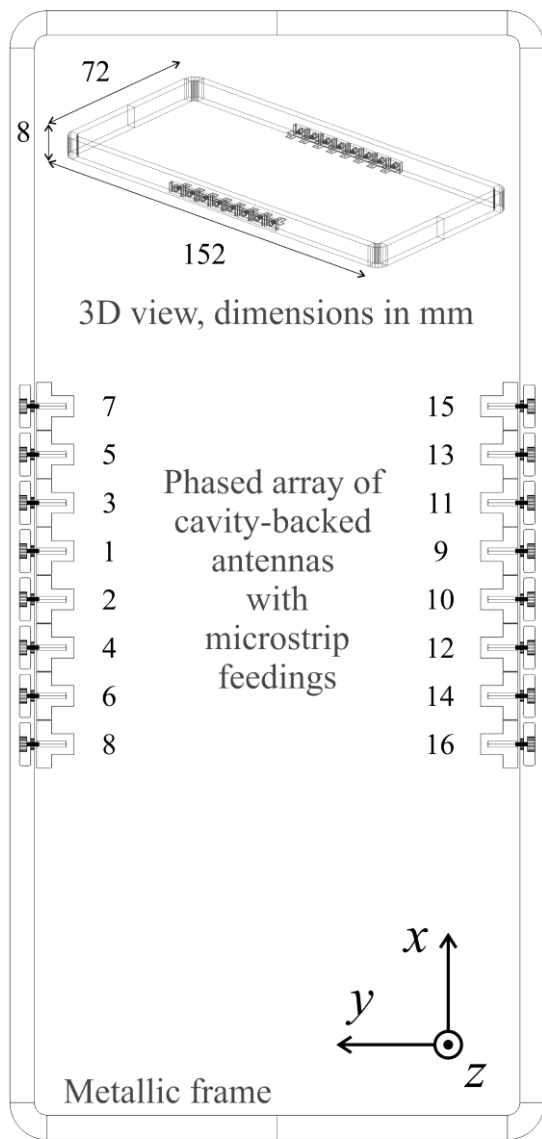


Fig. 1. Cellular handset metallic frame with two eight-element phased arrays with cavity-backed elements.

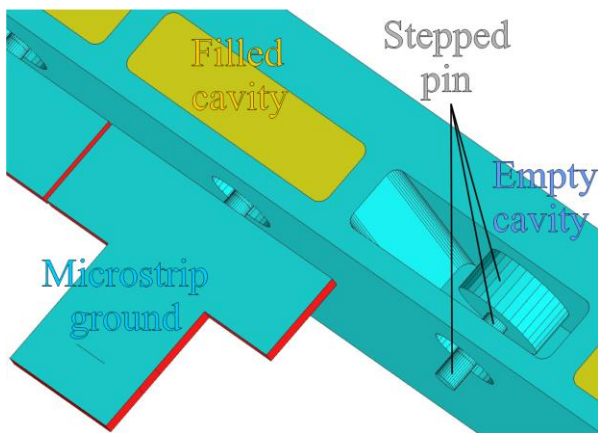


Fig. 2. Cavity filled with dielectric material and excited by a stepped pin. Empty cavity is shown as an illustration of the interior.

The handset with the metallic covers is shown in the Fig. 6 inset. The covers are model as infinitely thin metallic plates. The losses in the metal and dielectrics are neglected.

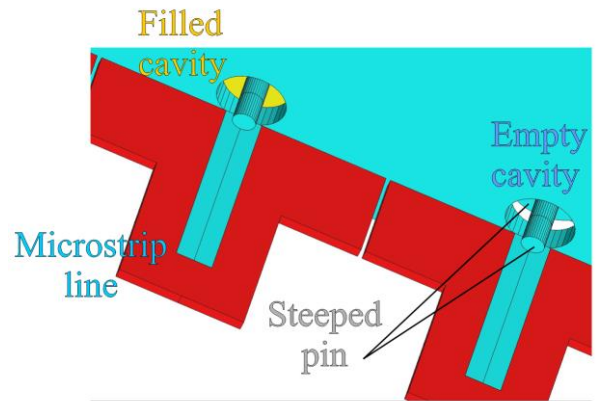


Fig. 3. Stepped pin fed by a microstrip line.

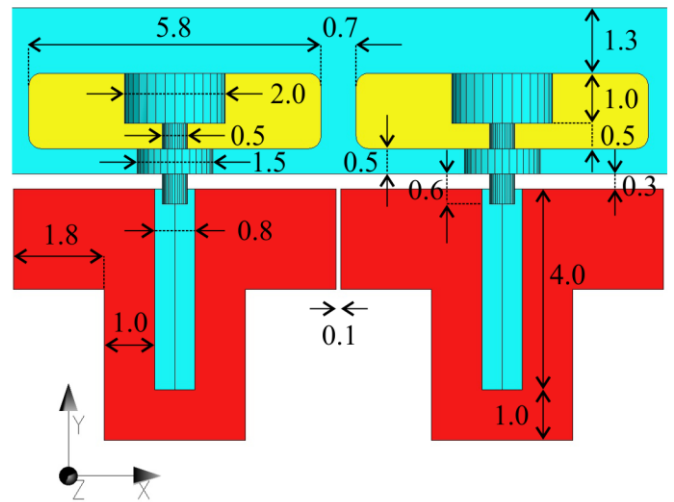


Fig. 4. Dimensions of the structure in mm,  $xy$ -plane.

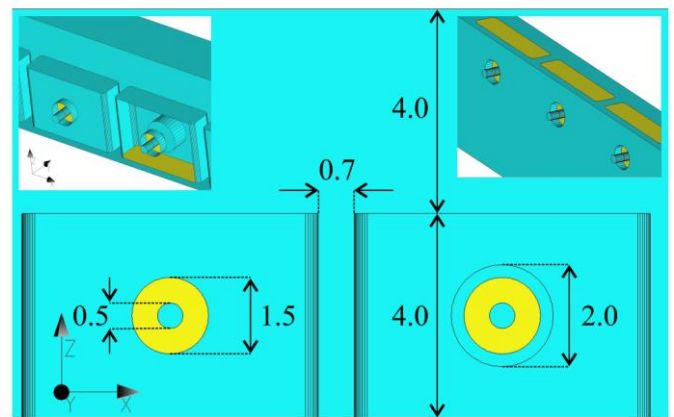


Fig. 5. Dimensions of the structure in mm,  $xz$ -plane. 3D views are shown in the figure insets.

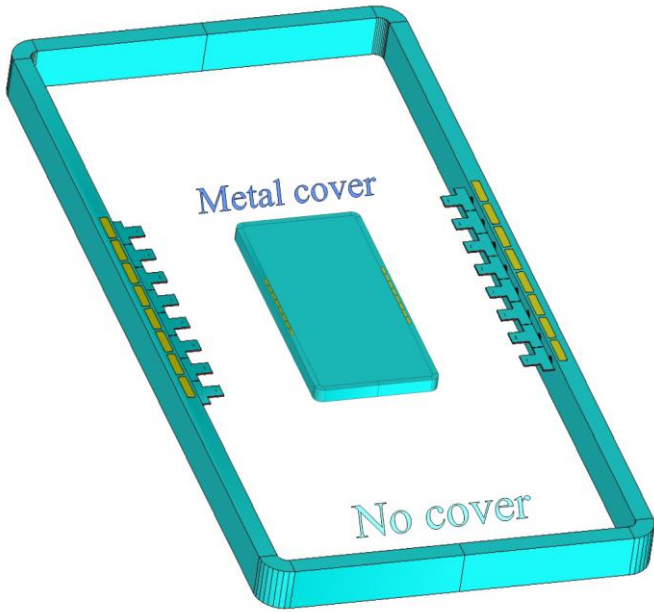


Fig. 6. Solid model of the handset frame, without the cover, with the cavities (in yellow). Model with the metallic cover is shown in the figure inset.

### III. NUMERICAL RESULTS

All simulations are performed using the software for electromagnetic modeling WIPL-D [7]. S-parameters are calculated in 21 linearly spaced frequencies from 27 GHz to 29 GHz. Radiation is calculated at 28 GHz. From a few numerical simulations, it is concluded that losses in the metal and the dielectric are not significant factor, so the presented results are for the lossless materials. The ports are at the voltage generators positions. The feeder used for microstrip lines has low reflection coefficient, but de-embedding of S-parameters in the plane of interest may be necessary for ultimate precision. Simulations are performed using two models from Fig. 6, referenced as Metal cover and No cover.

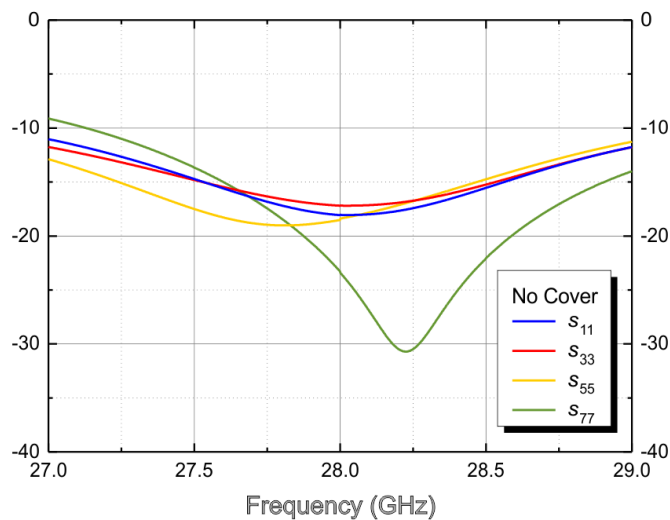


Fig. 7. Magnitudes of the reflection coefficients (i.e., magnitudes of  $S_{jj}$  parameters, in dB) at the ports 1, 3, 5, and 7, for the No cover model.

Magnitudes of the reflection coefficients (i.e., magnitudes of  $S_{jj}$  parameters, in dB) at the ports 1, 3, 5, and 7 (as numerated in Fig. 1), for No cover model, is shown in Fig. 7. Since the model is symmetric along two axes ( $x$  and  $y$ ), every other port has a reflection coefficient equal to one of those in Fig. 7. Ports 1 and 3 have similar reflection, whereas reflection curves for ports 5 and 7 are shifted in frequency (about 250 MHz), down, i.e., up. Furthermore, reflection at port 1 reaches significantly lower magnitudes. The curves are smooth, and 10 dB bandwidth is excellent ( $> 2$  GHz).

Magnitudes of the couplings (i.e., magnitudes of  $S_{jk}$  parameters, in dB) between some of the ports, for No cover model, is shown in Fig. 8. As expected, the coupling is stronger for physically closer ports. The most critical are pairs of adjacent ports at the end of the phased array (i.e.,  $S_{75}$  has the highest magnitude of all), and generally ports at the end of the array has stronger couplings (e.g.,  $S_{73}$  is higher than  $S_{51}$  and  $S_{41}$ ). The curves are smooth, as in Fig. 7.

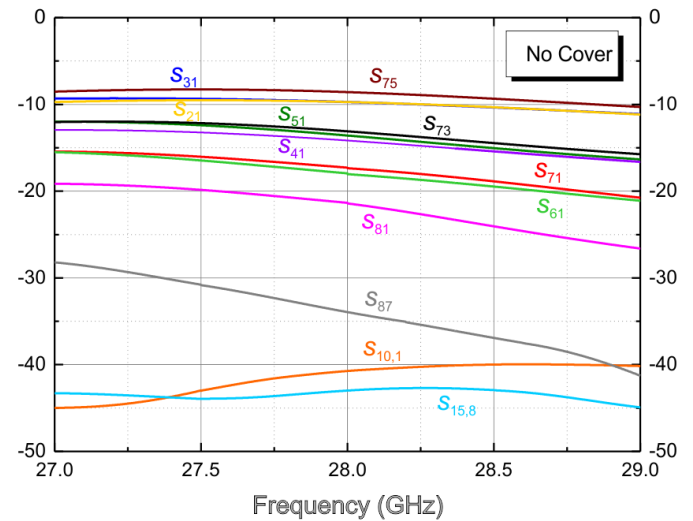


Fig. 8. Magnitudes of the couplings (i.e., magnitudes of  $S_{jk}$  parameters, in dB) between some of the ports, for the No cover model.

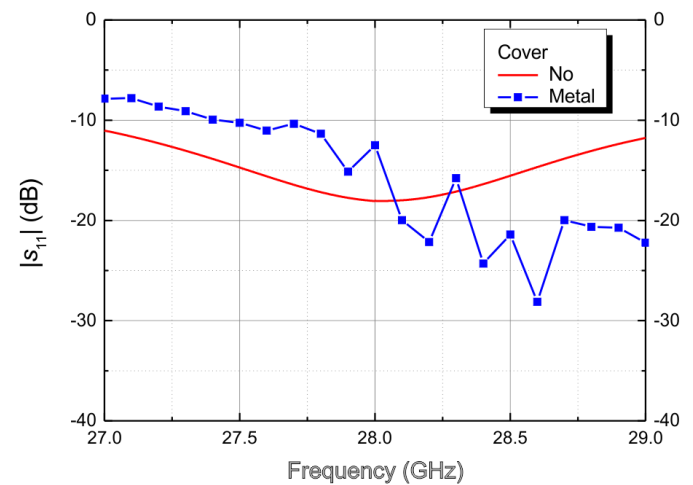


Fig. 9. Magnitudes of the reflection coefficients at the port 1, comparison between No cover and Metal cover models.

Putting metal covers on the frame makes significant difference. The structure becomes highly resonant, which can be seen in comparison with the No cover models. Magnitudes of the reflection coefficients for No cover and Metal cover models are compared in Fig. 9 (at port 1) and Fig. 10 (at port 7). Magnitudes of the couplings between ports 1 and 2, that is, ports 15 and 8 are compared in Fig. 11. Curves for the Metal cover model show high oscillations, which would be even higher if the curves were calculated in more frequency points. Generally, the Metal cover antenna will work, but there is a chance of malfunctioning at some frequencies.

Radiation pattern (Realized gain, in dB) when only generator 1, or 3, is turn on is shown in Fig. 12 ( $xz$ -plane), and Fig. 13 ( $yz$ -plane). Because of the symmetry, we can look only antennas 1, 3, 5, and 7. They have somewhat different radiation patterns, as illustrated for antennas 1 and 3. Maximal realized gain for Metal cover fluctuates more, because of the fluctuations in the reflection coefficient.

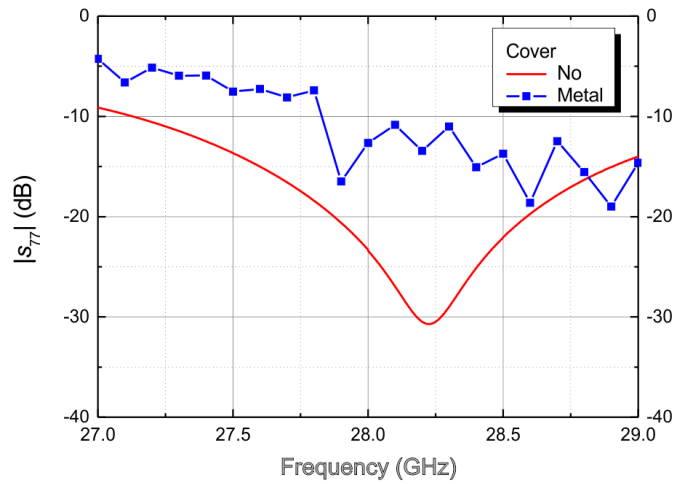


Fig. 10. Magnitudes of the reflection coefficients at the port 7, comparison between No cover and Metal cover models.

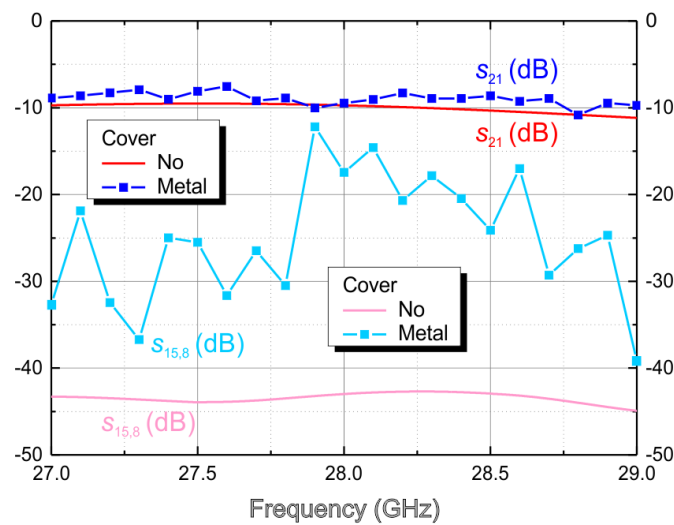


Fig. 11. Magnitudes of the couplings between some ports, comparison between No cover and Metal cover models.

Realized gain can reach as high as 9 dB for the Metal cover model, in the  $xz$ -plane. Maximal realized gain in the  $yz$ -plane is about 6 dB.

Finally, we should check the beam steering capability of the phased array. By using elementary mathematical relations for the antenna arrays (wavelength at 28 GHz, the distance between array elements, and the number of elements), we can conclude that only by phase shift between currents of the elements, we can form the beam with the angle with respect to the axes of the array ( $x$ -axes) between 60 degrees and 90 degrees (90 degrees corresponds to zero phase shift). For this purpose, we used the model with only one eight-element phased array (antennas 1 to 8).

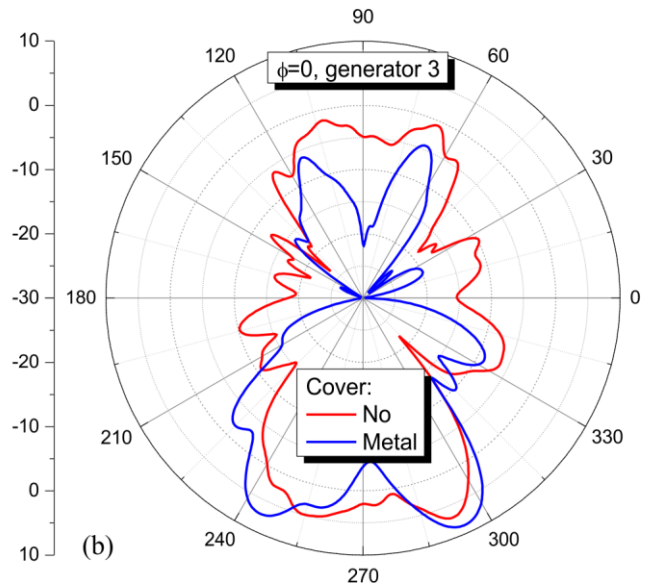
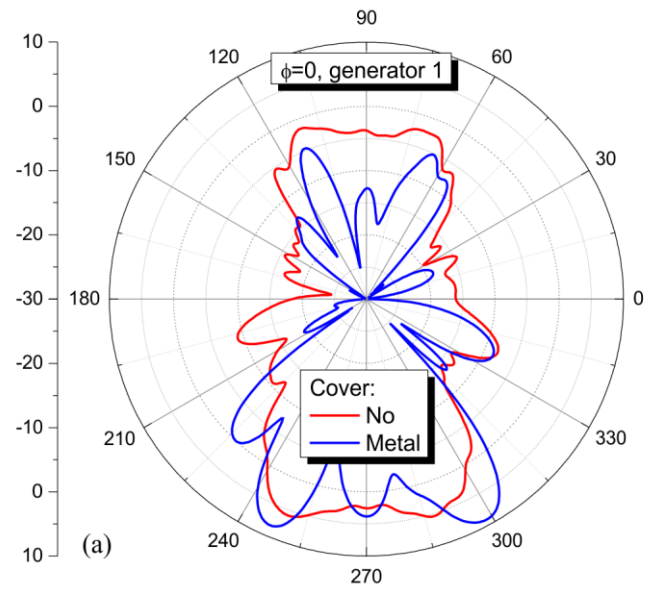


Fig. 12. Radiation pattern (Realized gain, in dB) in the  $xz$ -plane ( $\phi = 0$  degrees); comparison between No cover and Metal cover models, when only generator: (a) 1 and (b) 3 is turned on.

Second phased array (antennas 9 to 16) was removed from the model. Technically, by removing the second array, we obtain a different model. However, numerical results show that, for the No cover model, results for radiation patterns of these two models are very similar.

Hence, using the No cover model with the second array removed, we applied only uniform phase shifts to antenna generators, in order to obtain angles (with respect to the  $x$ -axes) of 90 degrees (no phase shift), 75 degrees, 60 degrees, and 45 degrees. The results for 3D radiation patterns (Realized gain, in dB) are shown in Figs. 14 to 17 (the frame of the handset, shown in the figures, is represented with a mesh of quadrilateral patches).

We can see that such setup works correctly for 90 degrees (Fig. 14, maximal realized gain 15.33 dB), 75 degrees (Fig. 15, maximal realized gain 15.89 dB), and 60 degrees (Fig. 16, maximal realized gain 15.47 dB). However, as expected, directivity of the radiation pattern significantly decreases for 45 degrees (which is outside the expected range from 60 degrees to 90 degrees). At this angle, the phased array factor “catches” maximums in two directions (45 degrees is one of them), so the resulting radiation pattern is less directive, and the maximal realized gain is only 9.08 dB (Fig. 17). Technically, for larger scanning range, the smaller distance between array elements (cavities) is needed.

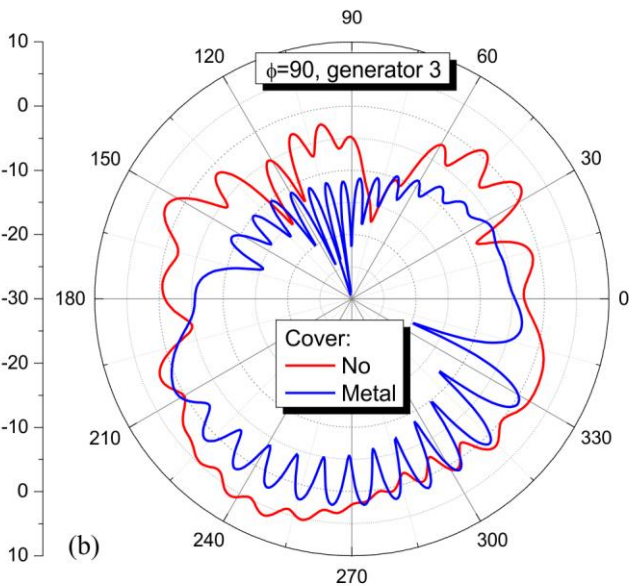
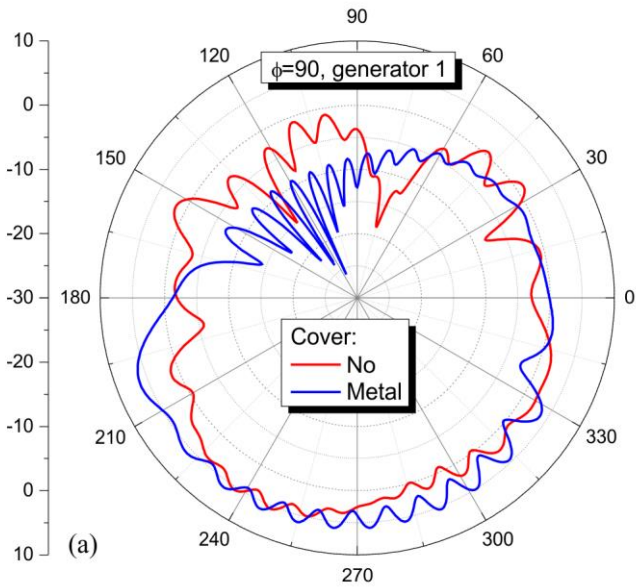


Fig. 13. Radiation pattern (Realized gain, in dB) in the  $yz$ -plane ( $\phi = 90$  degrees); comparison between No cover and Metal cover models, when only generator: (a) 1 and (b) 3 is turned on.

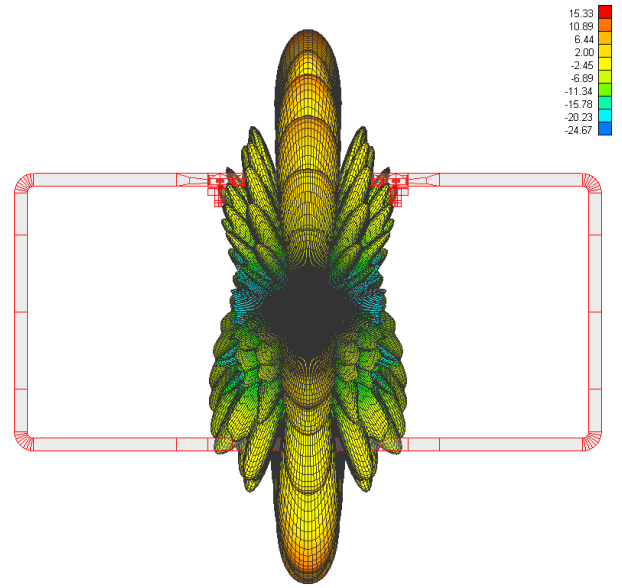


Fig. 14. 3D Radiation pattern (Realized gain, in dB) of the No cover model; phase shift adjusted for 90 degrees angle from the horizontal axes.

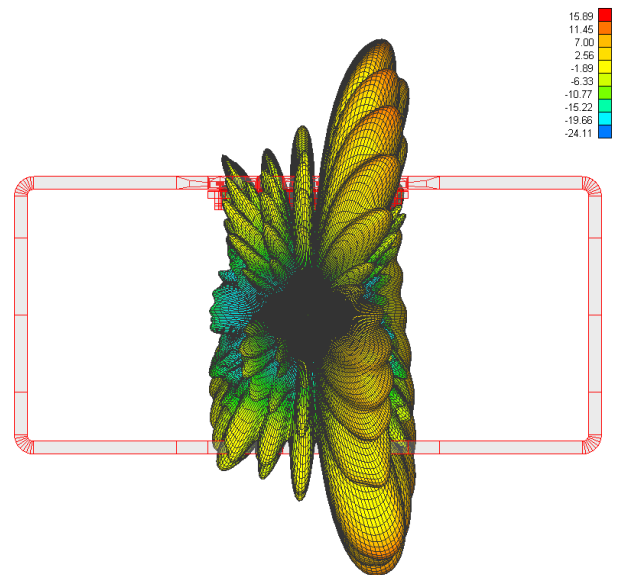


Fig. 15. 3D Radiation pattern (Realized gain, in dB) of the No cover model; phase shift adjusted for 75 degrees angle from the horizontal axes.

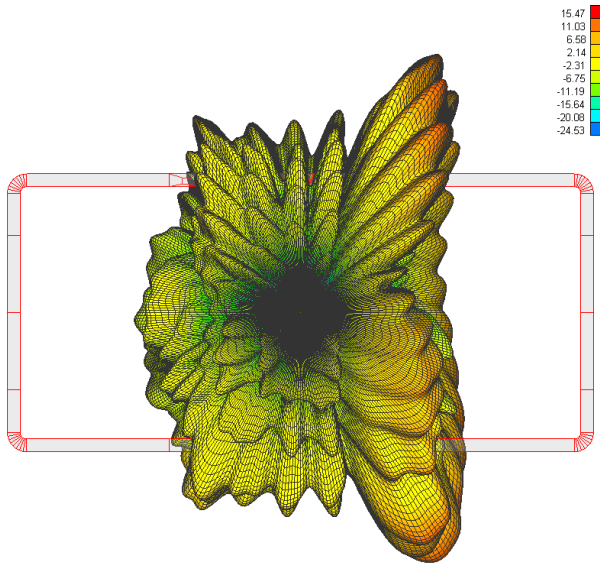


Fig. 16. 3D Radiation pattern (Realized gain, in dB) of the No cover model; phase shift adjusted for 60 degrees angle from the horizontal axes.

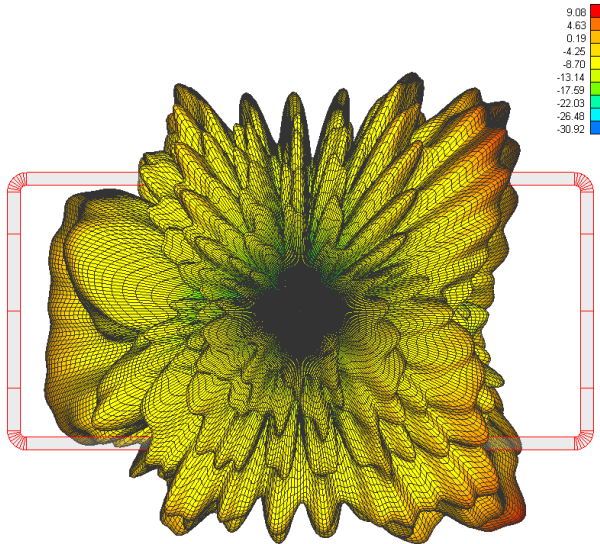


Fig. 17. 3D Radiation pattern (Realized gain, in dB) of No cover model; phase shift adjusted for 45 degrees angle from the horizontal axes.

#### IV. CONCLUSIONS

Numerical simulations show that phased arrays of cavity-backed antennas, in the frequency range around 28 GHz, can be successfully integrated into the metal frame of a cellular handset. If the frame is not covered with metallic plates, the phased array works correctly, within expectations, with large impedance bandwidth and good radiation pattern. However, the key advantage of the cavity-backed antennas is their potential usage in the handsets with fully metallic casing (of course, with slots for camera lenses). By covering the handset frame with the metal plates, S-parameters degrade, with moderate to high oscillations in the frequency range of interest (27 GHz to 29 GHz). These oscillations can result in reduced realized gain and high coupling between antennas, which could cause malfunctioning of the antenna system. Investigated solution has rather small scanning range (for both frame and full metal model), which can be improved by using smaller distance between cavity-backed antennas (and, consequently, smaller cavities). Position of the phased array should be reconsidered.

#### REFERENCES

- [1] A. I. Sulyman, A. T. Nassar, M. K. Samimi, G. R. Maccartney, T. S. Rappaport and A. Alsanie, "Radio propagation path loss models for 5G cellular networks in the 28 GHz and 38 GHz millimeter-wave bands," in *IEEE Communications Magazine*, vol. 52, no. 9, pp. 78-86, September 2014.
- [2] T. S. Rappaport et al., "Millimeter Wave Mobile Communications for 5G Cellular: It Will Work!," in *IEEE Access*, vol. 1, pp. 335-349, 2013.
- [3] W. Hong, K. Baek and S. Ko, "Millimeter-Wave 5G Antennas for Smartphones: Overview and Experimental Demonstration," in *IEEE Transactions on Antennas and Propagation*, vol. 65, no. 12, pp. 6250-6261, Dec. 2017.
- [4] B. Yu, K. Yang, C. Sim and G. Yang, "A Novel 28 GHz Beam Steering Array for 5G Mobile Device With Metallic Casing Application," in *IEEE Transactions on Antennas and Propagation*, vol. 66, no. 1, pp. 462-466, Jan. 2018.
- [5] J. Bang and J. Choi, "A SAR Reduced mm-Wave Beam-Steerable Array Antenna With Dual-Mode Operation for Fully Metal-Covered 5G Cellular Handsets," in *IEEE Antennas and Wireless Propagation Letters*, vol. 17, no. 6, pp. 1118-1122, June 2018.
- [6] S. Long, "Experimental study of the impedance of cavity-backed slot antennas," in *IEEE Transactions on Antennas and Propagation*, vol. 23, no. 1, pp. 1-7, January 1975.
- [7] WIPL-D Pro v17—3D EM Solver, Belgrade, Serbia, 2019, [online] Available: <http://www.wipl-d.com>

# Simulation of Wideband Bandpass Filters with Arbitrary Relative Bandwidth

Dušan Nešić, *Member, IEEE*, Branko Kolundžija, *IEEE Fellow* and Tomislav Milošević

**Abstract** - Algorithm for the realization of the wide relative bandwidth (*RBW*) bandpass filters is introduced. Algorithm is based on periodic ideal waveguide cells each with short-ended stub. Design curve of the ratio between characteristic impedance of the short-ended stub and the characteristic impedances of the main lines is given for the broad range of values of *RBW*.

**Index Terms** - Microwaves, Wide bandpass filter, Specified relative bandwidth, microstrip.

## I. INTRODUCTION

WIDE bandpass filters are important part of microwave systems [1-4]. Many of them are for unlicensed ultrawideband communications spectrum from 3.1 GHz to 10.6 GHz with relative bandwidth (*RBW*) of 106 % [1,4]. Another are customized for wider or something narrower *RBWs*. All of them are assumed to suppress DC and lower frequencies. It can be done using coupling and short-ended stubs [1-4] or only short-ended stubs [5-9]. Majority of them are done in microstrip technology, the most use planar technology in microwave systems. Some of them are also using defected ground structure (DGS), coupling or multilayers [1,4]. General problem is that there is no specific algorithm procedure for the broad range of values of *RBW*.

This paper introduces algorithm for the broad range of values of *RBW* up to 1.6 using only short-ended stubs. The structure is without coupling and without defected ground structure (DGS). Fabrication technology is the single layer microstrip. The procedure is tested on the fabricated filter for *RBW* 150 %.

## II. ALGORITHM

Considered general structure of the ideal lossless unit cell is shown in Fig. 1. It is something similar to the cell for low-pass filter with open-ended shunt network in [10]. The shunt network in this paper is short-ended. All cell networks are described, as in [10], in the form of ABCD matrix. The cell consists of three networks: two networks (N1 and N2) are cascaded and one network is shunted and short-ended (N3). Network N2 is the same as N1 except that the roles of its ports are reversed, so that  $A_t = D$ ,  $B_t = B$ ,  $C_t = C$  and  $D_t = A$ .

Dušan Nešić is with Centre of Microelectronic Technologies, Institute of Chemistry, Technology and Metallurgy, University of Belgrade, Njegoševa 12, 11000 Belgrade, Serbia (mail: [nesicad@nanosys.ihtm.bg.ac.rs](mailto:nesicad@nanosys.ihtm.bg.ac.rs)).

Branko Kolundžija is with the School of Electrical Engineering, University of Belgrade, 73 Bulevar kralja Aleksandra, 11020 Belgrade, Serbia (e-mail: [kol@etf.rs](mailto:kol@etf.rs)).

Tomislav Milošević is with WIPL-D d.o.o., Gandijeva 7, 11073 Belgrade, Serbia, (E-mail: [tomislav.milosevic@wipl-d.com](mailto:tomislav.milosevic@wipl-d.com)).

Effectively, two identical networks of ABCD-parameters  $A$ ,  $B$ ,  $C$ , and  $D$  is cascaded back to back at port ⑤ with the shunt network of ABCD-parameters  $A_s$ ,  $B_s$ ,  $C_s$ , and  $D_s$ , whose other port is short-ended. In fact it is one T-junction.

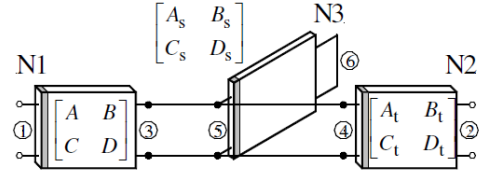


Fig. 1. Scheme of a filter cell with ABCD matrix.

Presentation of the developed matrix of the cell in Fig. 1. Matrix of N1 ( $ABCD$ ) and N2 ( $DBCA$ ) are presented in (1) and matrix of shunt short-ended network N3 ( $A_s B_s C_s D_s$ ) is developed in (2).

$$\begin{bmatrix} A & B \\ C & D \end{bmatrix} = \begin{bmatrix} \cos \theta & jZ \sin \theta \\ \frac{j}{Z} \sin \theta & \cos \theta \end{bmatrix} \text{ and } \begin{bmatrix} D & B \\ C & A \end{bmatrix} \quad (1)$$

$$\begin{bmatrix} A_s & B_s \\ C_s & D_s \end{bmatrix} = \begin{bmatrix} \cos \theta_s & jZ_s \sin \theta_s \\ \frac{j}{Z_s} \sin \theta_s & \cos \theta_s \end{bmatrix} \quad (2)$$

The shunt short-ended network N3 acts as a shunt admittance  $Y = D_s/B_s$  at port ⑤ (3).

$$\begin{bmatrix} 1 & 0 \\ Y & 1 \end{bmatrix} = \begin{bmatrix} 1 & 0 \\ \frac{D_s}{B_s} & 1 \end{bmatrix} \quad (3)$$

Matrix of the completed cell ( $A_c B_c C_c D_c$ ) is presented in (4)

$$\begin{bmatrix} A_c & B_c \\ C_c & D_c \end{bmatrix} = \begin{bmatrix} A & B \\ C & D \end{bmatrix} \cdot \begin{bmatrix} 1 & 0 \\ \frac{D_s}{B_s} & 1 \end{bmatrix} \cdot \begin{bmatrix} D & B \\ C & A \end{bmatrix} = \begin{bmatrix} AD + BC + \frac{D_s}{B_s} BD & 2AB + \frac{D_s}{B_s} B^2 \\ 2CD + \frac{D_s}{B_s} D^2 & AD + BC + \frac{D_s}{B_s} BD \end{bmatrix} \quad (4)$$

In an infinite cascade of identical unit cells the wave propagates along the structure only if  $|(A_c + D_c)/2| \leq 1$  [11], which implies existence of pass bands of the structure. After arranging matrix with reciprocity  $AD = BC + 1$  (5).

$$-1 \leq AD + BC + \frac{D_s BD}{B_s} \leq 1 \quad 0 \leq 2AD + \frac{D_s BD}{B_s} \leq 2 \quad (5)$$

Take attention on  $B/B_s$ . After incorporating values for ABCD parameters from (1) and (2), equation (5) becomes

$$0 \leq 2\cos(\theta)^2 + \cos(\theta_s)\cos(\theta) \frac{Z \sin(\theta)}{Z_s \sin(\theta_s)} \leq 2 \quad (6)$$

To eliminate changing the sign of  $\sin(\theta_s)$  and make easier for realization it is chosen to be  $\theta = \theta_s$ .

$$-1 \leq -1 + 2\cos(\theta)^2 + \cos(\theta)^2 \frac{Z}{Z_s} \leq 1 \quad (7)$$

Diagram of (7) in Fig. 3 is done for an arbitrary ratio  $Z/Z_s$ . Relation (7) has a period  $\pi$  and is presented in the phase range from 0 to  $\pi$ . The result of the relation (7) is in the range between -1 and +1 and corresponds to the bandpass region.

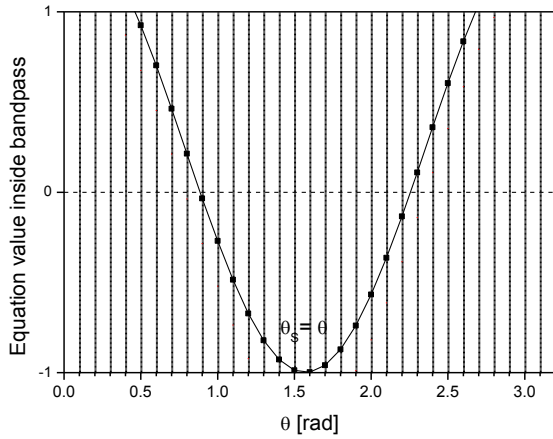


Fig. 3. Value of  $(A_c + D_c) / 2$  inside bandpass vs.  $\theta$ .

As can be seen in Fig. 3, center of the bandpass region logically corresponds to  $\theta_s = \pi/2$ . Boundaries of the bandpass are signed with  $\theta_{c1}$  for the lower frequency and  $\theta_{c2}$  for the higher frequency. According to the mentioned one can calculate useful bandpass filter characteristics. In the case  $\theta_s = \theta$  relation between boundaries is  $\theta_{c2} = \pi - \theta_{c1}$  and  $\theta_{c1}$  will be replace in equations simply with  $\theta_c$ . Relative bandwidth ( $RBW$ ) of the bandpass is

$$RBW = \frac{\theta_{c2} - \theta_{c1}}{\frac{1}{2}(\theta_{c1} + \theta_{c2})} = 2 - \frac{4}{\pi} \theta_{c1} = 2 - \frac{4}{\pi} \theta_c \quad (8)$$

$$\theta_c = \frac{2 - RBW}{4} \pi \quad (9)$$

For  $RBW = 2$  value of  $\theta_c$  becomes 0 and  $Z_s / Z$  is approaching infinity. For other values of  $RBW$  the boundary condition for (7) becomes

$$-1 + 2\cos(\theta_c)^2 + \cos(\theta_c)^2 \frac{Z}{Z_s} = 1 \quad (10)$$

$$\cos(\theta_c) = \sqrt{\frac{1}{1 + \frac{Z}{2Z_s}}}; \quad \cos(\pi - \theta_c) = -\sqrt{\frac{1}{1 + \frac{Z}{2Z_s}}} \quad (11)$$

$$\frac{Z}{Z_s} = 2 \operatorname{tg}^2(\theta_c) \quad (12)$$

For the given  $RBW$  one can calculate boundary  $\theta_c$  from (9) and next calculate  $Z/Z_s$  from (12).

As can be seen from (9) maximum  $RBW$  is 2 and according to Fig.4 very high  $RBW$  needs huge ratio between  $Z_s$  and  $Z$  and it is not realizable. The same is valid for the narrow  $RBW$ . Realizable  $RBW$  in microstrip technology is good for a wideband bandpass filter below  $RBW = 1.6$ . Ratio  $Z_s / Z > 1$  corresponds to relatively narrow stub microstrip line and is easier for realization of T-junction close to ideal.

### III. APPLICATION

For the filter formed by cascade of identical unit cells it is important to match nominal impedance of ports (commonly  $Z_0 = 50 \Omega$ ) as much as possible. It was done matching Bloch impedance to the nominal impedance  $Z_0$ .

$$Z_0 = Z_B = \sqrt{\frac{B_c}{C_c}} \quad (13)$$

And gives

$$Z_B = \frac{Z}{\cos \theta_c \sqrt{1 - \left(\frac{\cot \theta}{\cot \theta_c}\right)^2}} \quad (14)$$

As can be seen Bloch impedance is equal to  $Z / \cos(\theta_c)$  for the center of the band-pass filter ( $\theta = \pi/2$ ). It means that  $Z$  in the simulation process has the start value of  $Z = Z_0 \cos(\theta_c)$  and need to be optimized for the whole band-pass. Dependence of  $Z$  and  $Z_s$  vs.  $RBW$  for Bloch impedance of  $50 \Omega$  is presented in Fig. 4.

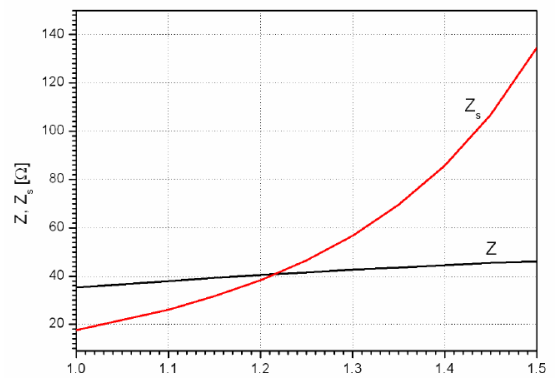


Fig. 4. Dependence of  $Z$  and  $Z_s$  vs.  $RBW$  Bloch impedance of  $50 \Omega$ .

Using previously developed equations 4-cells filters are simulated for  $RBW = 1.5$  (150%), 1.33 (133%) and 1.0 (100%) around central frequency of 3 GHz. Ideal model in WIPL-D Microwave Pro v5.1 [12] is presented in Fig. 5. for 4 identical cells with correspondence between  $\pi/2$  and  $(\lambda/4)$ .

$$\theta_c = \frac{2-RBW}{4}\pi \quad \frac{Z}{Z_s} = 2tg^2(\theta_c) \quad Z=Z_0 \cos(\theta_c) \quad (15a,b,c)$$

Simulated results for 4 identical cells are presented in Fig. 6a and 6b. As can be seen,  $S_{11}$  parameters are better for the wider band-stop-filters. Logically, using Bloch calculation (15c),  $S_{11}$  parameters are totally matched only for the central frequency (3 GHz in Fig.6.) and much higher on the boundaries. Optimization is in direction of equalizing maximums of the  $S_{11}$  parameters in the whole band-pass region. In order to do that impedance  $Z$  calculated in (15c) need to be something lower. Optimized results are for the case with equal values of  $S_{11}$  for the 1<sup>st</sup>, 6<sup>th</sup>, 3<sup>rd</sup> and 4<sup>th</sup> maximums in the bandpass. New optimized results are presented in Fig. 7a and 7b. Steepness of the filter is better for more cells but problem is dimensions. One cell longitudinal dimension is  $\lambda/2$ . 4-cells filter is chosen as optimal and for -3 dB criteria  $RBW$  is shifted only 3%.

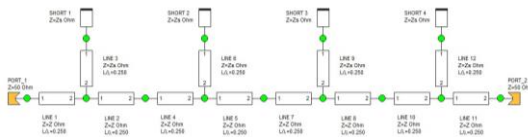


Fig. 5. Ideal model of a 4-cells filter with identical cells.

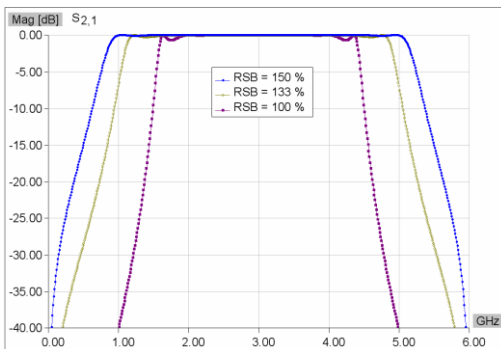
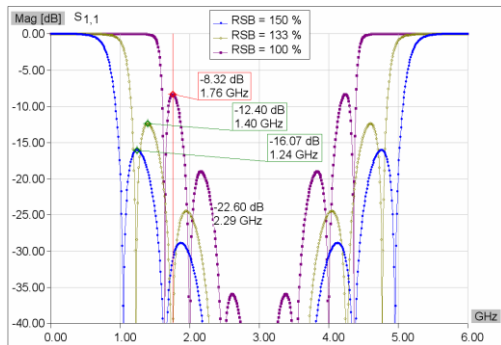


Fig. 6a,b Three wideband filters in the ideal model of 4 cells according to Bloch impedance (15c).

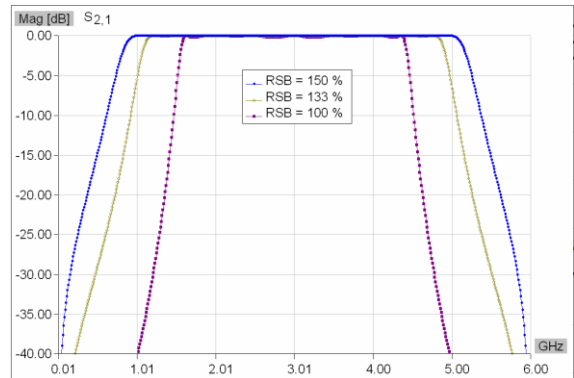
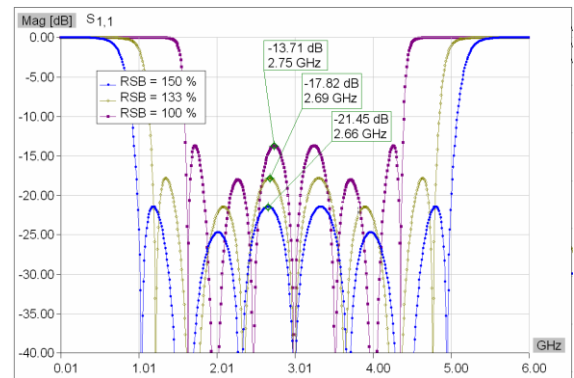


Fig. 7a,b Three wideband filters in the ideal model of 4 cells with something lower  $Z$ .

#### IV. CONCLUSION

This paper presents algorithm for the broad range of values of wide relative bandwidth ( $RBW$ ) up to 1.6. The algorithm is based on periodic ideal waveguide cells each with short-ended stub. Design curve of the ratio between characteristic impedences of the short-ended stub and characteristic impedences of the main lines is given for the broad range of values of  $RBW$ . Characteristic impedences are at first calculated according to the Bloch impedance and then slightly optimized for the optimal  $S_{11}$  parameters in the whole bandpass region.

Very high  $RBW$  needs huge ratio between  $Z_s$  and  $Z$  and it is not realizable. Along with microstrip the algorithm can be also applied to stripline and coplanar waveguide (CPW).

#### REFERENCES

- [1] Z.-C. Hao and J.-S. Hong, Ultrawideband filter technologies, IEEE Microwave Magazine, vol.11, no.4, pp.56-68, 2010.
- [2] R. Zhang and D. Peroulis, Planar Multifrequency Wideband Bandpass Filters With Constant and Frequency Mappings, IEEE Transactions on Microwave Theory and Techniques, vol.66, no.2, pp.935-942, 2018.
- [3] R. Zhang, S. Luo, L. Zhu, A New Synthesis and Design Method for Wideband Bandpass Filters With Generalized Unit Elements, Transactions on Microwave Theory and Techniques, vol. 65, no. 3, pp. 815-823, 2017.
- [4] L.-T. Wang, Y. Xiong and M. He (2019). Review on UWB Bandpass Filters, UWB Technology - Circuits and Systems, Mohamed Kheir, IntechOpen, DOI: 10.5772/intechopen.87204. Available from: <https://www.intechopen.com/books/uwb-technology-circuits-and-systems/review-on-uwb-bandpass-filters>.

- [5] M. S. Razalli, A. Ismail, M. A. Mahd and M. N. Hamidon, Compact Configuration Ultra- Wideband Microwave Filter Using Quarter-Wave Length Short-Circuited Stub, Proceedings of Asia-Pacific Microwave Conference 2007.
- [6] J.-S. Hong and H. Shaman, An Optimum Ultra-Wideband Microstrip Filter, Microwave and Optical Technology Letters, vol. 47, no. 3, pp.230-233, 2005.
- [7] W.-T. Wong, Y.-S. Lin, C.-H. Wang, and C. H. Chen, Highly Selective Microstrip Bandpass Filters for Ultra-Wideband (UWB) Applications, Proceedings of Asia-Pacific Microwave Conference 2005.
- [8] M. S. Razalli A. Ismail, M. A. Mahdi and M. N. Hamidon, Ultra-Wide Band Microwave Filter Utilizing Quarter-wavelength Short-Circuited Stubs, Microwave and Optical Technology Letters, Vol. 50, no. 11, pp. 2981-2983, 2008.
- [9] M. S. Razalli, A. Ismail, M. A. Mahdi and M. N. Hamidon, Compact Ultra-Wide Band Microwave Filter Utilizing Quarter-Wave Length Short Circuited Stubs with Reduced Number of Vias, Microwave and Optical Technology Letters, vol. 51, no. 9, pp. 2116-2119, 2009.
- [10] D. A. Nesic, B. M. Kolundzija, D. V. Tosic and D. S. Jeremic, Low-pass filter with deep and wide stop band and controllable rejection bandwidth, *International Journal of Microwave and Wireless Technologies*, Vol. 7, Iss. 2, 2015, pp. 141-149
- [11] D. M. Pozar, *Microwave Engineering*. 3rd ed., John Wiley and Sons, 2012.
- [12] Program Package WIPL-D Microwave Pro v5.1 (WIPL-D d.o.o, Belgrade 2019. [www.wipl-d.com](http://www.wipl-d.com))

# Numeričko računanje konačnog dela Zomerfeldovih integrala u blizini razdvojne površi vazduha i metamaterijala negativne permitivnosti

Nikola Basta i Branko Kolundžija, *Fellow, IEEE*

**Apstrakt**—Predložen je numerički pristup rešavanju konačnog dela Zomerfeldovog integrala koji odgovara rasejanom potencijalu vertikalnog Hercovog dipola u okolini spoja dve linearne sredine – vazduha i metamaterijala negativne permitivnosti. Integral je računat duž realne putanje integracije primenom Gaus-Ležandrove kvadrature formule. U analitičkoj pripremi integrala, primenom smene promenljivih i ekstrakcije singulariteta, poništen je singularni uticaj tačaka grananja i pola podintegralne funkcije, respektivno. Predložen pristup verifikovan je numeričkim primerima i poređenjem sa drugom metodom.

**Ključne reči**—Zomerfeldovi integrali; poništavanje singulariteta; pol; tačka grananja; smena promenljivih;

## I. UVOD

ANALIZA izvora elektromagnetskog zračenja u prisustvu dve linearne sredine (eng. *half-space problem*), predstavlja klasu problema koja se istražuje već više od jednog veka [1], [2]. Rešavanje ovakvog problema počiva na tzv. Zomerfeldovim integralima (ZI) [1]. S obzirom na današnju potrebu za tačnijim i efikasnijim metodama elektromagnetske analize koje bi omogućile analizu električki velikih struktura na širokom opsegu učestanosti, ZI su i dalje aktuelni, što potvrđuju brojne publikacije poslednjih godina, kao što su [3]–[5]. Osnovni izazovi u numeričkoj proceni ZI jesu njihova oscilatornost, singularnost i polubeskonačni interval integracije [1], [2], [6]. U ovom radu, posvećujemo pažnju konačnom delu ZI [7], odnosno metodama za prevazilaženje singulariteta, tj. pola i tačaka grananja, koji se nalaze na ili blizu putanje integracije [7], [8]. Pol i tačke grananja mogu značajno uticati na tačnost numeričke integracije. Njihovo postojanje i karakter su direktno uslovljeni električnim osobinama dveju razmatranih sredina.

U dosadašnjim istraživanjima, u tipičnim scenarijima, razmatrani su tzv. desno orijentisani materijali, u kojima za ekvivalentnu permitivnost i permeabilnost važi  $\text{Re}\{\epsilon_e\} > 0$  i  $\text{Re}\{\mu_e\} > 0$ . To je slučaj i u analizi antene u vazduhu, neposredno iznad realnog zemljišta [1], [2], [6]. Međutim, u savremenim primenama, kao što je interakcija plazme ili određenih metala sa elektromagnetskim poljem visoke učestanosti, može se desiti da realni deo ekvivalentne permitivnosti postane

negativan [9], [10]. Sa druge strane, specijalni feritni materijali u kombinaciji sa metalnim strukturama ili stranim magnetskim poljem mogu se konstruisati tako da je njihova ekvivalentna permeabilnost negativna [11]–[13]. Ovi efekti su od velikog značaja za oblast fizike koja se bavi optoelektronskim komponentama, bio-senzorima, sočivima, kao i formiranjem slike (eng. *imaging*) na nanoskali [14]. Iako je za postizanje željenog efekta potreban izvor elektromagnetskog polja čija radna učestanost je bliska optičkim, specijalnim periodičnim mikrostrukturama, izrađenim od odgovarajućih elemenata, može se formirati veštački materijal kod kojeg se isti efekat postiže na učestanostima značajno nižim od optičkih, reda veličine teraherca i gigaherca [10], [14]–[18]. Takvi materijali se nazivaju *metamaterijalima* i poslednjih decenija posvećena im je velika pažnja, o čemu svedoči veliki broj publikacija [14]. U ovom radu, razmotrićemo primer materijala sa negativnom permitivnošću (ENG – eng. *ε-negative*) kao jednu od dve linearne sredine u čijoj blizini se nalazi izvor zračenja. Međutim, prikazana saznanja se odnose i na materijale sa negativnom permeabilnošću (eng. *μ-negative*) i tzv. dvostruko negativne materijale (eng. *double negative*), kod kojih je  $\text{Re}\{\epsilon_e\} < 0$  i  $\text{Re}\{\mu_e\} < 0$ .

Makroskopski gledano, postojeće modele koji opisuju zavisnost permitivnosti nekog veštačkog materijala od učestanosti (npr. Drudov ili Lorencov model [15], [19]) možemo direktno uvrstiti u Maksvelove jednačine. U scenariju sa dve linearne nemagnetske sredine, od kojih je prva vazduh, a druga ENG metamaterijal, tj. metal u kojem je za datu učestanost  $\text{Re}\{\epsilon_e\} < 0$ , u podintegralnoj funkciji ZI se pojavljuju singulariteti – tačke grananja i pol. Cilj ovog rada jeste analiza singulariteta, odnosno razvoj metode za potiskivanje njihovog uticaja radi efikasnog numeričkog računanja konačnog dela ZI s visokom tačnošću.

## II. POSTAVKA PROBLEMA

U scenariju prikazanom na sl. 1, izvor (tačka *A*) je vertikalni Hercov dipol (VHD), koji se nalazi na *z*-osi, na visini *z'* iznad ravnih koja predstavlja razdvojnu površ vazduha (sredina 1) i ENG metamaterijala (sredina 2). Na istoj visini, na horizontalnom rastojanju  $\rho$ , nalazi se tačka u kojoj posmatramo polje, *P*. Problem ćemo dalje razmatrati na primeru *reflektovanog* ZI, tj. integralnoj predstavi rasejanog potencijala VHD,

$$I_{r,zz}(0, b) = \int_0^b R_{zz}(k_\rho) J_0(\rho k_\rho) e^{-\gamma_{z0}(|z|+|z'|)} \frac{k_\rho dk_\rho}{\gamma_{z0}}, \quad (1)$$

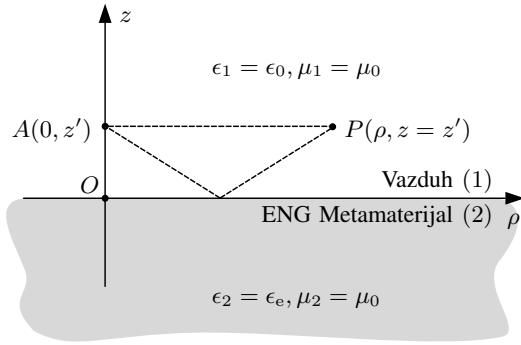
Nikola Basta is with the School of Electrical Engineering, University of Belgrade, 73 Bulevar kralja Aleksandra, 11120 Belgrade, Serbia (e-mail: nbasta@etf.rs).

Branko Kolundžija is with the School of Electrical Engineering, University of Belgrade, 73 Bulevar kralja Aleksandra, 11120 Belgrade, Serbia (e-mail: kol@etf.rs)

gde je  $R_{zz}$  generalisani koeficijent refleksije,  $J_0$  Beselova funkcija prve vrste i nultog reda,  $\gamma_{z0} = \sqrt{k_\rho^2 - k_0^2}$ ,  $k_0 = \omega\sqrt{\epsilon_0\mu_0}$ . U razmatranom slučaju je  $\epsilon_1 = \epsilon_0$ ,  $\epsilon_2 = \epsilon_e$ ,  $\mu_1 = \mu_2 = \mu_0$ , te se generalisani koeficijent refleksije može izraziti kao

$$R_{zz}(k_\rho) = \frac{N_{R_{zz}}(k_\rho)}{D_{R_{zz}}(k_\rho)} = \frac{k^2\sqrt{k_\rho^2 - k_0^2} - k_0^2\sqrt{k_\rho^2 - k^2}}{k^2\sqrt{k_\rho^2 - k_0^2} + k_0^2\sqrt{k_\rho^2 - k^2}}, \quad (2)$$

gde  $N_{R_{zz}}$  i  $D_{R_{zz}}$  predstavljaju brojilac i imenilac,  $k = \omega\sqrt{\epsilon_e\mu_0}$ . U izrazima  $R_{zz}$  i  $\gamma_{z0}$  uočavamo tačke grananja korenih funkcija,  $k_\rho = k_0$  i  $k_\rho = k$ , koje prouzrokuju beskonačne vrednosti integranda, odnosno njegovih izvoda. Integracija se vrši po realnoj osi, a gornja granica integrala,  $b$ , je odabrana tako da je dovoljno daleko od tačaka grananja (i eventualnog pola),  $b > \max\{k_0, \text{Re}\{k\}\}$ . Napominjemo da u ovom radu razmatramo konačan deo ZI, te je  $b < +\infty$ . Od posebnog interesa je kritičan slučaj, kada su singulariteti blizu putanje integracije, tj. kada jedna od sredina ima male gubitke [7]. Iz tog razloga usvajamo za sredinu 2 metamaterijal ENG tipa, čija je ekvivalentna permitivnost  $\epsilon_e = \epsilon_0\epsilon_{er}$ , gde je  $\epsilon_{er} = -4 - j0,01$ .



Sl. 1. Scenarij sa razdvojnjom površju vazduha i ENG metamaterijala. Izvor se nalazi u tački A, a tačka posmatranja je P.

### III. POTISKIVANJE SINGULARNOG UTICAJA TAČAKA GRANANJA PRIMENOM SMENE PROMENLJIVIH

Za numeričko računanje integrala (1) sa prihvatljivom tačnošću, neohodno je potisnuti uticaj singulariteta. Singularni uticaj tačaka grananja može se potisnuti primenom smene promenljivih [7], [8]. Radi povećanja efikasnosti, pre primene smene, domen integracije možemo podeliti na poddomene, a singularne tačke grananja, odnosno njihove projekcije na realnu osu,  $k_0$  i  $k_{re} = \text{Re}\{k\}$ , predstavljaju pogodno mesto za granice novih poddomena [7]. Dodatnu granicu, koja omogućava nezavisno tretiranje dve tačke grananja, definišemo kao aritmetičku sredinu dveju prvobitnih granica, kao što je prikazano na sl. 2. Na taj način imamo četiri poddomena, a time i četiri određena integrala, čije vrednosti treba proceniti. Sledi da ZI nad konačnim intervalom možemo izraziti kao  $I_{r,zz}(0, b) = I_1 + I_2 + I_3 + I_4$ , gde je

$$\begin{aligned} I_1 &= I_{r,zz}(0, k_{re}), & I_2 &= I_{r,zz}\left(k_{re}, \frac{k_0 + k_{re}}{2}\right), \\ I_3 &= I_{r,zz}\left(\frac{k_0 + k_{re}}{2}, k_0\right), & I_4 &= I_{r,zz}(k_0, b), \end{aligned} \quad (3)$$

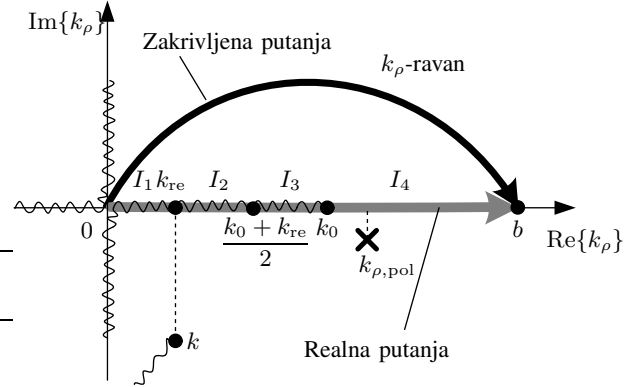
a gornja granica iznosi  $b = k_0\sqrt{2}$  [7], [20].

Radi transformacije integrala u oblik pogodniji za numeričko računanje, definišemo smene promenljivih [7],

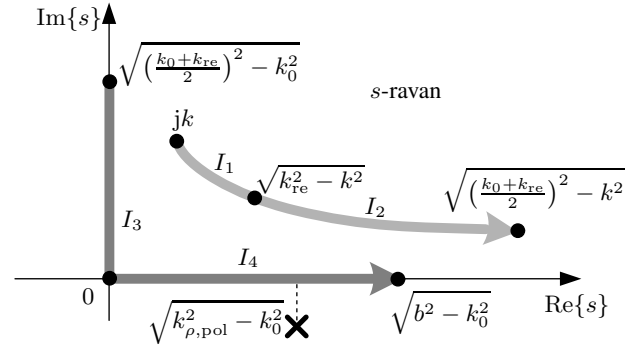
$$s = \sqrt{k_\rho^2 - k^2} \Rightarrow k_\rho = \sqrt{s^2 + k^2}, \quad \text{za } I_1 \text{ i } I_2, \quad (4)$$

$$s = \sqrt{k_\rho^2 - k_0^2} \Rightarrow k_\rho = \sqrt{s^2 + k_0^2}, \quad \text{za } I_3 \text{ i } I_4, \quad (5)$$

gde za obe smene važi  $k_\rho dk_\rho = s ds$ . Na ovaj način, potiskuje se singularni uticaj tačaka grananja, kao što će biti pokazano u odeljku V. Putanje integracije nakon smene prikazane su u kompleksnoj  $s$ -ravni na sl. 3.



Sl. 2. Prikaz realne putanje (siva linija) i zakrivljene putanje (crna linija) u kompleksnoj  $k_\rho$ -ravni za  $\text{Re}\{\epsilon_{er}\} < 0$  i  $\text{Im}\{\epsilon_{er}\} < 0$ . Projekcije talasnih brojeva na realnu osu i njihova aritmetička sredina predstavljaju granice poddomena. Usled negativnog realnog dela permitivnosti, pol se pojavljuje u blizini realne ose sa kritične desne strane u odnosu na  $k_0$ .



Sl. 3. Putanje integracije (sive linije) i singulariteti predstavljani u preslikanoj, kompleksnoj  $s$ -ravni.

### IV. EKSTRAKCIJA POLA PODINTEGRALNE FUNKCIJE

Na spoju vazduha i ENG metamaterijala, može se javiti posebna vrsta talasa u vidu površinskog plazmon-polaritona (SPP - eng. *surface plasmon polariton*). Fenomen SPP nastaje usled sprege oscilatornog EM polja i slobodnih nosilaca u metalu. Uslov za njegovo pojavljivanje na razdvojnoj površju sredina 1 i 2 glasi [14]

$$\text{Re}\{\epsilon_{e1}\} \text{Re}\{\epsilon_{e2}\} < 0, \quad \text{Re}\{\epsilon_{e1}\} + \text{Re}\{\epsilon_{e2}\} < 0, \quad (6)$$

gde je, u odnosu na [14], ovde iskaz uslova uopšten i izražen preko realnih delova ekvivalentnih permitivnosti, kako bi se u

račun uključio i slučaj sa gubicima. Za slučaj malih gubitaka, koji je u ovom radu razmatran, SPP se u literaturi naziva i Fanoov mod [3]. Pojava tzv. površinskog talasa je direktno povezana sa položajem pola podintegralne funkcije u kompleksnoj ravni (videti Dodatak). Pol u slučaju našeg integranda predstavlja nulu imenioca generalisanog koeficijenta refleksije. Rešavanjem jednačine

$$D_{Rzz}(k_\rho) = k^2 \sqrt{k_\rho^2 - k_0^2} + k_0^2 \sqrt{k_\rho^2 - k^2} = 0, \quad (7)$$

dobija se  $k_\rho = \pm k_{\rho, \text{pol}}$ , gde je

$$k_{\rho, \text{pol}} = \sqrt{\frac{k_0^2 k^2}{k_0^2 + k^2}} = k_0 \sqrt{\frac{\epsilon_{\text{er}}}{1 + \epsilon_{\text{er}}}}. \quad (8)$$

Za odabrano  $\epsilon_{\text{er}}$ , rešenje jednačine  $D_{Rzz} = 0$ , dato izrazom (8), iznosi  $k_{\rho, \text{pol}} \approx k_0(1,1547 - j0,0005)$ . Ovaj broj se nalazi u IV kvadrantu kompleksne  $k_\rho$ -ravni (pozitivan predznak rešenja jednačine  $D_{Rzz} = 0$ ), *desno* od tačke grananja  $k_0$  u neposrednoj blizini realne ose, odnosno realne putanje integracije (sl. 2). Takav pol nepovoljno utiče na tačnost i konvergenciju numeričkog računanja integrala i povezuje se sa pojavom površinskog talasa SSP tipa (videti Dodatak).

Primenom smene, pol se u kompleksnoj  $s$ -ravni preslikava u  $s_{\text{pol}} = \sqrt{k_{\rho, \text{pol}}^2 - k_0^2} \approx k_0(0,5773 - j0,0010)$ , što je takođe u IV kvadrantu i blizu realne ose. Kako u  $s$ -ravni domen integracije integrala  $I_4$  ide duž realne ose (sl. 3), zaključujemo da i u domenu nove promenljive, preslikani pol ugrožava tačnost i konvergenciju integrala. Korišćenjem tehnike ekstrakcije singulariteta, oduzimanjem i dodavanjem pogodnog singularnog izraza, čiji integral je analitički rešiv [21], [22], integral  $I_{r,zz}$  se nakon primenjene smene može izraziti u obliku

$$\begin{aligned} I_{r,zz} &= \int_{s_1}^{s_2} f_{r,zz}(s) ds \\ &= \int_{s_1}^{s_2} \left( f_{r,zz}(s) - \frac{R_{\text{pol}}}{s - s_{\text{pol}}} \right) ds + I_{\text{Res}}, \end{aligned} \quad (9)$$

gde je  $f_{r,zz}(s)$  podintegralna funkcija integrala  $I_{r,zz}$  nakon smene, a  $R_{\text{pol}}$  njen ostatak u tački  $s = s_{\text{pol}}$ ,

$$R_{\text{pol}} = \text{Res}_{s=s_{\text{pol}}} f_{r,zz}(s) = \lim_{s \rightarrow s_{\text{pol}}} (s - s_{\text{pol}}) f_{r,zz}(s). \quad (10)$$

Veličina  $I_{\text{Res}}$  se računa analitički integraljenjem oduzetog izraza

$$\begin{aligned} I_{\text{Res}} &= \int_{s_1}^{s_2} \frac{R_{\text{pol}}}{s - s_{\text{pol}}} ds = R_{\text{pol}} \left[ \ln \left| \frac{s_1 - s_{\text{pol}}}{s_2 - s_{\text{pol}}} \right| \right. \\ &\quad \left. + j(\arg\{s_2 - s_{\text{pol}}\} - \arg\{s_1 - s_{\text{pol}}\}) \right]. \end{aligned} \quad (11)$$

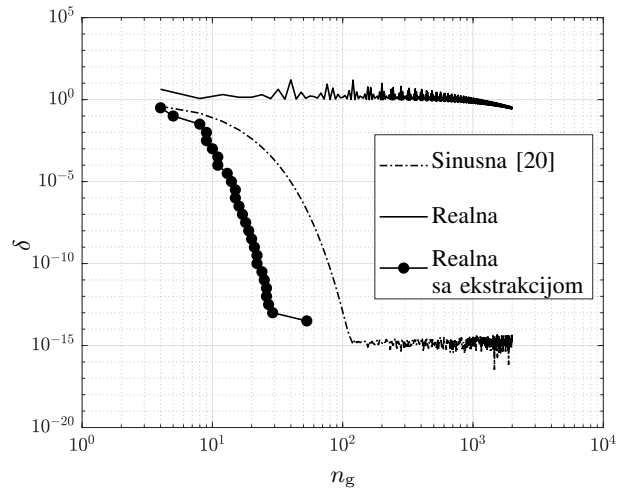
Ovakvom analitičkom pripremom, uticaj pola podintegralne funkcije je potisnut i možemo pristupiti numeričkoj integraciji.

## V. NUMERIČKI PRIMERI

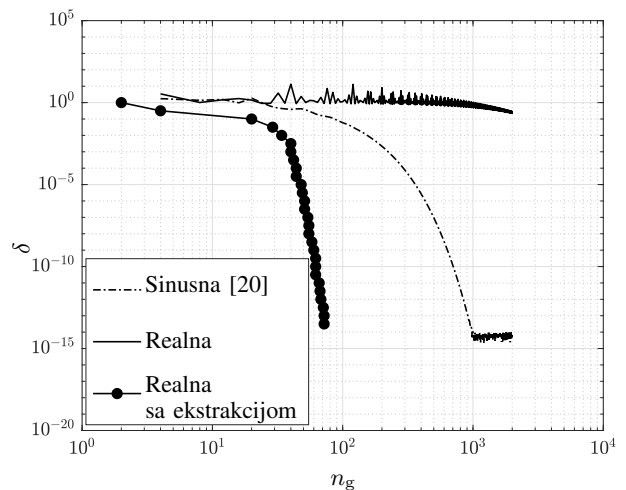
Radi provere efikasnosti smene promenljivih i ekstrakcije pola u sadejstvu, posmatran integral  $I_{r,zz}$  je razmatran za  $z = z' = 0$  i  $\rho/\lambda_0 \in \{1, 10, 100\}$ . Ovaj skup slučajeva je odabran,

jer se nultim vertikalnim rastojanjem ukida prigušenje anvelope usled eksponencijalnog faktora u podintegralnoj funkciji, te je otklonjena mogućnost da se dejstvo pola potre malim vrednostima funkcije prouzrokovanih prigušenjem. Takođe, bliskost izvora zračenja razdvojnoj površi odgovara velikom broju primera iz prakse, kao što su radio i geo-radarski predajnici neposredno iznad zemlje.

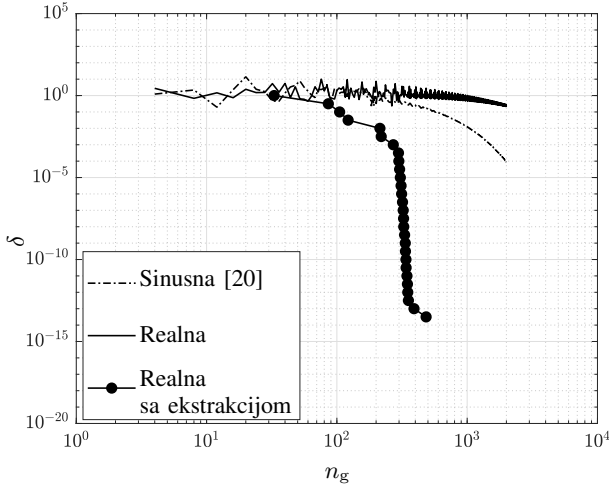
Za date slučajeve, relativna greška u funkciji potrebnog broja integracionih tačaka  $n_g$ , prikazana je na sl. 4–6. Integral je računat na tri načina - duž sinusne zakrivljene putanje (sl. 2) i duž realne putanje sa i bez ekstrakcije pola. Referentna zakrivljena putanja sinusnog oblika je zadata prema [20], gde je istaknuta zavisnost visine putanje od horizontalnog rastojanja  $\rho$ . Ovakva adaptivna putanja se pokazala superiornom u pogledu tačnosti u odnosu na ostale kanonične putanje iz literature koje su definisane fiksnim parametrima.



Sl. 4. Poređenje relativne greške računanja integrala  $I_{r,zz}$  pomoću sinusne putanje [20], realne putanje bez ekstrakcije pola i realne putanje sa ekstrakcijom pola za  $\rho = \lambda_0$  i  $z = z' = 0$ .



Sl. 5. Poređenje relativne greške računanja integrala  $I_{r,zz}$  pomoću sinusne putanje [20], realne putanje bez ekstrakcije pola i realne putanje sa ekstrakcijom pola za  $\rho = 10\lambda_0$  i  $z = z' = 0$ .



Sl. 6. Poređenje relativne greške računanja integrala  $I_{r,zz}$  pomoću sinusne putanje [20], realne putanje bez ekstrakcije pola i realne putanje sa ekstrakcijom pola za  $\rho = 100\lambda_0$  i  $z = z' = 0$ .

Posmatrajući krivu greške za realnu putanju kada je primenjena samo smena promenljivih, vidimo da je pol dovoljno blizu putanje integracije, te prouzrokuje grešku reda veličine  $\delta \sim 0,1 \div 10$ . Smena promenljivih u kombinaciji sa ekstrakcijom uspešno potiskuje dejstva tačaka grananja i pola, pa je dostignuta tačnost visoka. Integracija zakrivljenom sinusnom putanjom rezultuje nivoima greške koji su prihvatljivi za malo  $\rho$ , te se može pretpostaviti da je sinusna putanja dovoljno udaljena od pola. Međutim, dejstvo singularne tačke grananja  $k_\rho = k_0$ , a time i velikih vrednosti Beselove funkcije kompleksnog argumenta u I kvadrantu, je i dalje vidljivo. Osetljivost integracije duž zakrivljene putanje dolazi do izražaja naročito za veće  $\rho$  (sl. 6). S obzirom na veću robusnost sa aspekta horizontalnog rastojanja i lakoću implementacije ekstrakcije pola, u datom scenariju se predložena metoda sa korenom smenom promenljivih i realnom putanjom pokazuje kao pogodniji pristup.

## VI. ZAKLJUČAK

Realna putanja integracije i Gaus-Ležandrova kvadratura formula primenjeni su u numeričkom računanju Zomerfeldovog integrala za rasejani potencijal vertikalnog Hercovog dipola na spoju vazduha i metamaterijala negativne permitivnosti. Singularni uticaj tačaka grananja potisnut je primenom smene promenljivih, dok je pol uklonjen primenom tehnike ekstrakcije singulariteta nakon uvrščivanja smene. Na ovaj način omogućeno je efikasno računanje integrala sa visokom tačnošću. U poređenju sa metodama sa zakrivljenom putanjom integracije, predloženi pristup omogućava višu tačnost u širokom opsegu horizontalnih rastojanja izvora i tačke posmatranja.

## DODATAK

U zavisnosti od osobina dve linearne sredine, na njihovoj razdvojnoj površi može doći do pojave nekog od različitih oblika površinskog elektromagnetskog talasa, koji u manjoj

ili većoj meri doprinosi ukupnom talasu. Pojava površinskog talasa je usko povezana sa polovima podintegralne funkcije Zomerfeldovog integrala pomoću kojeg izražavamo EM polje. U ovom dodatku, na primeru reflektovanog Zomerfeldovih integrala, analiziraćemo uslov za postojanje polova i njihov singularni uticaj na numeričko računanje integrala.

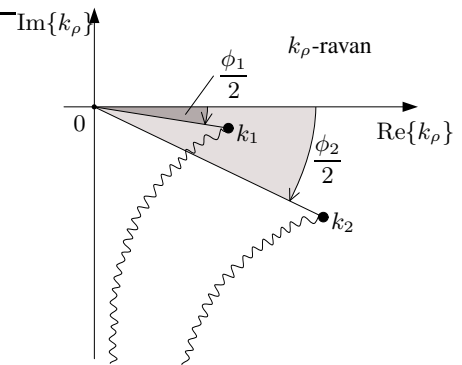
Izjednačimo sa nulom imenilac generalisanog koeficijenta refleksije za vertikalni Hercov dipol na razdvojnoj površi dve linearne nemagnetske sredine ( $\mu_1 = \mu_2 = \mu_0$ ),

$$D_{Rzz} = k_2^2 \sqrt{k_\rho^2 - k_1^2} + k_1^2 \sqrt{k_\rho^2 - k_2^2} = 0, \quad (12)$$

gde su  $k_1$  i  $k_2$  talasni brojevi prve i druge sredine. Tada kažemo da je ispunjen tzv. uslov rezonancije. Pravolinijskim rešavanjem jednačine (12), prebacivanjem na drugu stranu jednakosti, kvadriranjem i određivanjem rešenja po  $k_\rho$ , dobijamo izraz za pol<sup>1</sup>

$$k_\rho = \pm k_{\rho,\text{pol}}, \quad k_{\rho,\text{pol}} = \sqrt{\frac{k_1^2 k_2^2}{k_1^2 + k_2^2}}. \quad (13)$$

Međutim, kako se kvadriranjem gubi informacija o izboru grana u korenim funkcijama, nije jasno pod kojim uslovima takvo rešenje jednačine zaista postoji i u kakvoj su svezi ti uslovi sa svojstvima dveju sredina. Da bismo to razjasnili, pomenutu jednačinu rešićemo postupno, sa osvrtom na izbor grana. Radi jednostavnosti, razmatraćemo slučaj kada su  $k_1$  i  $k_2$  u IV kvadrantu  $k_\rho$ -ravni, što odgovara tipičnim sredinama sa gubicima. Neka su argumenti kompleksnih veličina  $k_1^2$  i  $k_2^2$  dati uglovima  $\phi_1$  i  $\phi_2$ , ( $|\phi_2| > |\phi_1|$ ), respektivno, i neka je  $\arg\{k_1^2 + k_2^2\} = \phi$ , kao na sl. 7. Zaseci su prikazani talasastim linijama, a njihov oblik odgovara hiperbolama, definisanim jednačinama  $\text{Im}\{k_{z1,2}\} = 0$ , gde je  $k_{z1,2} = \sqrt{k_{1,2}^2 - k_\rho^2}$  talasni broj u pravcu  $z$ -ose. Ovakav odabir zaseka korišćen je u originalnom Zomerfeldovom radu [1]. Imenilac u okolini



Sl. 7. Tačke grananja i zaseci podintegralne funkcije za slučaj dve sredine sa gubicima, čiji talasni brojevi su  $k_1$  i  $k_2$ . Talasaste linije predstavljaju zaseke odgovarajućih korenih funkcija.

<sup>1</sup>Ovaj izraz jeste pol kada je  $\text{Im}\{k_{z1}\} < 0$  i  $\text{Im}\{k_{z2}\} < 0$ , što odgovara prvoj, regularnoj grani funkcija  $k_{z1}$  i  $k_{z2}$ . Drugaćijim odabirom grana, dati izraz postaje nula brojioca. Ovo se postiže u tzv. neregularnoj grani, odnosno neregularnom listu Rimanove površi (eng. *improper Riemann sheet*), i tada se dati izraz zove *Brusterova nula* [23], [24].

pola postaje

$$\begin{aligned}
D_{Rzz}(k_{\rho,\text{pol}}) &= k_2^2 \sqrt{k_{\rho,\text{pol}}^2 - k_1^2} + k_1^2 \sqrt{k_{\rho,\text{pol}}^2 - k_2^2} \\
&= k_2^2 \sqrt{\frac{-k_1^4}{k_1^2 + k_2^2}} + k_1^2 \sqrt{\frac{-k_2^4}{k_1^2 + k_2^2}} \\
&= |k_2|^2 e^{j\phi_2} \frac{|k_1|^2}{\sqrt{|k_1^2 + k_2^2|}} \sqrt{e^{j(\pi+2\phi_1-\phi)}} \\
&\quad + |k_1|^2 e^{j\phi_1} \frac{|k_2|^2}{\sqrt{|k_1^2 + k_2^2|}} \sqrt{e^{j(\pi+2\phi_2-\phi)}}.
\end{aligned} \tag{14}$$

Da bi izraz (14) bio jednak nuli, potrebno je da dva sabirka nakon korenovanja eksponencijalnih faktora dobiju suprotne predznake. To je moguće samo ako podkorene veličine  $e^{j(\pi+2\phi_1-\phi)}$  i  $e^{j(\pi+2\phi_2-\phi)}$  imaju imaginarnu delove suprotnih predznaka, tj. ako je

$$(2\phi_1 - \phi)(2\phi_2 - \phi) < 0. \tag{15}$$

Drugim rečima, opseg ugla  $\phi$  je određen sa  $2|\phi_1| < |\phi| < 2|\phi_2|$ , odakle sledi potreban uslov za postojanje pola

$$|\phi_2| > 2|\phi_1|. \tag{16}$$

Iako je ovaj uslov često ispunjen u praksi, samo postojanje pola ne znači nužno i da on utiče na numeričku integraciju. Pokazuje se da uticaj pola, pored njegove udaljenosti od putanje integracije, zavisi i od njegovog relativnog položaja u odnosu na tačke grananja, što ćemo ilustrovati primerom.

Rešenje za pol integranda možemo izraziti na sledeći način:

$$k_{\rho,\text{pol}} = k_1 \sqrt{\frac{\kappa}{1 + \kappa}}, \quad \kappa = \frac{k_2^2}{k_1^2}. \tag{17}$$

Neka je, za svrhe našeg primera, sredina 1 bez gubitaka,  $\text{Re}\{k_1\} > 0 \wedge \text{Im}\{k_1\} = 0$ , a sredina 2 sa gubicima,  $\text{Im}\{k_2\} < 0$ . Tada se hiperbolični zasek koji odgovara tački grananja  $k_1$  (sl. 7) deformiše u dva pravolinijska segmenta, kao na sl. 8. Ako definišemo uglove  $\alpha$  i  $\beta$

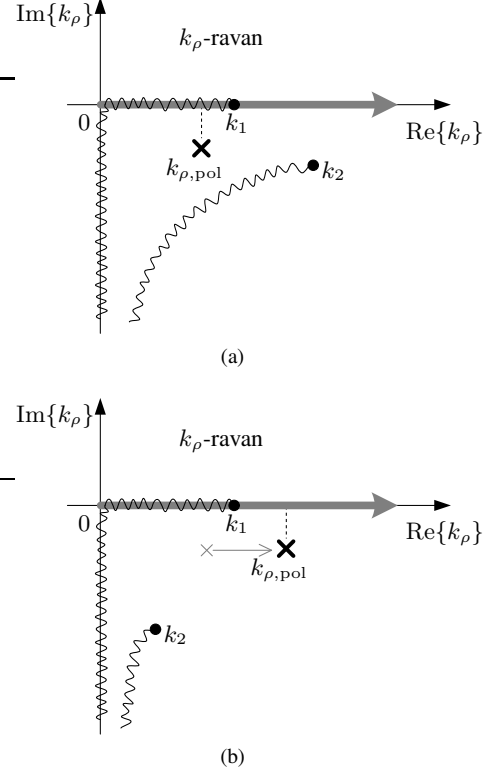
$$\begin{aligned}
\kappa &= |\kappa| e^{j\alpha}, \quad -\pi < \alpha < 0, \\
1 + \kappa &= |1 + \kappa| e^{j\beta}, \quad \alpha < \beta < 0,
\end{aligned} \tag{18}$$

sledi da je [3], [25]

$$k_{\rho,\text{pol}} = k_1 \sqrt{\frac{|\kappa|}{|1 + \kappa|}} e^{j\frac{\alpha-\beta}{2}}. \tag{19}$$

Posmatrajmo najpre slučaj kada je  $\text{Re}\{\kappa\} > 0$ . Tada je  $-\pi/2 < \alpha < 0$  i pol se nalazi u IV kvadrantu, *levo* od  $k_1$ , tj.  $\text{Re}\{k_{\rho,\text{pol}}\} < \text{Re}\{k_1\}$ . Ukoliko usvojimo putanju integracije duž realne ose i pretpostavimo male gubitke u sredini 2, čini se da bi blizina pola putanji integracije mogla značajno umanjiti tačnost rezultata usled velikih vrednosti integranda (sl. 8a). Međutim, s obzirom da se realna putanja integracije nalazi u prvoj, regularnoj grani funkcije  $k_{z1}$  (eng. *proper Riemann sheet*), neposredno iznad zaseka, a da se pol nalazi ispod njega, izbegnut je njegov singularni efekat. To se objašnjava time da se putanja integracije i pol ne nalaze istovremeno u zoni gde je potiranje sabiraka imenioca (14) moguće. Ako je pak  $\text{Re}\{\kappa\} < 0$ , tj.  $-\pi < \alpha < -\pi/2$  (npr. plazma, metamaterijali i određeni metali na visokim učestanostima),

onda se pol nalazi *desno* od tačke grananja  $k_1$ , i to u zoni gde svojom blizinom realnoj osi može prouzrokovati velike vrednosti integranda na putanji integracije, a time i umanjeње tačnosti numeričkog računanja integrala. Pojava pola desno od tačke grananja povezuje se sa pojavom jedne vrste površinskog talasa, kojeg nazivamo površinski plazmon-polariton (SPP - eng. *surface plasmon polariton*) [3], [24], [25].

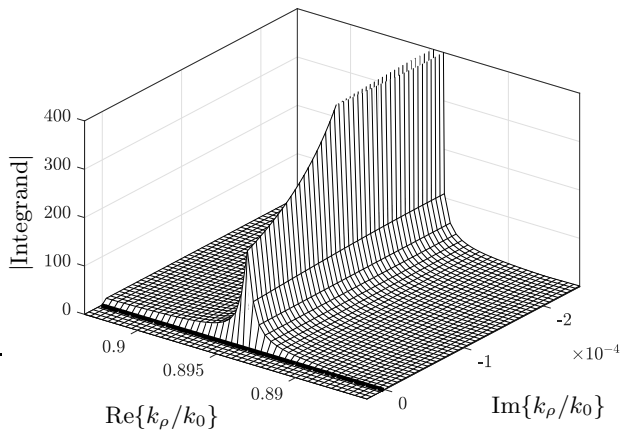


Sl. 8. Relativni položaj pola u odnosu na tačke grananja kada je sredina 2 (a) dielektrik s gubicima i (b) metamaterijal sa  $\text{Re}\{k_2^2\} < 0$ .

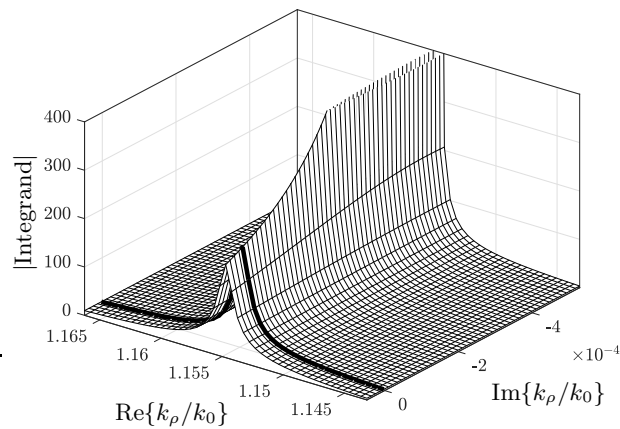
Na sl. 9 prikazan je grafik modula integranda ZI za rasejani potencijal vertikalnog Hercovog dipola u funkciji  $k_{\rho}$ , kada je  $\rho = 10\lambda_0$  i  $z = z' = 0$ . Crna linija predstavlja grafik modula integranda duž realne ose. U datom primeru je  $k_1 = k_0$  i  $k_2 = k_0 \sqrt{\epsilon_{\text{er}}}$ , odnosno  $\kappa = \epsilon_{\text{er}}$ . U prvom slučaju, prikazanom na sl. 8a, efektivna relativna permitivnost je  $\epsilon_{\text{er}} = 4 - j0,01$ , dok je pol  $k_{\rho,\text{pol}} \approx k_0(0,8944 - j0,0002)$ . Kako je  $\text{Re}\{\epsilon_{\text{er}}\} > 0$ , pol je *zaklonjen* zasekom, te ne stvara ekstremne vrednosti, odnosno jake promene u podintegralnoj funkciji. U drugom slučaju je  $\epsilon_{\text{er}} = -4 - j0,01$ , a pol, čija vrednost sada iznosi  $k_{\rho,\text{pol}} \approx k_0(1,1547 - j0,0005)$ , nije više *zaklonjen*, te stvara jak ekstremum na putanji integracije.

## LITERATURA

- [1] A. N. Sommerfeld, "Über die Ausbreitung der Wellen in der Drahtlosen Telegraphie," *Ann. Physik*, vol. 28, pp. 665–736, 1909.
- [2] H. Weyl, "Ausbreitung elektromagnetischer Wellen über einem ebenen Leiter," *Ann. Physik*, vol. 60, pp. 481–500, 1919.
- [3] K. Michalski and J. Mosig, "The Sommerfeld half-space problem revisited: from radio frequencies and zenneck waves to visible light and fano modes," *Journal of Electromagnetic Waves and Applications*, vol. 30, no. 1, pp. 1–42, 2016.
- [4] K. A. Michalski and J. R. Mosig, "Efficient computation of Sommerfeld integral tails – methods and algorithms," *Journal of Electromagnetic Waves and Applications*, vol. 30, pp. 281–317, Mar. 2016.



(a)



(b)

Sl. 9. Prikaz modula integranda ZI za rasejani potencijal vertikalnog Hercovog dipola nad kompleksnom  $k_\rho$ -ravni, kada je  $\rho = 10\lambda_0$  i  $z = z' = 0$ . Grafik je zasečen u okolini pola, a maksimalna prikazana vrednost je ograničena na 400, radi boljeg prikaza. Crna linija predstavlja grafik modula integranda duž realne putanje integracije. (a)  $\epsilon_{er} = 4 - j0,01$ , pol je zaklonjen zasekom i ne utiče na integrand; (b)  $\epsilon_{er} = -4 - j0,01$ , pol nije zaklonjen zasekom i stvara ekstremum;

- [5] R. Trembinski and D. A. McNamara, "The engineering modelling of electromagnetic wave scattering from sea ice by surface-based radar," in *Proc. 2018 IEEE Int. Symp. Ant. Prop. (APS/URSI)*, Boston, MA, July 2018.
- [6] V. Petrović, *Analiza žičanih antena u prisustvu realnog zemljišta metodom likova*, doktorska disertacija, Elektrotehnički fakultet Univerziteta u Beogradu, Beograd, 1993.
- [7] N. Basta and B. Kolundžija, "Efficient evaluation of the finite part of pole-free Sommerfeld integrals in half-space problems with predefined accuracy," *IEEE Transactions on Antennas and Propagation*, vol. 67, no. 7, pp. 4930–4935, 2019.
- [8] N. Basta and B. Kolundžija, "On efficient evaluation of pole-free Sommerfeld integrals," in *Proc. 2019 Int. Conf. on Electrical, Electronic and Computing Engineering (IcETRAN)*, Srebrno jezero, June 2019.
- [9] J. A. Bittencourt, *Fundamentals of Plasma Physics*. New York: Springer-Verlag, 2004.

- [10] W. Rotman, "Plasma simulation by artificial dielectrics and parallel-plate media," *IRE Transactions on Antennas and Propagation*, vol. 10, no. 1, pp. 82–95, 1962.
- [11] G. Dewar, "A thin wire array and magnetic host structure with  $n < 1$ ," *Journal of Applied Physics*, vol. 97, no. 10, p. 10Q101, 2005.
- [12] F. J. Rachford, D. N. Armstead, V. G. Harris, and C. Vittoria, "Simulations of ferrite-dielectric-wire composite negative index materials," *Phys. Rev. Lett.*, vol. 99, p. 057202, July 2007.
- [13] Y. Huang, G. Wen, Y. Yang, and K. Xie, "Simulations of ferrite-dielectric-wire composite negative index materials," *Appl. Phys. A*, vol. 106, p. 79–86, 2012.
- [14] L. Solymar and E. Shamonina, *Waves in Metamaterials*. New York: Oxford University Press, 2009.
- [15] J. B. Pendry, A. J. Holden, W. J. Stewart, and I. Youngs, "Extremely low frequency plasmons in metallic mesostructures," *Phys. Rev. Lett.*, vol. 76, pp. 4773–4776, Jun 1996.
- [16] J. B. Pendry, "Negative refraction makes a perfect lens," *Phys. Rev. Lett.*, vol. 85, pp. 3966–3969, Oct. 2000.
- [17] D. Gérard and S. K. Gray, "Aluminium plasmonics," *Journal of Physics D: Applied Physics*, vol. 48, p. 184001, dec 2014.
- [18] Y. Li, *Plasmonic Optics: Theory and Applications*. Bellingham: SPIE Press, 2017.
- [19] R. W. Ziolkowski and E. Heyman, "Wave propagation in media having negative permittivity and permeability," *Physical Review E: Statistical, nonlinear, and soft matter physics*, vol. 64, p. 056625, Oct 2001.
- [20] R. Golubovic, A. G. Polimeridis, and J. R. Mosig, "Efficient algorithms for computing Sommerfeld integral tails," *IEEE Transactions on Antennas and Propagation*, vol. 60, pp. 2409–2417, May 2012.
- [21] J. R. Mosig and T. K. Sarkar, "Comparison of quasi-static and exact electromagnetic fields from a horizontal electric dipole above a lossy dielectric backed by an imperfect ground plane," *IEEE Transactions on Microwave Theory and Techniques*, vol. 34, pp. 379–387, Apr. 1986.
- [22] J. R. Mosig, "Integral equation technique," in *Numerical Techniques for Microwave and Millimeter-wave Passive Structures* (T. Itoh, ed.), New York: Wiley, 1989.
- [23] A. Ishimaru, J. R. Thomas, and S. Jaruwatanadilok, "Electromagnetic waves over half-space metamaterials of arbitrary permittivity and permeability," *IEEE Transactions on Antennas and Propagation*, vol. 53, no. 3, pp. 915–921, 2005.
- [24] A. Ishimaru, *Waves in Inhomogeneous and Layered Media*, ch. 3, pp. 7–34. John Wiley and Sons, 2017.
- [25] K. A. Michalski and J. R. Mosig, "On the surface fields excited by a hertzian dipole over a layered halfspace: From radio to optical wavelengths," *IEEE Transactions on Antennas and Propagation*, vol. 63, no. 12, pp. 5741–5752, 2015.

## ABSTRACT

A numerical approach to computation of the final part of the reflected-potential Sommerfeld integral is proposed for the case of interface of air and negative-permittivity metamaterial. The integral is computed along the real-axis integration path, using Gauss-Legendre quadrature formula. In the analytical preparation of the integral, singular effects of branch-point singularities and pole are canceled by means of change of variables and singularity extraction technique, respectively. The proposed approach is verified through numerical examples and comparison to another method.

## Numerical computation of the finite part of Sommerfeld integrals in the vicinity of interface of air and negative-permittivity metamaterial

Nikola Basta and Branko Kolundžija

# Биосензори реализовани помоћу фреквенцијски селективних површина

Милка Потребих, члан *IEEE*, Дуња Лончаревић и Никола Баста

**Сажетак**— Вирусне инфекције које имају пандемијски потенцијал представљају претњу за цело човечанство. Да би се убрзала дијагностика и повећао капацитет тестирања заразе вирусом, отвара се могућност увођења алтернативних метода дијагностике као што је примена биосензора. Потрага за поузданом алтернативном методом, у последње време заузима све важније место у циљу брже дијагностике, веће осетљивости, неинвазивног и бесконтактнoг мерења. У терахерцном опсегу учестаности, коришћењем сензора на бази фреквенцијски селективних површина - метаматеријала, омогућава се бржа дијагностика и осетљивост откривања нано супстанци. У циљу поузданије детекције вируса инфлуенце А, анализирани су две различите ћелије метаматеријала. Биосензор је пројектован као апсорбер, а за детекцију као референтни параметар коришћен је коефицијент апсорпције. Анализирају се фреквенцијски помераји и промена вредности коефицијента апсорпције са и без постојања вируса. Показује се да јединични елемент са више резонантних учестаности има већу осетљивост од елемента са једном резонантном учестаношћу.

**Кључне речи**— апсорбер; биосензор; вирус инфлуенце А; јединични елементи; фреквенцијски селективна површина.

## I. Увод

ИНДУСТРИЈСКИ развој потребује реализацију нових адаптивних бежичних сензорских мрежа за опслуживање различитих процеса као што је надзор у индустријској производњи, у еколошке сврхе и за биомедицинске примене. Основне карактеристике нове генерације сензора подразумевају могућност повезивања са другим сензорским чворовима и размену информација, преносивост уређаја компактних димензија са малом потрошњом енергије, као и употребу за континуална мерења која су независна од тренутних услова окружења.

Као поуздана алтернатива постојећим дијагностичким методама, у новије време се уводе биосензори у циљу брже дијагностике, веће осетљивости, неинвазивног и бесконтактнoг мерења хемијских промена у човековом организму. У дијагностичке сврхе се најчешће користе сензори на микроталасним и терахерцним учестаностима.

Електромагнетски таласи утичу на материјале у зависности од њихове молекуларне структуре. Детекцијом реакције молекула након побуђивања могуће

је утврдити структуру анализираних ткива и течности као последицу њихових диелектричних својстава. Електромагнетски таласи могу до одређене мере продирати у анализирани узорке, омогућавајући неинвазивну дијагностику. Већина органских и неорганских материјала има специфичан фреквенцијски одзив, па се помоћу сензора може добити информација о структури материјала и функционалности. Помоћу низова сензора може се добити информација о фреквенцијском одзиву и истовремено о просторној расподели најмањег дела узорка који се тестира.

Микроталаси продиру дубље у анализирани узорак у односу на таласе у терахерцном или оптичком опсегу, али имају најнижу резолуцију детекције. Користе се при детекцији мањих промена концентрације глукозе у крви, детекцији етанола у води, туморских ћелија, итд. Код биоматеријала као што су протеини и ДНК, учестаности вибрационих модела молекула налазе се у THz опсегу, па се за њихову детекцију користи THz спектроскопија. Вируси су наночестице пречника од 10 до 300 nm, које карактерише одговарајућа диелектрична пермитивност. Бактериофага (вируси између 30 nm и 60 nm) успешно је детектована помоћу сензора базираног на метаматеријалу [1], [2]. Неки вируси показали су патогена својства са пандемијским потенцијалом. Стандардни метод детекције вируса је RT-PCR метода (Reverse transcription polymerase chain reaction) која открива присуство специфичног генетског материјала у било ком патогену. Ова дијагностичка метода представља сложен поступак детекције и временски је захтевна (траје и до три сата). Алтернативни начин детекције вируса, у терахерцном опсегу учестаности, коришћењем сензора на бази метаматеријала, омогућава бржу дијагностику и осетљивост откривање наночестица. Последње деценије THz спектроскопија се користи за брзо откривање и идентификацију биолошких узорака, јер омогућава бесконтактну и неинвазивну детекцију без коришћења реагенса за обележавање узорака [3], [4]. Ако је за саму детекцију потребно неколико секунди, додајући и време постављања узорка, значи да цела обрада траје око 10-15 секунди, што на дневном нивоу износи преко 5760 - 8640 анализираних узорака. Поређења ради, према званичним подацима Министарства здравља Републике Србије, тренутни капацитети на нивоу државе су око 11000 узорака дневно за детекцију вируса SARS-CoV-2 коришћењем RT-PCR методе [5].

У циљу што брже дијагностике заразе вирусима, у овом истраживању су анализирани биосензори за детекцију

Милка Потребих, Никола Баста, Дуња Лончаревић – Електротехнички факултет, Универзитет у Београду, Булевар краља Александра 73, 11020 Београд, Србија (е-пошта: milka\_potrebic@etf.rs, nbasta@etf.rs, dunja.loncarevic@live.com).

вируса инфлуенце А који узрокује заразну болест птица познату као птичји грип. Опасност по људску врсту настаје онда када вирус настани јединке које живе унутар живинских фарми, чиме се могућност преноса на човека знатно повећава услед интензивног контакта. Пандемијски потенцијал који дати вирус има је један од главних разлога истраживања у области конструисања биосензора [6].

У раду је извршена упоредна анализа перформанси две јединичне ћелије метаматеријала за детекцију вируса инфлуенце А. Приказан је преглед резултата добијен електромагнетском анализом периодичних структура и изведени су закључци са даљим правцима истраживања.

## II. ФРЕКВЕНЦИЈСКИ СЕЛЕКТИВНЕ ПОВРШИНЕ

Фреквенцијски селективне површине – метаматеријали су вештачки материјали који су пажљиво пројектовани да дају жељени фреквенцијски одзив. Ови материјали су сачињени од јединичних елемената чије су димензије знатно мање од таласне дужине инцидентног таласа [7]. Јединични елементи могу бити реализовани од разних материјала и распоређују се периодично у простору. Заједничка особина свих метаматеријала је да поседују карактеристике које немају природни материјали.

Карактеристике несвојствене за конвенционалне материјале, нису последица самих коришћених материјала (диелектрика и метала) за реализацију јединичног елемента, већ су резултат облика елемента, као и правилности по којој се елемент периодично понавља у простору. Прецизно одређена геометрија вештачког материјала, као и његове димензије и оријентација му омогућавају контролу простирања електромагнетских таласа (слабљење, апсорбовање, или усмеравање таласа).

Напредак технологија израде метаматеријала, са димензијама јединичних елемената реда нанометра, доноси могућност њихове масовне производње и шире доступности. Терахерцни метаматеријали нуде широк спектар могућих примена као што су брзи модулатори, електромагнетски апсорбери, филтери, разне врсте сензора, полупроводнички ласери и детектори.

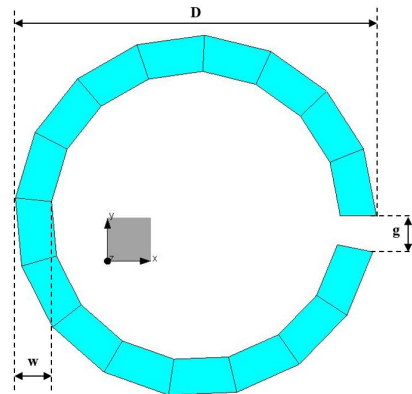
Очекује се да ће сензорска технологија заснована на метаматеријалима у скорој будућности пружити широк спектар примена у медицини поред оних везаних за присуство вируса [8]. Биосензори се могу користити за детекцију канцерогених ћелија, у области радиологије, као и у области медицинских бежичних телеметријских система.

У овом истраживању, апсорбери су пројектовани на бази метаматеријала, а за детекцију је коришћен коефицијент апсорпције у датом опсегу учестаности. Учестаности локалних максимума апсорпције зависе од средине у којој се сензор налази, па се очекује да додавањем слоја вируса на површину сензора дође до померања учестаности максимума у односу на почетну вредност.

### A. Јединични елемент метаматеријала

Прво се анализирају два модела јединичног елемента која се користе при пројектовању метаматеријала за детекцију вируса инфлуенце А.

Први изабрани јединични елемент (модел А) је кружни полуталасни резонатор (Split Ring Resonator - SRR), који се састоји из кружне контуре са малим процепом који узрокује капацитивност на крајевима контуре што утиче на смањивање резонантне учестаности (сл. 1). Димензије SRR (модела А) су следеће:  $D = 15 \mu\text{m}$ ,  $w = 1.25 \mu\text{m}$ ,  $g = 1 \mu\text{m}$ . Просторна периода понављања за реализацију метаматеријала по  $x$ -оси и  $y$ -оси је  $a = 25 \mu\text{m}$ . SRR је реализован од злата [9].



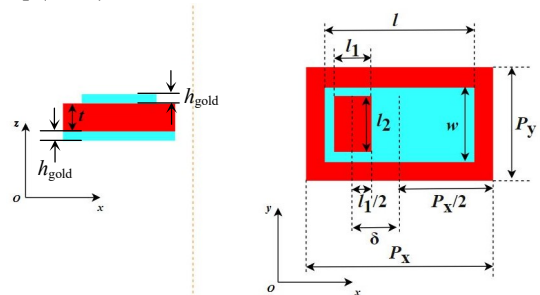
Сл. 1. Кружни прстенасти полуталасни резонатор.

Други јединични елемент (модел Б) је перфорирани правоугаони резонатор са металном плочом. Реализован је од злата дебљине  $h_{\text{gold}} = 0.4 \mu\text{m}$ , док је релативна пермитивност подлоге  $\epsilon_r = 3(1 - j0.05)$ . На сл. 2 је приказан модел Б са обележеним димензијама:  $t = 9 \mu\text{m}$ ,  $l = 80 \mu\text{m}$ ,  $w = 40 \mu\text{m}$ ,  $l_1 = 25 \mu\text{m}$ ,  $l_2 = 35 \mu\text{m}$ ,  $\delta = 18 \mu\text{m}$ . Просторна периода понављања за реализацију метаматеријала по  $x$ -оси износи  $P_x = 100 \mu\text{m}$ , а по  $y$ -оси  $P_y = 60 \mu\text{m}$  [7].

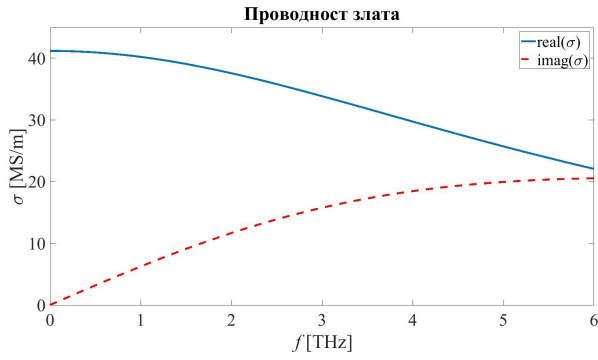
На учестаностима од неколико THz, проводност злата је функција радне учестаности и описана је Друдовим моделом:

$$\sigma = \epsilon_0 \omega_p^2 / (\gamma - j\omega), \quad (1)$$

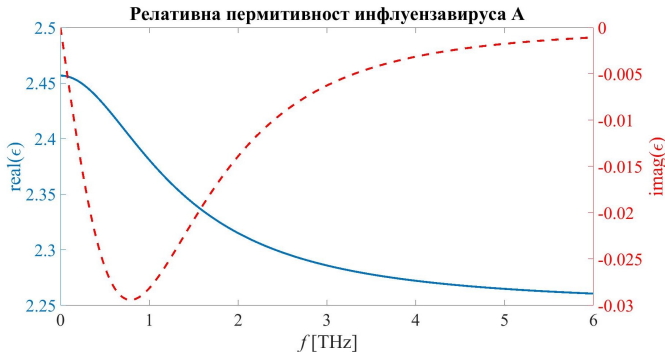
где је  $\omega = 2\pi f$  угаона учестаност,  $f_p$  је учестаност плазме (сопствена учестаност осциловања слободних електрона) и износи 2184 THz ( $\omega_p = 2\pi f_p$ ), а  $\gamma = 40.5 \times 10^{12} \text{ s}^{-1}$  (фактор пригушења који потиче од расејања проводних електрона) [9], [10] (сл. 3).



Сл. 2. Перфорирани правоугли резонатор: бочни пресек и горња страна штампане плочице.



Сл. 3. Реални и имагинарни део проводности злата.



Сл. 4. Реални и имагинарни део релативне пермитивности вируса инфлуенце А.

#### Б. Моделовање пермитивности вируса инфлуенце А

Релативна пермитивност вируса инфлуенце А је функција радне учестаности и дата је формулом:

$$\epsilon = \epsilon_{re} + j\epsilon_{im}, \quad (2)$$

$$\epsilon_{re} = (1.5)^2 + \left( \omega_{pv}^2 \left( \omega^2 + \omega_0^2 \right) \right) / \left( \left( \omega^2 + \omega_0^2 \right)^2 + (\gamma_v \omega)^2 \right), \quad (3)$$

$$\epsilon_{im} = -\omega_{pv}^2 \omega \gamma_v / \left( \left( \omega^2 + \omega_0^2 \right)^2 + (\gamma_v \omega)^2 \right), \quad (4)$$

где су  $\omega_{pv} = \gamma_v = 4$  THz,  $\omega_0 = 2.8\pi$  THz [6] (сл. 4).

Вирус инфлуенце А се моделује слојем који прекрива метаматеријал преко штампане структуре. Дебљине слоја вируса ( $h_{virus}$ ) које су разматране у овом истраживању су  $1 \mu m$ ,  $5 \mu m$  и  $8 \mu m$  [6].

#### В. Моделовање периодичних структура

Како су метаматеријали сачињени од великог броја јединичних елемената, моделовање подразумева њихово периодично понављање. Појединачно моделовање ћелија метаматеријала је релативно захтевно и уводи велики број непознатих чиме се време извршавања симулације продужава. Због тога је при моделовању метаматеријала, у софтверском алату *WILP-D*, коришћена функционалност *Periodic Boundary Condition (PBC)*. *PBC* је скуп граничних услова који се примењују у анализи бесконачних димензионалних електромагнетских система моделујући притом само један елемент посматраног система. Тај елемент се назива јединични елемент или ћелија. Јединични елемент може бити тродимензионална структура која се периодично понавља у  $xOy$ -равни формирајући на тај начин „ортогоналну решетку“.

Периоде дуж  $x$ -осе и  $y$ -осе су редом  $dx = X_2 - X_1$  и  $dy = Y_2 - Y_1$ , док свака  $z$ -координата јединичног елемента мора задовољавати услов  $Z_1 < z < Z_2$ . Приступци су дефинисани као равни паралелне  $xOy$ -равни,  $z$ -координате  $Z_1$  (*Port 2*), односно  $Z_2$  (*Port 1*). Постоји и могућност дефинисања домена испод приступа означеног као *Port 2*, док је домен изнад приступа означеног као *Port 1* вакуум.

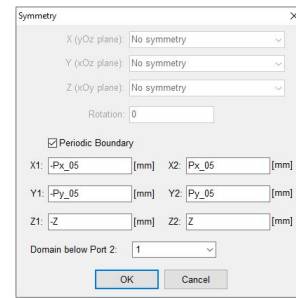
При моделовању, *PBC* функционалност је доступна једино када је у софтверу *operation mode* подешен на једну од опција за расејање [11].

Примена опције *PBC* приказана је кроз пример моделовања јединичне ћелије модела Б без вируса чија је геометрија дата на сл. 2. Периода дуж  $x$ -осе одређена је следећим параметрима:

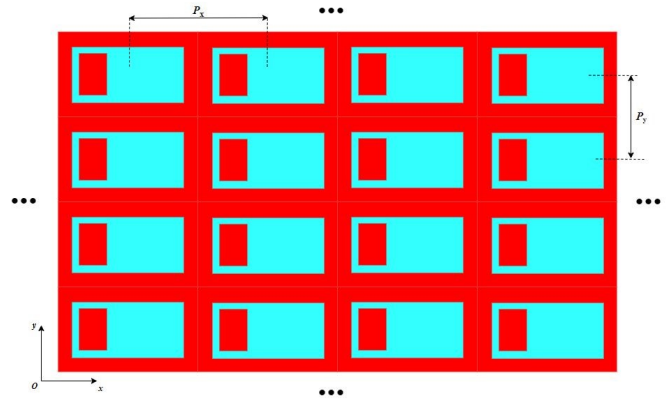
$$dx = X_2 - X_1 = P_x, \quad X_1 = -P_x/2 = -X_2 \quad (5)$$

док је периода дуж  $y$ -осе описана:

$$dy = Y_2 - Y_1 = P_y, \quad Y_1 = -P_y/2 = -Y_2. \quad (6)$$



Сл. 5. Приказ прозора у алату *WILP-D* у коме се дефинише *PBC*.



Сл. 6. Метаматеријал са јединичним елементом модела Б (двострумензиони приказ).

За  $Z_1$  и  $Z_2$  узете су вредности које одговарају, редом, минималним и максималним  $z$ -координатама јединичног елемента повећаних за 10%, према препоруци у [11]. Домен испод приступа означеног као *Port 2* је вакуум. Приказ прозора у софтверском алату *WILP-D* у коме се дефинише *PBC* представљен је на сл. 5. На сл. 6 је приказана периодична структура (метаматеријал) чији је јединични елемент модел Б. Параметри таласа којим побуђујемо посматрану структуру су дати у табели I. Исти поступак је примењен за дефинисање *PBC* параметара свих анализираних структура.

ТАБЕЛА I  
ПАРАМЕТРИ ПОБУЂУЈУЋЕГ ТАЛАСА.

Правац		$E_\phi$ [V/m]		$E_\theta$ [V/m]	
$\phi$ [°]	$\theta$ [°]	Real	Imag	Real	Imag
0	90	0	0	1	0

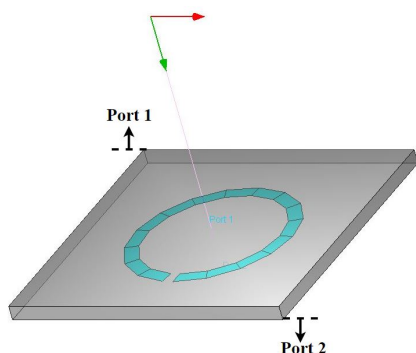
### III. СИМУЛАЦИОНИ РЕЗУЛТАТИ ДЕТЕКЦИЈЕ ВИРУСА

Резултати детекције вируса инфлуенце А коришћењем метаматеријала са јединичним ћелијама означеним ако модел А и Б дати су у наставку.

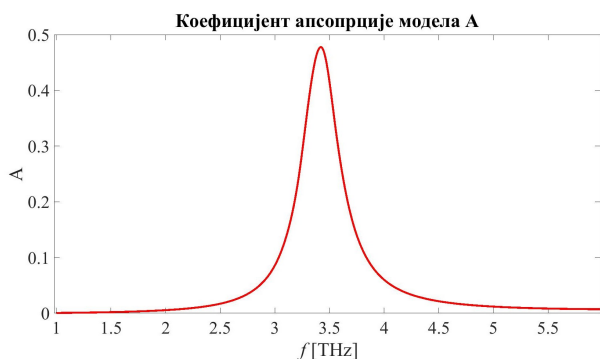
#### А. Модел А без присуства вируса

На сл. 7 је приказана јединична ћелија модела А без вируса, док је на сл. 8 приказан њен коефицијент апсорпције. Коефицијент апсорпције се дефинише као у [12]:

$$A(f) = 1 - |S_{11}(f)|^2 - |S_{21}(f)|^2 \quad (7)$$



Сл. 7. Јединична ћелија модела А без присуства вируса.



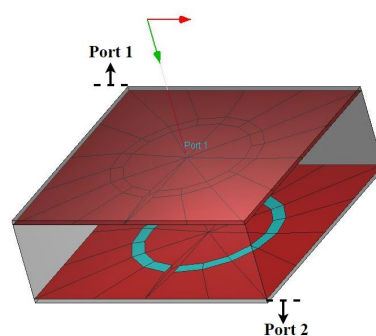
Сл. 8. Коефицијент апсорпције метаматеријала са јединичном ћелијом модела А, без присуства вируса.

Са сл. 8. се може уочити да коефицијент апсорпције достиже максимум при учестаности  $f_A = 3.416$  THz и износи  $A_A = 0.4755$ .

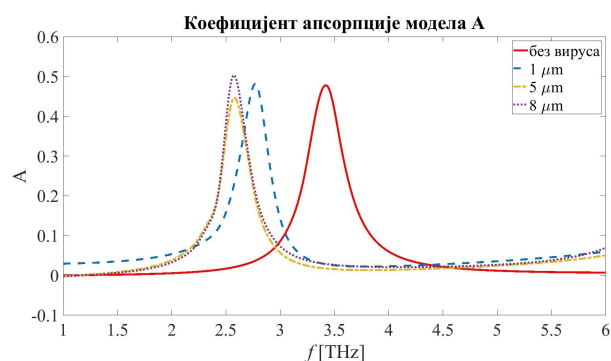
#### Б. Модел А са слојем вируса

Након додавања слоја вируса (сл. 9), посматран је његов утицај на коефицијент апсорпције. На сл. 10 је приказан коефицијент апсорпције у функцији учестаности за четири случаја модела А: 1) без вируса, 2) са слојем вируса дебљине 1  $\mu\text{m}$ , 3) са слојем вируса дебљине 5  $\mu\text{m}$ ,

и 4) са слојем вируса дебљине 8  $\mu\text{m}$ . У табели II су издвојени кључни резултати са сл. 10.



Сл. 9. Јединична ћелија модела А са слојем вируса.



Сл. 10. Коефицијент апсорпције модела А без и са слојем вируса различитих дебљина (1, 5 и 8  $\mu\text{m}$ ).

ТАБЕЛА II  
ЛОКАЛНИ МАКСИМУМИ КОЕФИЦИЈЕНТА АПСОРПЦИЈЕ И УЧЕСТАНОСТИ КОЈЕ ОДГОВАРАЈУ ТИМ МАКСИМУМИМА ЗА МОДЕЛ А БЕЗ И СА СЛОЈЕМ ВИРУСА РАЗЛИЧИТИХ ДЕБЉИНА (1, 5 и 8  $\mu\text{m}$ ).

	без вируса	са вирусом		
		$h_{\text{virus}}$ [ $\mu\text{m}$ ]		
		1	5	8
$f_{\text{peak}}$ [THz]	3.416	2.770	2.596	2.579
$A_{\text{peak}}$	0.47755	0.48114	0.44127	0.5022
$ \Delta f_{\text{peak}} $ [GHz]	/	646	820	837
$ \Delta A_{\text{peak}} $	/	0.00359	0.03628	0.02465

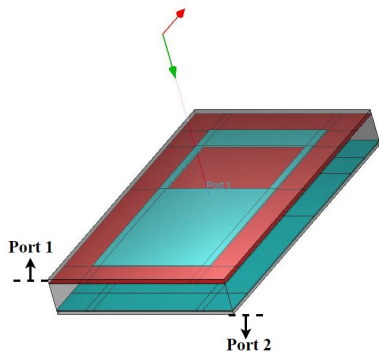
На основу табеле II се може уочити фреквенцијски померај код модела А са слојем вируса одговарајуће дебљине у односу на модел без вируса. Ако постоји фреквенцијски померај у одзиву, онда кажемо да се вирус може детектовати. Са графика приказаног на сл. 10 се јасно уочава да је могуће детектовати постојање вируса. Такође, могуће је направити и разлику између тога која је дебљина слоја вируса. Слој дебљине 1  $\mu\text{m}$  се од других вредности разликује по фреквенцијском померају, док се слојеви дебљина 5 и 8  $\mu\text{m}$  међусобно могу диференцирати по вредности коефицијента апсорпције у односу на модел без вируса. Између слојева дебљине 5 и 8  $\mu\text{m}$  постоји и мали фреквенцијски померај, који у зависности од

резолюције мерног инструмента којим се мере  $S$ -параметри биосензора, такође може да се користи за диференцирање ова два модела.

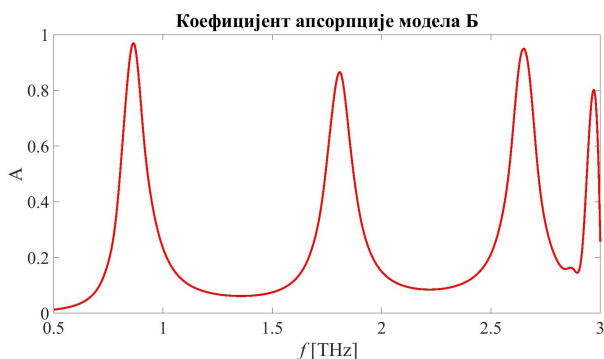
### В. Модел Б без присуства вируса

На сл. 11 је приказана јединична ћелија модела Б без вируса, док је на сл. 12 дат коефицијент апсорпције овог модела.

Са графика приказаног на сл. 12 могу се очитати четири локална максимума, а вредности локалних максимума коефицијента апсорпције и учестаности које одговарају тим максимумима су издвојене у табели III. Биће анализирана само прва два локална максимума.



Сл. 11. Јединична ћелија модела Б без присуства вируса.



Сл. 12. Коефицијент апсорпције метаматеријала са јединичном ћелијом модела Б, без присуства вируса.

### Г. Модел Б са слојем вируса

Као и код модела А, посматрамо ефекат слоја вируса на коефицијент апсорпције. На сл. 13 су приказани коефицијенти апсорпције у функцији учестаности за четири случаја модела Б: 1) без вируса, 2) са слојем вируса дебљине  $1 \mu\text{m}$ , 3) са слојем вируса дебљине  $5 \mu\text{m}$ , и 4) са слојем вируса дебљине  $8 \mu\text{m}$ .

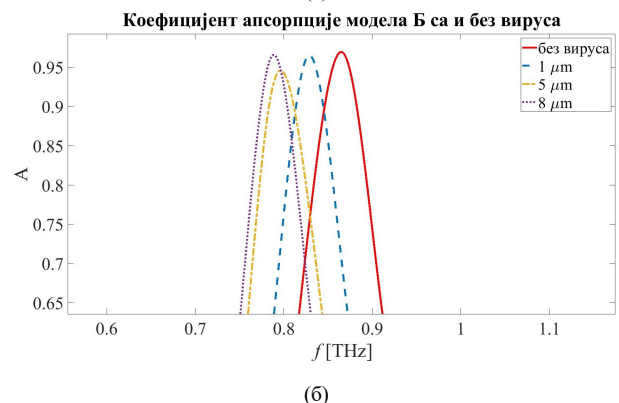
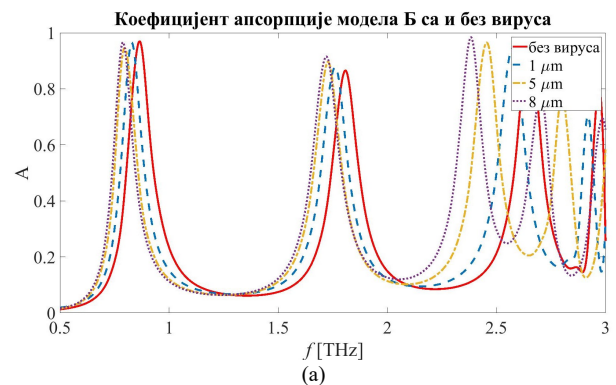
У табели IV су дати кључни подаци са сл. 13. Резултати су слични као и за модел А. Јасно је да се вирус инфлуенце А може детектовати коришћењем метаматеријала чији је јединични елемент модел Б. Такође, могуће је направити и разлику између тога која је узета дебљина слоја вируса. Слој дебљине  $1 \mu\text{m}$  се од других вредности разликује по фреквенцијском померају, док се слојеви дебљине  $5$  и  $8 \mu\text{m}$  међусобно могу

диференцирати по промени вредности коефицијента рефлексије у односу на модел без вируса. Између слојева дебљине  $5$  и  $8 \mu\text{m}$  постоји и мали фреквенцијски померај, који у зависности од резолуције мерног инструмента којим се мере  $S$ -параметри биосензора, такође може да се користи за диференцирање ова два модела.

ТАБЕЛА III

ЛОКАЛНИ МАКСИМУМИ КОЕФИЦИЈЕНТА АПСОРПЦИЈЕ И УЧЕСТАНОСТИ КОЈЕ ОДГОВАРАЈУ ТИМ МАКСИМУМИМА.

$i$	1	2	3	4
$f_{\text{peak}, i}$ [THz]	0.864	1.809	2.650	2.970
$A_{\text{peak}, i}$	0.96949	0.86522	0.9495	0.80191



Сл. 13. Коефицијент апсорпције модела Б без и са слојем вируса различитих дебљина ( $1$ ,  $5$  и  $8 \mu\text{m}$ ): (а) у ширем опсегу учестаности, (б) у околини првог локалног максимума.

У околини првог и другог локалног максимума, референтног (оригиналног) модела Б без вируса, учача се слична расподела максимума за различите дебљине слоја вируса, уз незнатна одступања фреквенцијског помераја и вредности коефицијента апсорпције. Трећи и четврти референтни локални максимума нису коришћени при детекцији, јер се налазе реалативно близу, а у случају присуства вируса долази до преклапања апсорпционих кривих у том делу спектра.

## IV. ЗАКЉУЧАК

У раду је приказана могућност коришћења апсорбера као биосензора за детекцију присуства вируса. Као референтни параметар детекције коришћен је

кофицијент апсорпције. Показује се да је могуће детектовати фреквенцијски померај и/или промену вредности локалног максимума коефицијента апсорпције, у односу на случај биосензора без вируса. Узимајући у обзир оба параметра при одлучивању може се донети прецизан закључак. Биосензор је реализован на бази метаматеријала са јединичним ћелијама које могу да детектују вирус инфлуенце А.

ТАБЕЛА IV

ЛОКАЛНИ МАКСИМУМИ КОЕФИЦИЈЕНТА АПСОРПЦИЈЕ И УЧЕСТАНОСТИ КОЈЕ ОДГОВАРАЈУ ТИМ МАКСИМУМИМА ЗА МОДЕЛ Б БЕЗ И СА СЛОЈЕМ ВИРУСА РАЗЛИЧИТИХ ДЕБЉИНА (1, 5 И 8  $\mu\text{m}$ )

$i$		без вируса	са вирусом		
			$h_{\text{virus}} [\mu\text{m}]$		
			1	5	8
1	$f_{\text{peak}, 1} [\text{THz}]$	0.864	0.829	0.797	0.789
	$A_{\text{peak}, 1}$	0.96949	0.96522	0.94446	0.9659
	$ \Delta f_{\text{peak}, 1}  [\text{GHz}]$	/	35	67	75
	$ \Delta A_{\text{peak}, 1} $	/	0.00427	0.02503	0.00359
2	$f_{\text{peak}, 2} [\text{THz}]$	1.809	1.762	1.731	1.720
	$A_{\text{peak}, 2}$	0.86522	0.87684	0.89905	0.91508
	$ \Delta f_{\text{peak}, 2}  [\text{GHz}]$	/	47	78	89
	$ \Delta A_{\text{peak}, 2} $	/	0.01162	0.03383	0.04986

На основу анализе две јединичне ћелије може се уочити да је критична резолуција инструмента којим се мере  $S$ -параметри биосензора. Предност при детекцији има метаматеријал чији је јединични елемент SRR (модел А), јер је фреквенцијски померај са слојем вируса више од 10 пута већи од истог фреквенцијског помераја за случај јединичног елемента као перфорираног правоуглог резонатора (модел Б).

Мана биосензора базираног на моделу А, у односу на модел Б, се огледа у томе што први сензор подразумева рад на вишим учестаностима. Такође, коефицијент апсорпције модела Б ја значајно већи од модела А што резултује израженијим локалним максимумима и, последично, већој осетљивости таквог сензора. Још једна предност модела Б потиче из чињенице да он без вируса има више локалних максимума који могу да се користе као референца у случајевима када се слој вируса нанесе на сензор.

Даљи правци истраживања подразумева би испитивање осетљивости сензора на различите подтипове и сојеве вируса инфлуенце А, анализирање коефицијента апсорпције за већи број различитих вредности дебљина слоја вируса, проучавање коришћења коначног броја јединичних елемената у односу на бесконачан број, као и крајњу израду оваквог сензора.

#### ЗАХВАЛНИЦА

Ово истраживање је рађено у оквиру пројекта бр. 50206

који је финансиран од Фонда за иновациону делатност из буџета Републике Србије од стране Министарства просвете, науке и технолошког развоја, а кроз Пројекат за унапређење конкурентности и запошљавања (споразум о зајму са Светском банком). Истраживање је делимично подржано од стране Министарства просвете, науке и технолошког развоја Републике Србије.

#### ЛИТЕРАТУРА

- [1] K. Meng et al., "Increasing the sensitivity of terahertz split ring resonator metamaterials for dielectric sensing by localized substrate etching," *Opt. Express*, vol. 27, no. 16, pp. 23164-23172, 2019.
- [2] S. J. Park et al., "Sensing viruses using terahertz nano-gap metamaterials," *Biomed. Opt. Express*, vol. 8, no. 8, pp. 3551-3558, 2017.
- [3] S. J. Park, A. R. Kim, J. T. Hong, J. Y. Park, S. Lee, and Y. H. Ahn, "Crystallization kinetics of lead halide perovskite film monitored by in-situ terahertz spectroscopy," *J. Phys. Chem. Lett.*, vol. 8, no. 2, pp. 401-406, 2017.
- [4] A. Keshavarz, Z. Vafapour "Water-based terahertz metamaterial for skin cancer detection application," *IEEE Sens. J.*, vol. 19, no. 4, 2019.
- [5] Статистички подаци о вирусу COVID-19 у Републици Србији, <https://covid19.rs/>
- [6] A. Keshavarz, Z. Vafapour, "Sensing avian influenza viruses using terahertz metamaterial reflector," *IEEE Sens. J.*, vol. 19, no. 13, 2019.
- [7] Q. Xie, G. Dong, B. Wang, W. Huang, "Design of quad-band terahertz metamaterial absorber using a perforated rectangular resonator for sensing applications," *Nanoscale Res. Lett.*, vol. 13, pp. 1-8, 2018.
- [8] W. Xu, et al., "Mechanisms and applications of terahertz metamaterial sensing: a review," *Nanoscale*, vol. 9, no. 37, pp. 13864-13878, 2017.
- [9] N. Shen, P. Tassin, T. Koschny, C. Soukoulis, "Comparison of gold- and graphene-based resonant nano-structures for terahertz metamaterials and an ultra-thin graphene-based modulator," *Phys. Rev. B*, vol. 90, no. 11, pp. (115437) 1-8, 2014.
- [10] J. B. Khurgin, A. Boltasseva, "Reflecting upon the losses in plasmonics and metamaterials," *MRS Bull.*, vol. 37, no. 8, pp. 768-779, 2012.
- [11] WIPL-D Microwave Pro v5.1 Circuit and EM Simulation Professional Edition – User's Manual, 2018.
- [12] K. Ozden, O. M. Yucedag, H. Kocer, "Metamaterial based broadband RF absorber at X-band," *AEU-Int J Electron C*, vol. 70, no. 8, pp. 1062-1070, 2016.

#### ABSTRACT

Viral infections that have pandemic potential pose a threat to all of humanity. In order to speed up diagnostics and increase the capacity for testing of virus infection, the possibility of introducing alternative diagnostic methods, such as the use of biosensors, opens up. Recently, the search for the reliable alternative to the existing methods has occupied an increasingly important place in order to achieve faster diagnostics, higher sensitivity, non-invasive and non-contact measurement. In the terahertz frequency range, using sensors based on frequency-selective surfaces - metamaterials, enables faster diagnostics and sensitivity of detecting nano substances. In order to more reliably detect influenzavirus A, two different metamaterial cells were analyzed. The biosensor was designed as an absorber, and the absorption coefficient was used as the reference parameter for detection. Frequency shifts and changes in the values of the absorption coefficient with and without the existence of the virus are analyzed. It is obtained that a unit element with more resonant frequencies has higher sensitivity than an element with one resonant frequency.

#### Biosensors based on frequency selective surfaces

Milka Potrebić, Dunja Lončarević, Nikola Basta